High-order harmonic generation with few-cycle pulses for ultrafast electron spectroscopy

Ouahioune, Nedjma

2026

Document Version:
Publisher's PDF, also known as Version of record

High-order harmonic generation with few-cycle pulses for ultrafast electron spectroscopy

NEDJMA OUAHIOUNE
DEPARTMENT OF PHYSICS | FACULTY OF ENGINEERING, LTH | LUND UNIVERSITY

High-order harmonic generation with few-cycle pulses for ultrafast electron spectroscopy

High-order harmonic generation with few-cycle pulses for ultrafast electron spectroscopy

by Nedjma Ouahioune

LUND
UNIVERSITY

Thesis for the degree of Doctor in Physics
Thesis advisors: Dr. Mathieu Gisselbrecht, Prof. Anne L'Huillier, Dr. Cord L. Arnold
Faculty opponent: Dr. Franck Lépine

To be presented with the permission of the Faculty of Engineering, LTH of Lund University, for public criticism in the Rydberg lecture hall at the Department of Physics on Friday, the 4th of September 2026 at 13:00.

Organization	Document name
LUND UNIVERSITY Department of Physics Box 118 SE–221 00 LUND Sweden	**DOCTORAL DISSERTATION** Date of disputation 2026-09-04 Sponsoring organization
Author(s) Nedjma Ouahioune	

Title and subtitle

High-order harmonic generation with few-cycle pulses for ultrafast electron spectroscopy

Abstract

In this thesis, a high-repetition-rate attosecond light source based on high-order harmonic generation in gases was used to perform time-resolved electron spectroscopy in atoms and solids. The source was driven by few-cycle near-infrared laser pulses with a controllable carrier-to-envelope phase, enabling the generation of sequences of two to four attosecond pulses in the extreme ultraviolet range within only a few laser half-cycles. Part of the work was devoted to characterizing these short attosecond pulse trains using laser-assisted photoionization. The results reveal that both microscopic and macroscopic aspects of the generation process influence the number and relative intensity of the pulses contributing at different photon energies. Temporal confinement of the emission was observed and attributed to subcycle phase-matching dynamics. The duration of the attosecond pulse trains was further reduced through precise control of the time-dependent polarization of the driving laser field. Subcycle polarization gating, where linear polarization is confined near the peak of the pulse envelope, strongly reduced the attosecond pulse duration. This was experimentally evidenced by the presence of continuous spectra highly sensitive to the laser carrier-to-envelope phase.

Another part of this thesis studied the impact of effects arising from the ultrashort nature of the light fields on laser-assisted photoionization of helium, where interference between electron wavepackets plays a central role. Four new types of quantum interference involving one-photon ionization pathways through absorption of the attosecond pulses and two-photon ionization pathways involving the absorption or emission of an additional laser photon were observed and theoretically explained. A second study investigated interference effects involving highly excited states of helium, highlighting the influence of the spectral amplitude and phase of the laser field. A retrieval method was developed to extract information about the excited states and the light fields.

Finally, measurements of ultrafast electron dynamics in semiconductors were performed. Carrier relaxation dynamics in cubic tin(II) sulfide were investigated under various photoexcitation conditions using attosecond transient absorption spectroscopy. Several relaxation pathways could be disentangled, including the onset of many-body interactions between carriers, which were found to accelerate cooling and recombination processes from a threshold photoinduced carrier density. Using time-resolved photoemission electron microscopy, the potential for spatial localization of photoelectron emission from indium phosphide nanowires driven by the few-cycle laser pulses was also experimentally and theoretically investigated. The photoelectron kinetic-energy distributions were found to be compatible with sub-femtosecond emission durations.

Key words

High-order harmonic generation, Attosecond, Photoionization

Classification system and/or index terms (if any)

Supplementary bibliographical information	Language
	English
ISSN and key title 0281-2762	ISBN 978-91-8104-984-8 (print) 978-91-8104-985-5 (pdf)
Recipient's notes	Number of pages 201 / Price
	Security classification

High-order harmonic generation with few-cycle pulses for ultrafast electron spectroscopy

by Nedjma Ouahioune

LUND
UNIVERSITY

A doctoral thesis at a university in Sweden takes either the form of a single, cohesive research study (monograph) or a summary of research papers (compilation thesis), which the doctoral student has written alone or together with one or several other author(s).

In the latter case the thesis consists of two parts. An introductory text puts the research work into context and summarizes the main points of the papers. Then, the research publications themselves are reproduced, together with a description of the individual contributions of the authors. The research papers may either have been already published or are manuscripts at various stages (in press, submitted, or in draft).

Cover illustration front: Laser-assisted photoionization spectrogram obtained with short APTs and few-cycle NIR laser pulses.

Cover illustration back: Spectrogram of electron photoemission from an InP nanowire induced by few-cycle NIR laser pulses.

Funding information: The thesis work was financially supported by the European Research Council (Grant Nos. 2020-05200, 2023-04603, 2021-04691) and the Knut and Alice Wallenberg Foundation.

Faculty of Engineering, LTH, Department of Physics

ISBN: 978-91-8104-984-8 (print)
ISBN: 978-91-8104-985-5 (pdf)
ISSN: 0281-2762

Printed in Sweden by Media-Tryck, Lund University, Lund 2026

« Que diable allait-il faire dans cette galère ? »
Molière, *Les Fourberies de Scapin*, acte II, scène 7.

Abstract

In this thesis, a high-repetition-rate attosecond light source based on high-order harmonic generation in gases was used to perform time-resolved electron spectroscopy in atoms and solids. The source was driven by few-cycle near-infrared laser pulses with a controllable carrier-to-envelope phase, enabling the generation of sequences of two to four attosecond pulses in the extreme ultraviolet range within only a few laser half-cycles. Part of the work was devoted to characterizing these short attosecond pulse trains using laser-assisted photoionization. The results reveal that both microscopic and macroscopic aspects of the generation process influence the number and relative intensity of the pulses contributing at different photon energies. Temporal confinement of the emission was observed and attributed to subcycle phase-matching dynamics. The duration of the attosecond pulse trains was further reduced through precise control of the time-dependent polarization of the driving laser field. Subcycle polarization gating, where linear polarization is confined near the peak of the pulse envelope, strongly reduced the attosecond pulse duration. This was experimentally evidenced by the presence of continuous spectra highly sensitive to the laser carrier-to-envelope phase.

Another part of this thesis studied the impact of effects arising from the ultrashort nature of the light fields on laser-assisted photoionization of helium, where interference between electron wavepackets plays a central role. Four new types of quantum interference involving one-photon ionization pathways through absorption of the attosecond pulses and two-photon ionization pathways involving the absorption or emission of an additional laser photon were observed and theoretically explained. A second study investigated interference effects involving highly excited states of helium, highlighting the influence of the spectral amplitude and phase of the laser field. A retrieval method was developed to extract information about the excited states and the light fields.

Finally, measurements of ultrafast electron dynamics in semiconductors were performed. Carrier relaxation dynamics in cubic tin(II) sulfide were investigated under various photoexcitation conditions using attosecond transient absorption spectroscopy. Several relaxation pathways could be disentangled, including the onset of many-body interactions between carriers, which were found to accelerate cooling and recombination processes from a threshold photoinduced carrier density. Using time-resolved photoemission electron microscopy, the potential for spatial localization of photoelectron emission from indium phosphide nanowires driven by the few-cycle laser pulses was also experimentally and theoretically investigated. The photoelectron kinetic-energy distributions were found to be compatible with sub-femtosecond emission durations.

Popular science summary

"High-order harmonic generation with few-cycle pulses for ultrafast electron spectroscopy". If I had to break down this title in plain English, it would be: "I shot at any poor electron unlucky enough to be in the way of my laser and took note of their reaction". This may sound unsettling, but this is not so far from the truth.

This thesis is about tracking the very (very) *fast* dynamics of very (very) *small* particles. But what does "very (very)" mean?

How fast and how small?

The particles we are interested in are electrons, which live in the smallest constituent of matter, called atoms. An atom is about 0.1 nanometer in size, that is, 0.0000000001 meter. For comparison, the smallest things we can see with our naked eyes are hair, and it is a million times larger. To see beyond our own limit, we use advanced instruments like microscopes, which is still not enough to see an atom. In this work, we focus on electrons which are even smaller than an atom!

Even if we could resolve the size of an electron, we would not see it because it moves too quickly. It is like attempting to follow by eye the course of a bullet, of a bolt of lightning or tracking your supervisor's thoughts. Simply impossible, one could think.

To overcome this, we can develop high-speed cameras that help us to make a movie in "slow motion". In practice, this means taking snapshots with a high shutter speed, and processing them at a speed we can keep up with. Imagine that you are recording a race: if you only take a snapshot at the start and at the finish, you miss everything in between. To truly see what happens, you need many images taken along the way.

Today, the fastest cameras can capture events lasting a few picoseconds (0.000000000001 seconds). As it turns out, this is still not enough to observe electrons since they move on *attosecond* time scales. An attosecond is 0.000000000000000001 second. If you don't have the time to count the zeros, I can do it for you: 18.

The camera we use is *ultrashort light pulses* at the attosecond time scale. We send our laser into a gas made of many atoms and the interaction leads to light bursts of attosecond duration: our attosecond shutter! The complex phenomena behind this interaction state something very simple: the shorter the laser pulses, the shorter the produced attosecond pulses. We therefore use a laser with the shortest pulse duration in the world. A part of this thesis has been devoted to study ways to reduce the duration of the produced attosecond pulses by controlling the interaction itself.

Measurement time!

Now that we have a tool fast enough to "film" electrons, the next question is: what do they actually do? Well in reality, we do not know much until the attosecond pulse impinges on the atom.

Something quirky occurs when this happens. Electrons can be at two places at the same time, with a certain *probability*. This means they may absorb energy from the light and become excited, so-called *photoexcitation*, or they may leave the atom, so-called *photoionization*.

However, electrons are not isolated. Like humans, when an electron wants to do something, neighboring particles might want to prevent it from doing so. In the case of photoionization for example, other electrons can interact to delay the time it takes the electron to leave the atom. Measuring the exact time has been one of the breakthroughs of attosecond science. Yet, it is a tough task since one needs to disentangle the contribution of the light used for the measurement from that of the surrounding environment. To do so requires both prior knowledge of the light properties and a robust experimental method. This thesis addresses both points by characterizing the properties of the short attosecond pulses and by showing that using them in time-resolved experimental studies provides new information about photoionization.

The principle behind these time-resolved experiments is always the same: the *pump-probe* scheme. A first light pulse kicks off the electron dynamics, and a second pulse probes the induced changes. By changing the time at which the second pulse arrives, a "movie" of the dynamics is made. These methods are applied here to study electrons in both atoms and solids, which are made of many atoms. Understanding how electrons move in such systems is fundamental, as many technologies are closely tied to their motion. From electronics and solar cells to emerging quantum technologies. Controlling electron motion is key to future innovations.

By improving our ability to observe and understand ultrafast electron dynamics, this work contributes to the long-term development of faster electronic devices and more efficient, sustainable materials.

Populärvetenskaplig sammanfattning

"Högordningens harmoniska generering med fåcykelpulser för ultrasnabb elektronspektroskopi".

Om jag skulle behöva bryta ned den här rubriken på ren svenska så skulle det bli: " jag sköt på alla stackars elektroner som råkade befinna sig i vägen för min laser och antecknade hur de reagerade." Det kan låta oroväckande men det ligger faktiskt inte så långt från sanningen.

Den här avhandlingen handlar om att följa den mycket (mycket) *snabba* dynamiken hos mycket (mycket) *små* partiklar. Men vad betyder egentligen "mycket (mycket)"?

Hur snabbt och hur smått?

De partiklar vi är intresserade av är elektroner, som lever i den minsta beståndsdelen av materia, så kallade atomer. En atom har en storlek på ungefär 0,1 nanometer, det vill säga 0,0000000001 meter. Som jämförelse är det minsta vi kan se med blotta ögat ungefär en miljon gånger större, ungefär lika brett som ett hårstrå. För att se bortom våra egna begränsningar använder vi avancerade instrument som mikroskop, men en atom är fortfarande 10 000 gånger mindre. Och elektroner är minst 100 000 gånger mindre än en atom.

Men även om vi kunde urskilja storleken på en elektron skulle vi inte kunna se den, eftersom den rör sig för snabbt. Det är som att försöka följa en kula, en blixt – eller din handledares tankar. Helt enkelt omöjligt skulle man kunna tro.

För att övervinna detta problem så kan vi utveckla höghastighetskameror som hjälper oss att skapa en film i "slow motion". Det innebär i praktiken att man tar bilder med mycket kort exponeringstid och sedan spelar upp dem i en hastighet vi kan följa. Föreställ dig att du filmar ett lopp: om du bara tar en bild vid start och en vid mål missar du allt däremellan. För att verkligen se vad som händer behövs många bilder längs vägen.

Idag kan de snabbaste kamerorna fånga händelser som varar några pikosekunder (0,000000000001 sekunder). Men det räcker fortfarande inte för att observera elektroner, eftersom de rör sig på *attosekundsskalan*. En attosekund är 0,000000000000000001 sekund. Om du inte har tid att räkna nollorna efter decimaltecknet kan jag göra det åt dig: 18.

Kameran vi använder är *ultrakorta ljuspulser* på attosekundsskala. För att nå attosekundsområdet skickar vi vår laser genom en gas bestående av många atomer. Växelverkan leder då till ljusblixtar med attosekunders varaktighet: vår attosekund-"slutare"!

De komplexa fenomenen bakom denna växelverkan säger något väldigt enkelt: ju kortare laserpulser, desto kortare blir de producerade attosekundspulserna. Därför pressar vi ner laserpulsernas längd till några få femtosekunder. En del av denna avhandling har ägnats åt att undersöka sätt att ytterligare förkorta de producerade attosekundspulserna genom att kontrollera själva växelverkan, utan att ändra den drivande laserpulsens varaktighet.

Dags att mäta!

Nu när vi har ett verktyg som är tillräckligt snabbt för att ”filma” elektroner, är nästa fråga: vad gör de egentligen? I själva verket vet vi inte mycket förrän attosekundpulsen träffar atomen. När detta sker inträffar något märkligt. Elektroner kan befinna sig på två ställen samtidigt, med en viss *sannolikhet*. Detta innebär att de kan absorbera energi från ljuset och bli exciterade, så kallad *fotoexcitation*, eller så kan de lämna atomen, så kallad *fotojonisering*.

Elektroner är dock inte isolerade. Precis som människor kan närliggande partiklar försöka hindra en elektron från att göra något när den vill göra det. Vid fotojonisering kan till exempel andra elektroner interagera för att fördröja den tid det tar för elektronen att lämna atomen. Att mäta den exakta tiden har varit ett av genombrotten inom attosekundvetenskapen. Det är dock en svår uppgift eftersom man måste skilja ut bidraget från det ljus som används för mätningen från det som kommer från omgivningen. För att göra detta krävs både förkunskaper om ljusets egenskaper och en robust experimentell metod. Denna avhandling behandlar båda dessa punkter genom att karakterisera egenskaperna hos de korta attosekundspulserna och genom att visa att användningen av dem i tidsupplösta experimentella studier ger ny information om fotojonisering.

Principen bakom dessa experiment är alltid densamma: en första ljuspuls sätter igång elektronernas rörelsemönster, och en andra puls undersöker de förändringar som uppstår. Genom att variera tidpunkten för den andra pulsen kan man spela in en ”film” av dynamiken. Dessa metoder används här för att studera elektroner både i enskilda atomer och i fasta material, som består av många atomer. Att förstå hur elektroner rör sig i sådana system är av grundläggande betydelse, eftersom många tekniker är nära kopplade till elektronernas rörelse. Från elektronik och solceller till nya kvanttekniker är kontrollen av elektronernas rörelse avgörande för framtida innovationer.

Genom att förbättra vår förmåga att observera och förstå ultrafast elektrondynamik bidrar detta arbete till den långsiktiga utvecklingen av snabbare elektroniska komponenter och mer effektiva och hållbara material.

Résumé scientifique vulgarisé

« Génération d'harmoniques d'ordre élevé avec des impulsions laser à peu de cycles pour application à la spectroscopie électronique ultrarapide ».

Une manière simple d'expliquer mon titre serait : j'ai tiré sur tous les pauvres électrons assez malchanceux pour se trouver sur le chemin de mon laser, et que j'ai observé leur réaction. Cela peut sembler déstabilisant, mais cela est assez proche de la réalité.

Cette thèse porte sur le suivi de la dynamique très (très) *rapide* de particules très (très) *petites*. Mais qu'entend-on par « très (très) » ?

À quelle vitesse et à quelle échelle ?

Les particules qui nous intéressent sont les électrons, qui vivent dans les plus petits constituants de la matière appelés atomes. Un atome a une taille d'environ 0,1 nanomètre, soit 0,0000000001 mètre. À titre de comparaison, les plus petites choses que nous pouvons voir à l'œil nu sont un million de fois plus grandes, de l'ordre de l'épaisseur d'un cheveu. Pour dépasser nos propres limites, nous faisons appel à des instruments avancés comme les microscopes, ce qui ne suffit toujours pas pour voir un atome. Dans ce travail, nous nous intéressons aux électrons, qui sont encore plus petits qu'un atome !

Mais même si nous pouvions distinguer la taille d'un électron, nous ne le verrions pas, car il se déplace trop rapidement. C'est comme essayer de suivre à l'œil nu la trajectoire d'une balle de pistolet, d'un éclair ou les pensées de votre directeur de thèse. Tout simplement impossible, pourrait-on penser.

Pour observer des phénomènes aussi rapides, les caméras ultra-rapides peuvent nous aider en ralentissant le film du mouvement. L'idée repose sur la prise de plusieurs images, ensuite projetées les unes après les autres à une vitesse que nous pouvons suivre. Imaginez que vous deviez filmer une course : si vous ne prenez qu'une photo au départ et une à l'arrivée, vous manquerez tout ce qui se passe au milieu. Pour vraiment voir ce qui se passe, il faut prendre de nombreuses images tout au long de la course.

Aujourd'hui, les caméras les plus rapides peuvent capturer des événements de quelques picosecondes (0,000000000001 seconde). Cependant, cela reste insuffisant pour observer les électrons, car ils évoluent sur des échelles de temps *attosecondes*. Une attoseconde correspond à 0,000000000000000001 seconde. Si vous n'avez pas le temps pour compter les zéros après la virgule, je le fais pour vous : 18.

Notre caméra est faite d'*impulsions lumineuses ultracourtes*, de durées attosecondes. On envoie notre laser dans un gaz composé de nombreux atomes, et l'interaction produit des impulsions lumineuses de durée attoseconde : notre caméra attoseconde ! La physique complexe de l'interaction donne lieu à une règle très simple : plus les impulsions laser sont courtes, plus les impulsions attosecondes produites le sont également. Nous utilisons donc les lasers avec les durées les plus courtes du monde. Une partie de cette thèse a été consacrée à l'étude de moyens de réduire la durée des impulsions attosecondes produites en contrôlant l'interaction elle-même.

Place aux mesures !

Maintenant que nous disposons d'un outil assez rapide pour « filmer » les électrons, la question suivante est : que font-ils réellement ? En réalité, pas grand-chose… jusqu'à l'arrivée des impulsions attosecondes lumineuses. Lorsque cela arrive, quelque chose d'étrange se produit. Les électrons peuvent se trouver à deux endroits en même temps, avec une certaine *probabilité*. Ils peuvent rester dans leur état initial, être excités, ce qui s'appelle *photoexcitation*, ou ils peuvent quitter l'atome en absorbant de l'énergie lumineuse, ce qui s'appelle *photoionisation*.

Cependant, les électrons ne sont pas isolés. Comme les humains, lorsqu'un électron veut faire quelque chose, les particules voisines peuvent tenter de l'en empêcher. Dans le cas de la photoionisation par exemple, d'autres électrons intéragissent avec lui ce qui peut retarder le moment où il parvient à quitter l'atome. Mesurer précisément ce temps constitue un des grands succès de la science attoseconde. Pourtant, c'est une tâche redoutable, car la lumière utilisée pour la mesure a un impact sur le mouvement des électrons qui doit être pris en compte. De telles études nécessitent donc à la fois une connaissance préalable des propriétés de l'impulsion lumineuse et une méthode expérimentale robuste. Cette thèse aborde ces deux aspects en caractérisant les propriétés des impulsions attosecondes courtes, et en montrant que leur utilisation dans des expériences résolues en temps fournit davantage d'informations sur la photoionisation.

Le principe de ces expériences repose sur le même principe : la technique *pompe-sonde*. Une première impulsion lumineuse initie la dynamique électronique, et une seconde sonde les changements induits. En modifiant le moment d'arrivée de la seconde impulsion, on obtient donc un film de la dynamique. Ces méthodes sont appliquées ici à l'étude des électrons dans les atomes ou dans les solides, constitués de nombreux atomes. Comprendre comment les électrons se déplacent dans ces systèmes est fondamental, car de nombreuses technologies dépendent étroitement de leur mouvement. De l'électronique aux panneaux solaires, en passant par les technologies quantiques émergentes, le contrôle du mouvement des électrons est essentiel pour les innovations futures.

En améliorant notre capacité à observer et comprendre la dynamique ultrarapide des électrons, ce travail contribue au développement à long terme de dispositifs électroniques plus rapides ainsi que de matériaux plus efficaces et durables.

List of publications

This thesis is based on the following publications, referred to by their Roman numerals:

I **Impact of oblique reflections on the generation of isolated attosecond pulses by polarization gating**
C. Picot, D. Díaz Rivas, **N. Ouahioune**, D. Hoff, L. Perez, S. Skupin, A. K. Raab, C. Guo, P. K. Maroju, A. L'Huillier, A-L. Viotti, C. L. Arnold, M. Gisselbrecht and E. Constant
Optics Letters, pp. 6738–6741

II **Subcycle phase matching effects in short attosecond pulse trains**

N. Ouahioune, R. Martín-Hernández, D. Hoff, P. K. Maroju, C. Guo, R. Weissenbilder, S. Mikaelsson, A. L'Huillier, M. Lucchini, C. L. Arnold and M. Gisselbrecht
Ultrafast Science, pp. 0154

III **Parity-mixing in photoionization**

N. Ouahioune, D. Hoff, P. K. Maroju, C. L. Arnold, D. Busto, A. L'Huillier, M. Gisselbrecht and S. Carlström
Submitted

IV **From interface-limited to Auger-dominated carrier dynamics in π-SnS**

H. Laurell*, K. Xiong*, **N. Ouahioune***, T. K. Jensen*, J. R. Adelman, K. J. Gannan, R. Quintero-Bermudez, L. Verbitsky, H. K. D. Le, A. Mikkelsen, P. Yang, C. Hägglund and S. R. Leone
Submitted

V **Ultrafast photoemission from InP nanowires mediated by local optical field enhancement**

N. Ouahioune, M. Saini, E. Östberg, Z. Zhao, T. K. Jensen, C. Juliano, N. Zaiats, M. Gisselbrecht, C. Guo, A-L. Viotti, C. L. Arnold, C. Verdozzi and A. Mikkelsen
Manuscript

VI **Quantum beats: Finite pulse effects**

S. Eriksson, P. K. Maroju, S. Carlström, D. Hoff, **N. Ouahioune**, E. M. Kjaersdam Telléus, S. Mikaelsson, A. L'Huillier, C. L. Arnold and M. Gisselbrecht
Manuscript

Abbreviations

APT	Attosecond Pulse Train
ATAS	Attosecond Transient Absorption Spectroscopy
ATRS	Attosecond Transient Reflection Spectroscopy
ATI	Above-Threshold Ionization
BBO	Beta-Barium Borate
CB/CBM	Conduction Band/Conduction Band Minimum
CMA	Central Momentum Approximation
CPA	Chirped Pulse Amplification
CEP	Carrier-to-Envelope Phase
CIEL	Coïncidences entre Ions et Électrons Localisés
DLD	Delay-Line Anode Detector
d-scan	dispersion scan
EWP	Electron Wavepacket
GD	Group Delay
GDD	Group Delay Dispersion
HeNe	Helium-Neon
HHG	High-order Harmonic Generation
IR	Infrared
LAP	Laser-Assisted Photoionization
MCP	Microchannel Plate
NOPA	Non-collinear Optical Parametric Amplification
NIR	Near-Infrared
PAD	Photoelectron Angular Distribution
PEEM	Photoemission Electron Microscope
RABBIT	Reconstruction of Attosecond Beating by Interference of Two-photon transitions
SAP	Single Attosecond Pulse
SATI	Stereo-Above-Threshold-Ionization
SHG	Second Harmonic Generation
SFA	Strong-Field Approximation
TDPT	Time-Dependent Perturbation Theory
TDSE	Time-Dependent Schrödinger Equation
TOF	Time-of-flight
TOD	Third Order Dispersion
TR-PEEM	Time-Resolved PEEM
VB/VBM	Valence Band/Valence Band Maximum
WD	Wigner Distribution
XUV	Extreme Ultraviolet

Contents

Part I: Thesis

CHAPTER 1

Introduction

1 Time-resolved electron spectroscopy

Light–matter interactions have long been a central area of research, driven both by their fundamental importance and their wide range of applications to study and control matter. Progress in this field has been closely tied to the development of light sources, enabling ever more precise ways to probe matter. It is well-known that shining light on matter may lead to the absorption of one or several photons, thereby promoting an electron to a higher bound energy level (photoexcitation) or to a free continuum state (photoemission). These processes are associated to a dynamic response of the system driven out-of-equilibrium. For example, photoexcitation is followed by radiative and/or non-radiative relaxation to lower excited states while in photoemission, the electron is emitted with a delay due to scattering with neighboring charged particles. Information about the electronic response can be obtained by measuring an observable impacted by the electron interaction (light spectrum) or a property of the electron itself (energy, momentum, spin, etc...).

A widely used detection method consists in photoemitting electrons using light, then detect their kinetic energy (i.e. spectrum), which is referred to as electron spectroscopy. Depending on the exact light parameters (frequency, field strength) and matter properties (binding energy), the photoemission takes place in different regimes. If the photon energy exceeds the binding energy, single-photon ionization occurs, as illustrated in Fig. 1.1a. This is called the photoelectric effect, which was first observed by Hertz [1] and explained by Einstein [2]. For high-frequency and/or weak fields, nonlinear absorption of multiple photons having a total energy exceeding the binding energy is also possible, as shown in Fig. 1.1b. In contrast, intense fields give rise to tunnel ionization in which the Coulomb potential is distorted by the field strengths, lifting the need for having a total energy

exceeding that binding the electron to the atom. This process is illustrated in Fig. 1.1c.

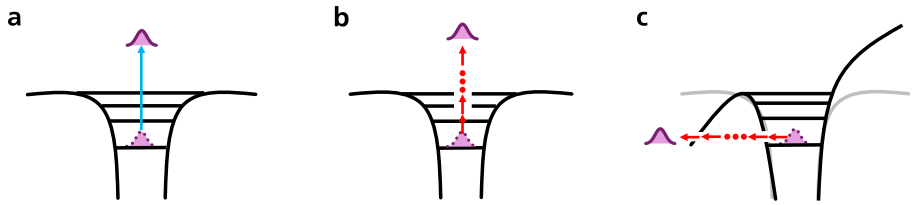

Figure 1.1: Main photoemission regimes. (a) Single-photon ionization with a high energy photon. (b) Multiphoton ionization, possible for long wavelengths. (c) Tunnel ionization. Each arrow represents the absorption of a photon and the purple gaussian area represents the electron wavepacket.

Nowadays, it is possible to generate laser pulses with femtosecond durations (1 femtosecond = 10^{-15} second), which exhibit broadband spectra in various regions of the electromagnetic spectrum and can be focused to high peak intensities. This enables reaching the three aforementioned photoemission regimes, which is done in the various applications of this work. However, measuring the spectrum provides incomplete information, as it does not directly access the phase of the photoelectron which carries temporal information.

Time-resolution is obtained by means of pump-probe interferometry. In this scheme, a pump pulse initiates the phenomenon of interest (e.g. photoexcitation or photoemission) which is then probed by a variably delayed pulse. It was implemented to study nuclear dynamics in molecules with femtosecond laser pulses by Ahmed Zewail, for which he was awarded the Nobel Prize in 1999 [3]. This method has since been extended to the study of numerous phenomena in molecules or solids in spectral regions ranging from the deep ultraviolet to the mid-infrared.

Yet, electron dynamics in atoms occur on even shorter timescales: attosecond ones (1 attosecond = 10^{-18} second). Furthermore, binding energies of ground state atoms or of core-levels in molecules and solids reach extreme ultraviolet (XUV) or X-ray energies, inaccessible with femtosecond pulses. With the advent of attosecond science, accessing electron dynamics involved in these phenomena became possible.

2 The realm of attosecond spectroscopy

Attosecond science emerged in the late 1980s, when scientists discovered that focusing an intense laser in a gas produced a broad comb of odd high-order harmonics of the laser frequency [4, 5]. This process, called high-order harmonic generation (HHG), gave access to a broad spectral range in the XUV or even X-ray region, compatible with attosecond durations. Since then, HHG has become a common technique to generate attosecond pulses, often in two main forms: long attosecond pulse trains (APTs) or single attosecond pulses (SAPs). As it is the natural time scale on which electrons move, each type of XUV radiation has revolutionized the study of electron dynamics in matter. Among its numerous successes, these could be used to measure photoionization time delays in atoms [6, 7, 8, 9], molecules [10, 11, 12] and condensed matter [13, 14] or to investigate sub-femtosecond dynamics of core excitons [15, 16, 17, 18]. More recently, large efforts of the community

are dedicated to develop protocols for characterizing the temporal evolution of the quantum state of electrons [19, 20, 21] or to extend the already existing metrology schemes [22, 23, 24].

The richness of applications arises from the immense choice in light sources, and their possible manipulation, but also detectors, which give access to more observable hence new information about the electron dynamics. Thus far, attosecond science has mostly combined XUV SAPs or APTs with phase-locked infrared (IR) laser pulses while detecting either charged particles or light.

When light-detection is chosen, attosecond transient absorption or reflection spectroscopy (ATAS or ATRS) dominates [25, 26, 27, 28, 29, 30], although alternative methods exist such as four-wave mixing [31, 32]. This thesis has used ATAS to investigate relaxation dynamics of photoexcited electrons. Here, an IR laser is used as a pump to induce changes in a sample, through which a XUV probe is propagated. The transmitted XUV spectrum is recorded, and provides information about the out-of-equilibrium dynamics. These all-optical techniques are in generally favored to study liquids or solids, which can be challenging with charged particle detection. This is especially pronounced in solids composed of several elements of the periodic table for which ATAS is more easily implemented.

When electron-detection is chosen, two cornerstone techniques dominate: streaking [33, 34, 35] and the Reconstruction of Attosecond Beating By Interference of Two-photon Transitions (RABBIT) [36, 37]. Both can be described as multiphoton processes (see Fig. 1.1a and b). RABBIT consists in using a weak IR probe to create quantum interference between electron wavepackets (EWP) produced through photoionization by the XUV. The amplitude and phase of the interference encodes information about the light fields or photoionization process. However, the subset of accessible variables is restricted and generally requires prior knowledge about the process itself or the light fields to disentangle the different contributions, especially in complex systems [38]. Besides, the complexity of this approach increases when broadband pulses are employed such that this implementation has been often avoided by the community. In this thesis, a robust study is carried out with the aim to lay the foundation for the interpretation of measurements using broadband fields and to leverage them as a more powerful metrology tool to study complex systems.

3 Scope of this work

Broadly, this work has been devoted to the study of ultrafast electron spectroscopy using broadband few-cycle laser pulses and short APTs -down to nearly SAPs. Since such studies intrinsically involve complex effects that are highly sensitive to the light source properties and detection methods, different approaches were employed, as illustrated in Fig. 1.2.

In the first part of this thesis, efforts were dedicated to improve the understanding of the few-cycle laser driven HHG light-source and its control. This system produces short APTs consisting of two to four attosecond pulses with different spectral and temporal properties. Their *characterization* is crucial for the photoemission-related applications since the light field properties impact the measurements.

A thorough study of HHG using laser-assisted photoioniziation (LAP) shows that both microscopic

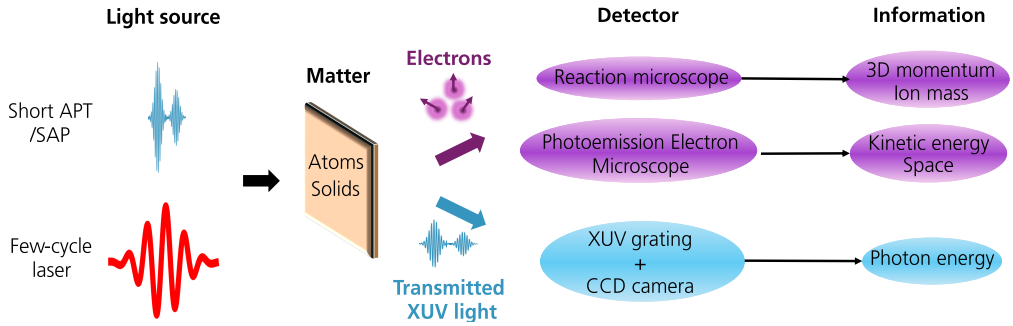

Figure 1.2: Overview of the light sources and detectors used in this thesis. Each combination of a light source and detector has its own scope of sensitivity.

and macroscopic aspects of the HHG process could change the number of pulses in the train in specific spectral ranges, due to the simultaneous effect of the carrier-to-envelope phase (CEP) of the laser and to time-dependent phase matching. This offers control capabilities for tuning the light source.

Other methods to control the XUV radiation consisted in manipulating the polarization of the few-cycle laser pulses driving HHG. In particular, the harmonic emission could be temporally confined to obtain continuous XUV spectra compatible with the generation of SAPs, which improves the versatility of the attosecond light source.

The second part of this thesis focused on using the attosecond and few-cycle pulses in *applications*. Two of them concentrated on interpreting and using broadband effects to extract new information in LAP whereas two others addressed various phenomena in light-solid interactions.

In the former, photoionization of helium using a comb of broad harmonics in the presence of a few-cycle laser field was studied using a reaction microscope which provided the three-dimensional momentum of the photoionized electrons. New observations are made arising from broadband effects. We propose a theoretical framework for LAP with broadband light fields, which is essential for extending these studies to more complex systems. A method to reconstruct the full quantum state of highly excited states via photoionization is also benchmarked in helium.

Finally, dynamics in semiconductors were investigated using two different techniques. First, an ATAS set-up combining few-cycle lasers and SAPs with a XUV spectrometer (in blue in Fig. 1.2) enabled identifying carrier cooling and recombination dynamics in a cubic tin(II) sulfide (π-SnS) semiconductor. The importance of this work relates to the identification of several carrier relaxation regimes, highly relevant for photovoltaic applications. In addition, it emphasizes the potential of this technique to study complex solids composed of several atoms.

An energy-resolved photoemission electron microscope (PEEM) was also installed to carry out time-resolved measurements of photoemission from indium phosphide (InP) nanowires directly with the few-cycle laser pulses. This work demonstrates that ultrafast production of electrons with broadband energy spectra, compatible with sub-femtosecond duration (several hundreds of attoseconds), can be localized at the edges of the wires.

4 Papers and outline

This thesis is based on six papers, which are connected to the use of few-cycle lasers and short APTs for the investigation of electron dynamics. These can be divided into two categories:

(1) Temporal confinement of the high-order harmonic emission driven by few-cycle lasers, and its characterization (**Papers I and II**).

(2) Electron spectroscopy with few-cycle lasers and short APTs (**Papers III-VI**).

Papers I and II investigate two mechanisms to confine the high-order harmonic emission driven by few-cycle laser pulses. In **Paper I**, the time-dependent polarization state of few-cycle laser pulses is tailored to confine the high-order harmonic emission. We find that oblique reflections which transport the polarization-gated pulses to the HHG target detrimentally alter the polarization-gate. We pre-compensate this effect and demonstrate a CEP-dependent confinement of the XUV emission. In **Paper II**, we generate short APTs with few-cycle laser pulses for different laser CEPs and characterize them using LAP. The spectra exhibit an energy-dependent number of attosecond pulses, which depends on the CEP-dependent single-atom response. We also show that the number of pulses is non-trivially impacted by XUV confinement due to phase matching dynamics.

LAP of helium atoms using a comb of broad harmonics in the presence of a few-cycle dressing laser field is performed in **Papers III and VI**. In **Paper III**, a three-dimensional electron momentum detector enables the identification of four new interference features in the photoelectron spectra, arising from interference between quantum pathways of different parities. These are distinguished and encode unique information about the light fields and photoionization process. **Paper VI** focuses on interference involving below-threshold excited states. In particular, we find that the broad bandwidths of our few-cycle laser pulses enrich the measurement, although they require careful analysis.

Papers IV and V focus on the ultrafast spectroscopy of semiconductor materials. In **Paper IV**, an ATAS set-up from the Stephen R. Leone group in Berkeley is used to investigate charge carrier dynamics in a metastable cubic phase of SnS. The dynamics are studied under different photoexcitation conditions, which enables identifying different carrier cooling and recombination regimes. **Paper V** presents a energy- and time-resolved study of photoemission from InP nanowires using few-cycle laser pulses and a PEEM. Due to local field enhancement, the photoelectron kinetic energy spectra exhibit features typical of the strong-field regime. These present broad bandwidths compatible with ultrashort durations, down to the attosecond regime.

This thesis is organized into four chapters. Chapter 2 introduces the fundamentals of few-cycle laser pulses as well as the experimental laser source and pulse-manipulation tools used in this work. In Chapter 3, theoretical and experimental HHG driven by few-cycle lasers is described. Based on these notions, two different mechanisms to confine the high-order harmonic emission are discussed. Chapter 4 focuses on angularly-resolved LAP with short APTs and few-cycle pulses, and compares it with the traditional RABBIT and streaking techniques. It is shown that this regime gives rise to new observations, which open the road to many possible studies. Finally, Chapter 5 presents two different time-resolved methods for ultrafast spectroscopy of solids (ATAS and TR-PEEM) and provides an example of application for each of them.

CHAPTER 2

Few-cycle laser pulses and their manipulation

The experimental techniques used in this thesis, in particular high-order harmonic generation and pump-probe interferometry, rely on the coherent properties of the light. The first section introduces the basic tools required to understand these measurements. Then, few-cycle laser pulses and methods applied to manipulate their properties are described, in view of the use of these tailored pulses for light-matter interactions in the next chapters.

1 Light pulses

Light-matter applications are often described by treating light either as an oscillating electromagnetic wave or as a photon. Both descriptions are valid, although physical intuition may come more naturally from one or the other depending on the situation.

Light oscillating at a single frequency ν is infinite in time and is referred to as monochromatic. Such waves constitute the building block of laser pulses. This is depicted in Fig. 2.1a, where monochromatic waves with different frequencies and a constant phase relationship are added, leading to a main peak with large amplitude. The pulse duration $\Delta\tau$ is as short as it can be, and the pulse is said to be Fourier limited. In contrast, Fig. 2.1b shows the superposition of monochromatic waves with random phase relationships. The resulting waveform consists of small random amplitude fluctuations, and no main peak is distinguishable.

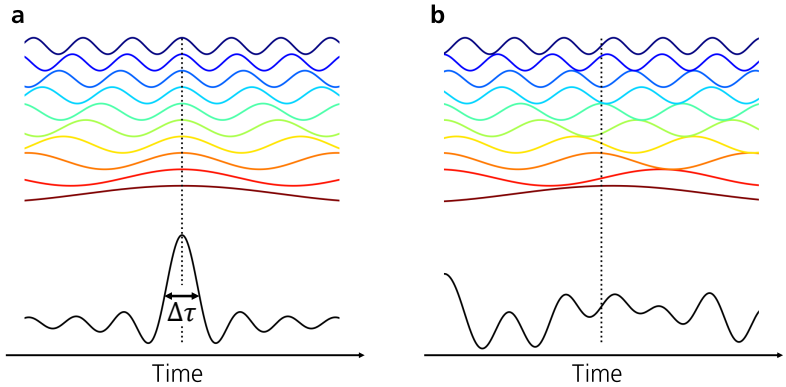

Figure 2.1: **Superposition of waves with different frequencies.** Superposition of N=10 monochromatic waves of different frequencies (blue to red curves) with a (a) fixed and (b) random phase relationship. In (a) the waves sum up to a well-defined main peak with a full-width at half maximum $\Delta\tau$ while in (b) their overlap leads to random intensity fluctuations of small amplitude.

All phenomena investigated in this thesis involve interactions with lasers, and rely on their coherent properties which means that the phase relationship is well defined over time. In the following sections, two concepts essential to the experiments in this work are introduced: spectral interferometry and multiple-slit interference.

1.1 Light pulses in the frequency and temporal domains

The measurements presented in this work are performed in the frequency domain, which is related to the temporal one through the Fourier transform pair:

$$\tilde{E}(\omega) = \int_{-\infty}^{+\infty} E(t) e^{-i\omega t}\, dt \quad \leftrightarrow \quad E(t) = \frac{1}{2\pi} \int_{-\infty}^{+\infty} \tilde{E}(\omega) e^{i\omega t}\, d\omega. \tag{2.1}$$

For laser pulses, the electric fields are conveniently expressed as complex quantities:

$$E(t) = |E(t)| e^{i\omega t + i\phi(t)} \quad \leftrightarrow \quad \tilde{E}(\omega) = |\tilde{E}(\omega)| e^{i\phi(\omega)}, \tag{2.2}$$

where $\omega = 2\pi\nu$ is the angular frequency, $|E(t)|$ the amplitude of the complex envelope, $|\tilde{E}(\omega)|$ the spectral amplitude with $|\tilde{E}(\omega)|^2$ being the spectrum, $\phi(t)$ the temporal phase and $\phi(\omega)$ the spectral phase.

Figure 2.2a and d present Gaussian Fourier limited pulses with a duration of 6 fs and 30 fs in the time domain. The envelope is plotted in red, and its maximum value E_0 corresponds to the electric field amplitude. The rapidly oscillating component, shown in black, is referred to as the carrier wave. Its oscillation frequency is approximately equal to the central frequency ω_0 of the spectrum with bandwidth $\Delta\omega$, shown in Figure 2.2b and e. The time and frequency being conjugate variables, broader bandwidths lead to shorter pulse durations.

The Fourier transform provides important insights about the spectrum of the entire pulse. However, two-dimensional spectrograms, which show the variations of the signal as a function of time and

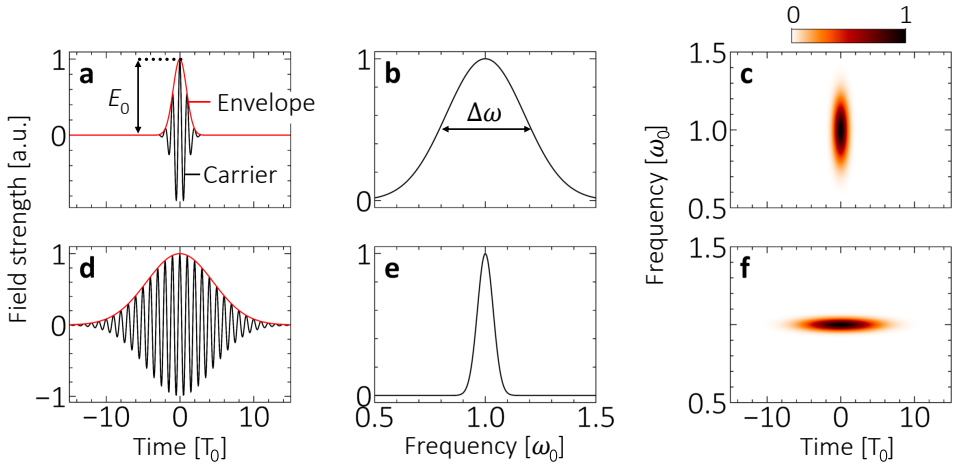

Figure 2.2: Common representations of light pulses. Electric field in the (a,d) time and (b,e) frequency domains of a 6 fs (top pannel) and 30 fs (bottom pannel) light pulse. (c,f) WD of the pulses. The time (frequency) axis is normalized to the laser period (central frequency).

frequency, provide a more intuitive representation of the spectral phase, especially when it strongly varies across the pulse envelope. The Wigner distribution (WD), given by

$$W(t,\omega) = \int_{-\infty}^{+\infty} E\left(t+\tfrac{\tau}{2}\right) E^*\left(t-\tfrac{\tau}{2}\right) e^{-i\omega\tau}\, d\tau, \tag{2.3}$$

provides a high spectral and temporal resolution. Here, different temporal slices of the pulse are auto-correlated. A drawback of this distribution is that non-physical cross terms can occur, which will be the case when simulating attosecond pulse trains in the next chapters. Those appear in-between consecutive components, and take on positive and negative values. The WD of the femtosecond pulses shown in Fig. 2.2a and d are displayed in c and f, respectively. The strong correlation between time and frequency is immediately accessible. Since the pulses are Fourier limited (constant spectral phase), the frequency is constant over time. The effect of a varying spectral phase is discussed later.

1.2 Spectral interferometry

Pump-probe experiments in this work aim at investigating light-matter phenomena over ultrashort time scales, which is not yet possible with electronic recording devices. Since the time domain is not accessible, a solution is to perform measurements in the frequency domain. Spectral interferometry was introduced to measure ultrashort laser pulses in the 1970s [39, 40]. It consists in measuring the spectrum resulting from the interference between two pulses delayed by τ, expressed as

$$I(\omega) = |\tilde{E}_1(\omega)|^2 + |\tilde{E}_2(\omega)|^2 + 2|\tilde{E}_1(\omega)||\tilde{E}_2(\omega)|\cos\left(\omega\tau + \Delta\phi\right) \tag{2.4}$$

where $\tilde{E}_1(\omega)$ and $\tilde{E}_2(\omega)$ are the two fields and $\Delta\phi$ their relative spectral phase. While the delay changes the periodicity of the fringes, the phase changes their position. Figure 2.3 compares the

spectra arising from the interference between two pulses delayed by τ (blue) and $\tau + \delta\tau$ (black dotted line) in time. In the former case, the interference pattern consists of peaks separated by τ^{-1}, and is modulated by the pre-factor $\tilde{E}_1(\omega)\tilde{E}_2(\omega)$. Increasing the delay between both pulses by $\delta\tau$ decreases the separation between the peaks in the spectral domain to $(\tau+\delta\tau)^{-1}$, as shown by black dotted lines. In this thesis (**Papers II, III, IV, V and VI**), light-matter interaction phenomena are investigated with methods building on the concepts of spectral interferometry.

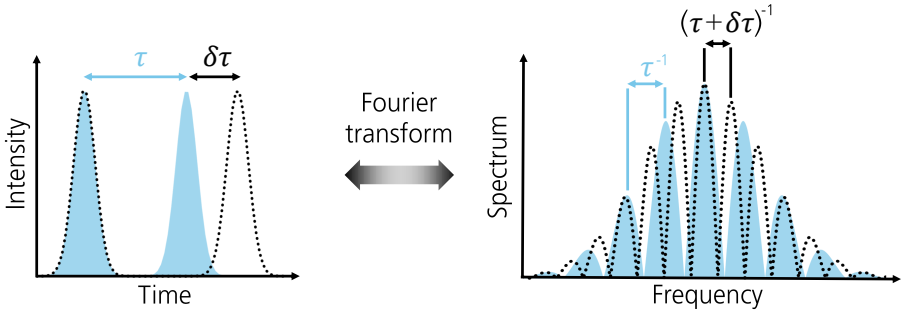

Figure 2.3: **Two-pulse interference.** Schematic of the spectrum arising from the interference between two pulses delayed by τ (blue) and $\tau + \delta\tau$ (black dotted line).

1.3 Multiple-pulse interference

Equation (2.4) shows that two light pulses separated in the temporal domain interfere in the spectral domain, even at large delays where they do not overlap. Certain processes, especially high-order harmonic generation, leads to the emission of pulse trains, composed of several pulses separated in time. Their spectrum can be understood in terms of multiple-pulse interference.

Figure 2.4 shows the spectrum of pulse trains composed of $N =$ (a) 3, (b) 5 and (c) 10 pulses separated by τ. We observe that the interference maxima become narrower as the number of pulses increases and that $N-2$ secondary maxima arise in-between the main peaks. In the case of three-pulse interference, the separation between the main peaks is half that between consecutive main peaks. Accordingly, the interference pattern can be intuitively thought of as the sum of interference patterns produced by each pulse-pair combination, as depicted in Fig. 2.4d. The secondary peaks can only originate from interference between the first and third pulse (gray curve) while interference between the second and first (or third) pulse leads to the main peaks (pink curve).

Breaking the time periodicity by slightly modifying the distance between two of the pulses allows controlling the position of the main or secondary maxima, thus breaking the symmetry of the pattern. Changing the phase of a pulse in the train leads to similar control possibilities. These concepts have strong consequences for high-order harmonic generation with few-cycle laser pulses.

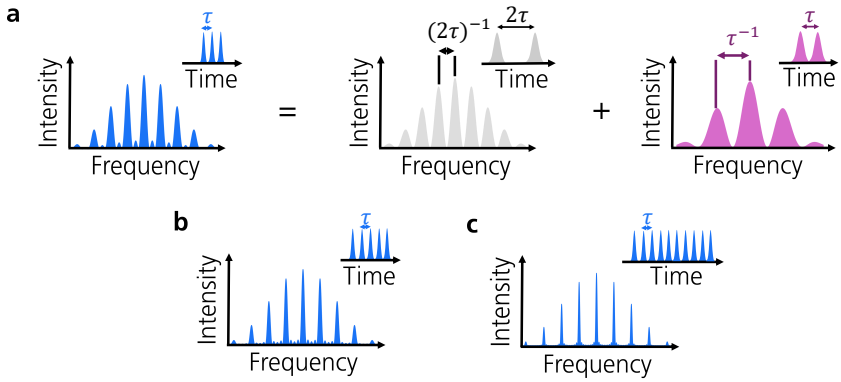

Figure 2.4: Multiple-pulse interference. Spectra of pulse trains composed by (a) three, (b) five and (c) ten pulses separated by τ in the temporal domain. The spectra can be thought as the sum of interference between all possible pulse pairs.

2 Few-cycle laser pulses

Nowadays, it is possible to reach pulse bandwidths of several hundreds of nanometers, that can support pulses as short as a few optical periods $T_0 = \frac{2\pi}{\omega_0}$. In this thesis, ~6 fs near-infrared (NIR) pulses are used, which contain two to four optical cycles. Most of the optical elements used to manipulate the light pulses are chromatic, meaning that they have a frequency-dependent refractive index $n(\nu)$. Since the speed of each frequency component in the medium depends on the refractive index, the various frequencies that make up the pulse propagate at different speeds resulting in a frequency-dependent phase. As discussed in the previous section, shorter pulses are obtained for temporally correlated waves. This makes the control of the phase a challenging but crucial requirement to achieve very short pulse durations.

An intuitive understanding of the means by which dispersion affects the pulses can be obtained by expanding the spectral phase in a Taylor series around the central frequency ω_0

$$\phi(\omega) = \underbrace{\phi_0^{(0)}}_{\text{CEP}} + \underbrace{\phi_0^{(1)}}_{\text{GD}}(\omega-\omega_0) + \frac{1}{2!}\underbrace{\phi_0^{(2)}}_{\text{GDD}}(\omega-\omega_0)^2 + \frac{1}{3!}\underbrace{\phi_0^{(3)}}_{\text{TOD}}(\omega-\omega_0)^3 + \ldots \tag{2.5}$$

where $\phi_0^{(n)} = \frac{d^n\phi}{d\omega^n}|_{\omega=\omega_0}$, $\phi_0^{(0)}$ the carrier-to-envelope phase (CEP), $\phi_0^{(1)}$ the group delay (GD), $\phi_0^{(2)}$ the group delay dispersion (GDD) and $\phi_0^{(3)}$ the third order dispersion (TOD). These terms are described in more details in the next sections.

2.1 Carrier-to-envelope phase and stereo-above-threshold ionization

The CEP corresponds to the absolute phase of the electric field oscillations with respect to the peak of the envelope. The electric field of a 6 fs pulse having three CEP values separated by 45° is plotted in Fig. 2.5. At a CEP of 0° and 90°, the carrier is symmetric with respect to the peak of the envelope (t=0) and oscillates as a cosine and a sine, respectively. For in-between CEP values, for

example 45°, the carrier is asymmetric with respect to the peak of the envelope. Applications using few- or single-cycle pulses, like HHG or above-threshold ionization (ATI), are highly sensitive to the instantaneous electric field. This requires a stable, and ideally controllable CEP.

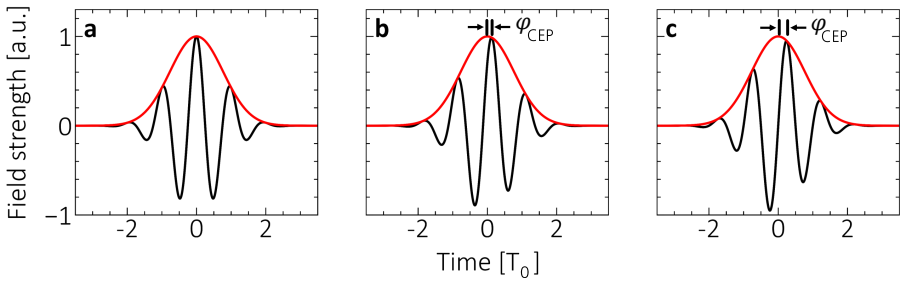

Figure 2.5: Carrier-to-envelope phase. Electric field of a 6 fs light pulse with a CEP equal to (a) 0°, (b) 45° and (c) 90°.

During propagation in dispersive media, however, the envelope and the carrier propagate at different speeds, resulting in a timing mismatch. This leads to CEP shifts $\Delta\varphi_{\mathrm{CEP}}$. Similar effects can also occur upon light reflection, depending on the light polarization state, which effect on HHG is studied in **Paper I**. Such aspects, in practice detrimental, offer means to control the CEP. For example, the thickness of BK7 or fused silica wedges can be adjusted to stabilize, shift or control the CEP of NIR pulses.

In **Papers I, II and III**, the CEP is locked using the stereo-above-threshold-ionization (SATI) technique [41], schematically illustrated in Fig. 2.6. Few-cycle laser pulses are tightly focused to high peak intensities ($\sim 10^{13}$ W/cm^2) into a xenon gas, resulting in photoionization. The field asymmetry is transferred to the photoelectrons, which are detected in opposite directions parallel to the field polarization. Their time-of-flight t_{TOF} (energy) is measured and a filter is applied on photoelectrons with high energies, that are more sensitive to the asymmetry.

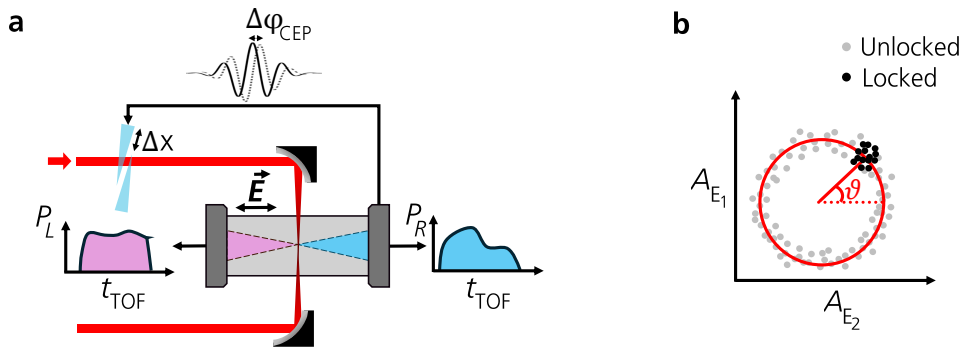

Figure 2.6: CEP-locking with the SATI. (a) Set-up of the SATI system. Few-cycle pulses (red) are focused into the SATI, where photoionization of xenon occurs. The photoelectron kinetic energy is detected in two opposite directions, and resulting asymmetry signal is analyzed by a feedback loop that controls a wedge pair located before the SATI. (b) Polar graph of asymmetry parameters for two different photoelectron energy slices. The gray and black points show the asymmetry parameters at each laser shot when the CEP is unlocked and locked, respectively.

The photoelectron counts detected by each detector (P_L and P_R) yield an asymmetry parameter $A = (P_L - P_R)/(P_L + P_R) \propto \cos(\varphi_{\mathrm{CEP}} + \phi_0)$, which presents sinusoidal variations with the CEP. The phase ϕ_0 of oscillations being energy-dependent, two energy slices are taken and optimized to obtain a relative 90° phase difference. These are plotted in a two-dimensional graph that takes the form of a circle, where the polar angle ϑ is the CEP. The distribution is shown in Fig. 2.6 for an unlocked (gray points) and a locked (black points) CEP. Long-term CEP drifts lead to a change in polar angle, which can be actively compensated for by a feedback loop that moves a wedge pair upstream the SATI. This can also be used to shift the CEP by a known amount. The SATI provides a CEP stability of around 160 mrad (corresponding to a precision of 10°).

2.2 Higher-order terms and dispersion scan

The first order term $\phi^{(1)}$ in Eq. (2.5) is a group delay, that is a temporal shift of the pulse. Since it does not affect the pulse duration, it is generally neglected. Higher order contributions, however, modify the pulse's shape, especially at the edges given the fast variations of $(\omega - \omega_0)^n$. In the bottom panel of Fig. 2.7, the WD of a 6 fs pulse having various spectral phases (shown in blue in the top panel) are plotted. In Fig. 2.7a and d, the reference Fourier limited pulse, having a constant phase, is shown. A GDD equal to 8 fs^2 is added in Fig. 2.7b. The corresponding WD, displayed in Fig. 2.7e, presents a frequency tilt that spans a larger temporal window than in d. Adding a second order phase term thus stretches temporally the pulse, thereby reducing its peak intensity. The GDD can be negative or positive, in which cases it induces a frequency decrease or increase with time, respectively. Sources of positive GDD are ubiquitous in optical set-ups and their effect must be balanced with special optics, such as chirped mirrors or grating compressors.

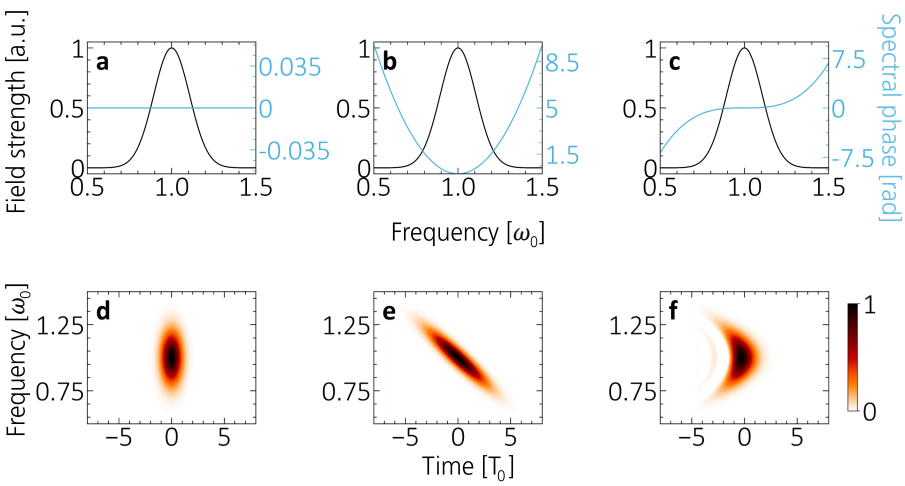

Figure 2.7: Effect of the spectral phase. (a-c) Graphs showing the spectral amplitude of a 6 fs pulse (in black) and the applied spectral phase (in blue). (d-f) Wigner distribution of the pulses in (a-c). The amplitudes are normalized in each graph and not scaled to the Fourier limited pulse.

In Fig. 2.7c, a positive TOD (5 fs^3) is applied, translating to a signature parabolic shape of the

WD, as seen in Fig. 2.7f. A pre-pulse also appears around -4T_0. Therefore, the TOD modifies the envelope shape by simultaneously stretching the pulse and separating the Gaussian tails from the main pulses, resulting in smaller pre- or post-pulses, depending on the TOD sign. This is very detrimental to the beam quality, as it affects the shape of the pulse on top of the duration.

For the experiments presented in this thesis, the aim is to obtain the shortest pulse duration possible. This is done by measuring the pulse duration with the dispersion scan (d-scan) technique, from which the presence of high order spectral phase terms can be inferred. A d-scan measurement consists in scanning the spectrum of a nonlinear signal for different material dispersion. The set-up is shown in Fig. 2.8a. First, the laser pulse to characterize is sent into a pair of dispersive wedges, where it acquires a spectral phase $e^{i\phi(\omega)}$, mostly a positive GDD. Optical elements with negative dispersion, like chirped mirrors, are introduced upstream to compensate the excess dispersion. The pulses are then focused in a nonlinear crystal, where their second harmonic is generated. The d-scan trace, which is the second harmonic signal as a function of the wavelength and wedge insertion Δx, is recorded with a fiber spectrometer. Second harmonic generation (SHG) being nonlinear, the signal's intensity is maximum when the pulse is optimally compressed. The electric field (amplitude and spectral phase) at each Δx is retrieved using an algorithm that minimizes the root mean square error between the measured and a simulated trace.

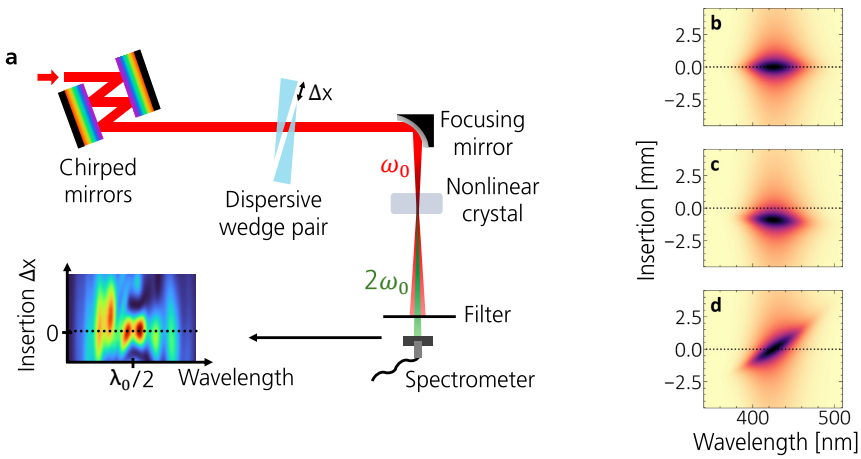

Figure 2.8: Dispersion scan. (a) Schematic of a typical d-scan set-up. Right panel: Simulated d-scan traces obtained for the second harmonic of a 6 fs pulse centered at 850 nm. D-scan trace, which shows the second harmonic signal as a function of the wedge insertion and wavelength, when the pulse is (b) Fourier limited, has (c) a positive GDD and has (d) a positive TOD.

In addition to providing the pulse duration, the d-scan provides an indication on whether high order phase terms are present, in which case the pulse duration is not Fourier limited. On the right of Fig. 2.8, the simulated d-scan trace for a 6 fs pulse at 850 nm with different spectral phases is shown. In Fig. 2.8b, the pulse is Fourier limited so the trace is flat and the signal maximum at $\Delta x = 0$. During experimental campaigns, we use various dispersive elements with the aim to obtain this type of trace, to ensure having the optimum pulse at the application target (HHG medium or ionization medium). In Fig. 2.8c, a positive GDD is applied to the pulse, which shifts the trace without strong modifications of the shape. Finally, a positive TOD leads to a tilt (see Fig. 2.8d), with a shape analogous to the WD showing the effect of GDD on the spectral phase in Fig. 2.7b-e.

It is important to note that the d-scan does not measure the CEP of the electric field.

3 Manipulation of the light polarization

A great number of applications depend on the light polarization, defined as the direction in which the electric field oscillates in space. Several methods exist to manipulate the polarization either spatially or temporally, enabling the investigation of symmetries in various types of matter or the control of light-matter interactions on ultrafast time scales [42]. For instance, tailored polarization in ultrashort light pulses has opened promising research fields, including the ultrafast engineering of electronic states in materials [43, 44, 45] or the generation and control of strong magnetic fields on ultrafast timescales [46, 47].

In the context of this thesis, the polarization of few-cycle laser pulses is manipulated in time to control the XUV radiation generated via HHG. Specifically, the polarization gating technique, which consists in confining a specific polarization state (linear) in a narrow temporal window, is implemented. Means to create a polarization gate for reducing the duration of produced XUV pulses have been widely developed since the early 1990s [48, 49, 50, 51, 52, 53]. In this section, a beginner's guide on how to use propagation in birefringent materials to manipulate the polarization in time is given. It then presents the set-up implemented to create polarization-gated few-cycle pulses in **Paper I**, including key experimental challenges.

3.1 Control of the polarization through birefringence

According to Jones formalism, the electric field vector can be decomposed into orthogonal components with amplitudes E_i (i=x,y) having a relative phase $\Delta\phi = \phi_y - \phi_x$:

$$\mathbf{J} = \begin{bmatrix} E_x \\ E_y e^{i\Delta\phi} \end{bmatrix}. \tag{2.6}$$

The tip of the electric field vector traces an ellipse during light propagation, as shown in Fig. 2.9. The shape is determined by the two angles ψ and χ:

$$\tan(2\psi) = \frac{2R}{1-R^2}\cos(\Delta\phi), \tag{2.7}$$

$$\tan(2\chi) = \frac{2R}{1+R^2}\sin(\Delta\phi) \tag{2.8}$$

with $R = E_y/E_x$ being the components' amplitude ratio. The exact shape defines the polarization state, which is classified into three types: circular when the ellipse is a circle ($R = 1$ and $\Delta\phi = \pi/2$), linear when the ellipse folds onto a plane and elliptical otherwise.

It follows that the polarization can be manipulated via optical elements that control R and/or $\Delta\phi$. A widely used approach is to employ birefringent materials, in which light possesses an anisotropic

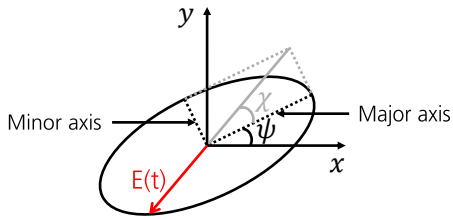

Figure 2.9: Polarization ellipse. Ellipse drawn by the electric field tip vector over its course. The exact shape is solely determined by the angles ψ and χ.

refractive index such that orthogonal field components propagate at different velocities. This results in a relative phase expressed as

$$\Delta\phi(\omega) = \frac{\omega}{c}\Delta n(\omega)d, \tag{2.9}$$

where d is the thickness of the crystal and Δn is the difference between the refractive indices. The value of Δn depends on the material and on the crystal orientation. In **Paper I**, uniaxial crystals are used, which can be oriented such that light linearly polarized along a so-called ordinary x_o and extraordinary x_e axis has a refractive index equal to the ordinary n_o and extraordinary n_e indices, respectively. By tuning the thickness, one can finely control the phase shift and thus the polarization. For example, quarter-wave plates introduce a phase shift of $\pi/2$, enabling conversion between linear and circular polarization.

For ultrashort pulses, birefringence has an additional crucial consequence. Since the orthogonal components propagate at different velocities, they become temporally delayed with respect to each other. In their overlap region, the polarization becomes time-dependent because the amplitude varies within the individual components pulse envelopes.

3.2 Experimental set-up for polarization gating

The in-line polarization gate set-up implemented in **Paper I** uses two birefringent plates made of fused silica, as schematically illustrated in Fig. 2.10. First, the pulse that is linearly polarized over the entire duration is transmitted through a quarter waveplate (QWP1). When the ordinary (or extraordinary) axis is oriented parallel or perpendicular to the field, the polarization remains linear. To create the polarization gate, one of the axes of QWP1 is instead oriented at an angle θ_1 with respect to the input field. This results in two orthogonal, delayed replicas of the input pulse.

At the time where the amplitudes of the two components is equal, the polarization is circular. Away from this time, the polarization becomes increasingly elliptical since $R = |E_e|/|E_o|$ decreases. Rapidly, R=0 and the polarization is linear. Finally, linear polarization at the position of the polarization gate is desirable so another quarter waveplate (QWP2) is inserted at an angle $\theta_2 = \theta_1 - 45°$.

Figure 2.11 illustrates the delayed orthogonal field replica for two different angles of QWP1. The relative amplitudes between the orthogonal components is different in both cases, as seen in Fig. 2.11a-b. However, the phase difference is fixed, as it is solely determined by the thickness and refractive

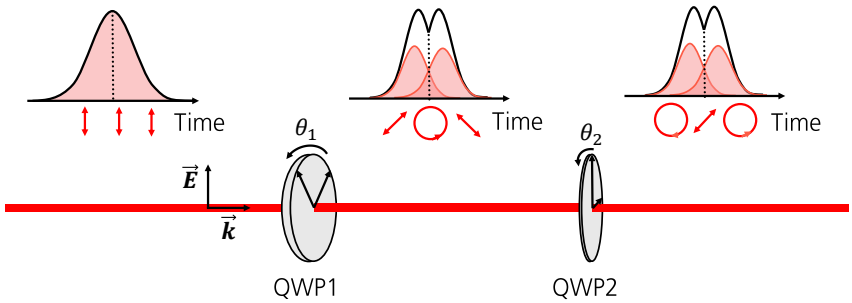

Figure 2.10: **Polarization gating.** Schematic of the polarization-gate setup implemented in **Paper I**. Linearly polarized pulses are split into two delayed orthogonally polarized components by a first quarter waveplate (QWP1), producing a time-varying polarization state. A second quarter waveplate (QWP2) is used to obtain circular polarization at the peak of the output pulse envelope.

indices of the material. As a result, the polarization gate position t_{PG} changes since R=1 occurs at different times for the two angles, as seen in Fig. 2.11c-d.

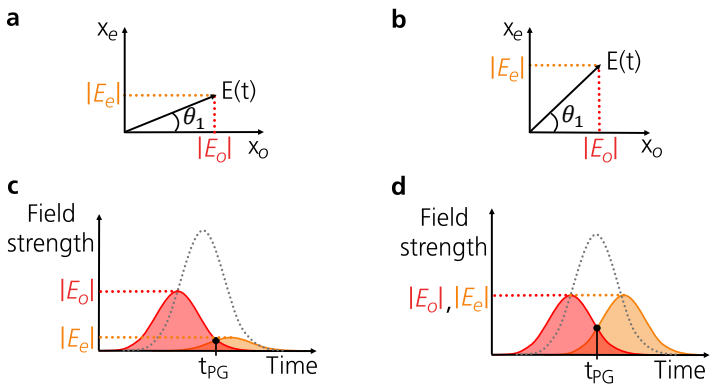

Figure 2.11: **Manipulation of the polarization gate position.** Principle schematic of a polarization gate generated at different times t_{PG} in the pulse by changing the angle θ_1. (a,b) Input electric field orientation with respect to the principal axes of the first quarter waveplate. (c,d) Delayed replica of the input field (red and orange) after propagation in the quarter waveplate. The input electric field envelope is indicated with a gray dotted line.

In Fig 2.12, we plot a simulation of the output electric field strength (in black) and of the degree of ellipticity $\tan(\chi)$ (in blue) at the output of two fused silica waveplates with thickness 16.5 mm and θ_1=10° and 45°. We observe that the ellipticity varies mostly linearly with time and reaches zero at different times for different angles. Furthermore, the gate spans less than an optical period, enabling efficient temporal confinement of the linear polarization. The exact number of covered half-cycles depends on the CEP, which is found to have an effect when the gated pulse is used for high-order harmonic generation in **Paper I**.

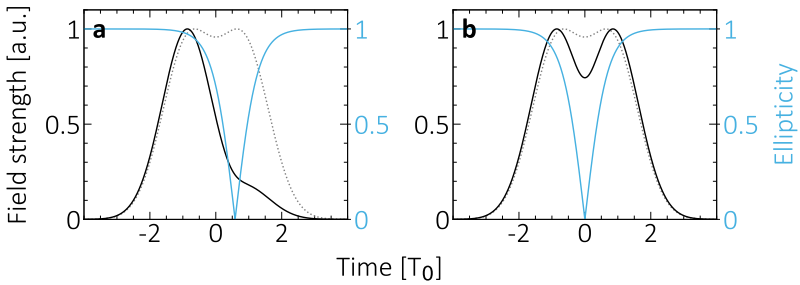

Figure 2.12: **Temporal properties of the polarization gate.** Polarization gate generated at different times by changing the angle θ_1 between the electric field and the ordinary axis x_o of QWP1. Simulated electric field strength at the input (in gray) and at the output (in black) of two fused silica waveplates at (a) θ_1=10° and (b) 45°. The degree of ellipticity is plotted in blue.

3.3 Design challenges

In most experiments, the polarization-gated pulse is created upstream of the application chamber (HHG target), such that coated reflective optics (e.g. mirrors) are used to transport the pulse to the application target. However, reflection is polarization-dependent: the electric field components parallel and perpendicular to the plane of incidence, known as *s*- and *p*-polarization, experience different amplitude and phase changes. For a pulse which is linearly polarized throughout its duration, the field is either *s* or *p* polarized, and reflection does not alter its polarization state. In contrast, a pulse having a time-dependent polarization state always has a total electric field that can be decomposed into a *s*- and a *p*- component, whose relative amplitude and phase changes with time. Upon reflection at oblique incidence, these components are modified differently, thereby changing the polarization state.

Even though the absolute phase shifts introduced by the reflections is small, it becomes non-negligible for few-cycle pulses. In this thesis, we drive high-order harmonic generation with polarization-gated pulses. However, the gate is created in air and then transported to the HHG medium via six reflections at 45° on coated metallic mirrors. **Paper I** shows that these reflections alter the time-dependent polarization to an extent that the gate is destroyed before reaching the HHG medium.

To address this issue, an in-line experimental arrangement, shown in Fig. 2.13, was developed to pre-compensate the reflection-induced dephasing. The gated pulses first pass through two pairs of wedges. Each pair is composed of a birefringent quartz wedge, BW1 and BW2, that have opposite insertion values ($\Delta x_{\mathrm{BW2}} = -\Delta x_{\mathrm{BW1}}$). The delay between the two orthogonal replica of the input pulse is finely controlled by changing the thickness. Since varying the thickness by just 0.1 µm yields a group delay [$|\tau_g| = \partial_\omega \Delta\phi(\omega)$] of approximately 3 as at 850 nm, an attosecond precision is possible.

To maintain a neutral dispersion (constant thickness), each birefringent wedge is coupled to a non-birefringent fused silica wedge (NW1 and NW2), that moves synchronously to compensate thickness variations ($\Delta x_{\mathrm{NWi}} = -\Delta x_{\mathrm{BWi}}$, with i=1,2). A specificity of this arrangement is that only positive delays can be achieved. Negative delays are obtained by adding two birefringent quarter waveplates (QWP3 and QWP4) that have their extraordinary and ordinary axes aligned but inverted

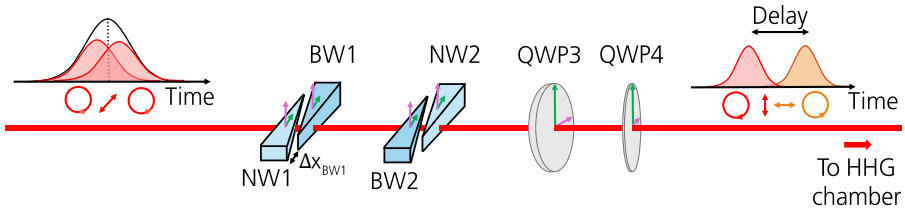

Figure 2.13: **Pre-compensation system.** Schematic illustrating the polarization control set-up. The polarization-gated pulses enter the unit from the left and propagate into two pairs of movable wedges consisting of birefringent quartz (BW1 and BW2) and non-birefringent fused silica (NW1 and NW2) wedges. Then, it propagates into two birefringent quarter waveplates (QWP3 and QWP4). Green and purple arrows indicate the extraordinary and ordinary axes, respectively.

to that of the wedge pairs.

4 Experimental generation of few-cycle optical pulses

In this thesis, most of the experiments (**Papers I, II, III, V, VI**) were performed in Lund using a laser system relying on optical parametric chirped pulse amplification (OPCPA) technology [54]. The laser set-up is presented in the following.

4.1 Optical Parametric Chirped Pulse Amplification

In general, chirped pulse amplification (CPA) [55] consists of three steps, illustrated in Fig. 2.14a. First, the pulses are temporally stretched by introducing a frequency-dependent phase, which reduces their peak intensity. This allows their subsequent amplification in a gain medium (amplifier) without causing damages. The amplified pulses are then compressed back to their initial duration by controlling the spectral phase, thus leading to a large peak intensity gain ΔI. While very reliable, CPA systems based on conventional bulk gain media, most often titanium-sapphire (Ti:Sa) crystals, suffer from thermal issues and a narrow amplification bandwidth. The heat issues lead to a trade-off between having a high repetition rate or a high pulse energy and the limited spectral ranges limit the minimum achievable pulse duration. For applications in this thesis, one wants to have intense few-cycle pulses (broad bandwidths) at a high repetition rate.

This is achieved with the OPCPA technique, which differs in that the amplification step is nonlinear, as illustrated in Fig. 2.14b. More precisely, non-collinear optical parametric amplification (NOPA) is used. Here, two light fields with different frequencies, called the seed (red) and the pump (green), are focused into a uniaxial Beta Barium Borate (BBO) crystal. When they are temporally and spatially overlapped, the BBO nonlinearity leads to frequency mixing, where different frequency components in the spectra are added or subtracted with each other thus producing new frequencies. In NOPA, energy from the pump is transferred to the seed and a third wave, called idler (rainbow colors), is produced. The overall process is sensitive to the phase relationship between the interacting beams.

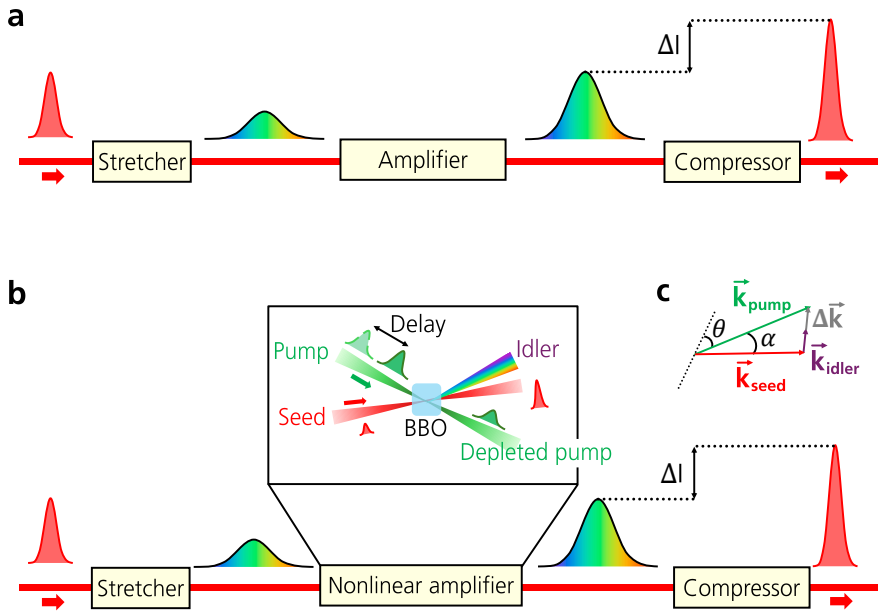

Figure 2.14: Amplification schemes used in the Lund laser system. Principle schematic of the (a) CPA and (b) OPCPA technique. The set-up in Lund uses NOPA, in which the pump and the seed are mixed noncollinearly, as seen in (c).

It can be shown that the phase matching condition for an efficient process is:

$$\Delta\mathbf{k} = \mathbf{k}_{\mathrm{pump}} - \mathbf{k}_{\mathrm{seed}} - \mathbf{k}_{\mathrm{idler}} = 0, \tag{2.10}$$

where $\mathbf{k}_{\mathrm{pump}}$, $\mathbf{k}_{\mathrm{seed}}$ and $\mathbf{k}_{\mathrm{idler}}$ are the wavevectors of the pump, seed and idler, respectively. The wavevector mismatch depends on the angle θ, between the pump beam and the crystal optical axis (dotted line), and the angle α, between the pump and seed beams, as illustrated in Fig. 2.14c. In practice, we adjust both angles to optimize phase matching when preparing the laser source for experimental campaigns. In this thesis, the maximum bandwidth which can be amplified is about a 300–350 nm with a central wavelength around 850 nm.

4.2 Laser system

The schematic of the complete experimental OPCPA set-up is presented in Fig. 2.15. It starts with a Ti:Sa oscillator providing pulses <6 fs. A dichroic mirror separates the beam into a broadband (640-1100 nm, in red) and a narrowband (at 1030 nm, in black) portions, that will become the seed and pump sources for the OPCPA. The narrowband pulses are stretched and amplified using a combination of fibers, which reduces the repetition rate from the MHz range to 200 kHz. The stretched pulses are then compressed by a pair of reflection gratings to a duration of ∼300 fs. The second harmonic of these pulses is generated with a SHG crystal while the remaining fundamental is damped by a dichroic mirror (DM). The second harmonic (in green) is used for pumping the OPCPA.

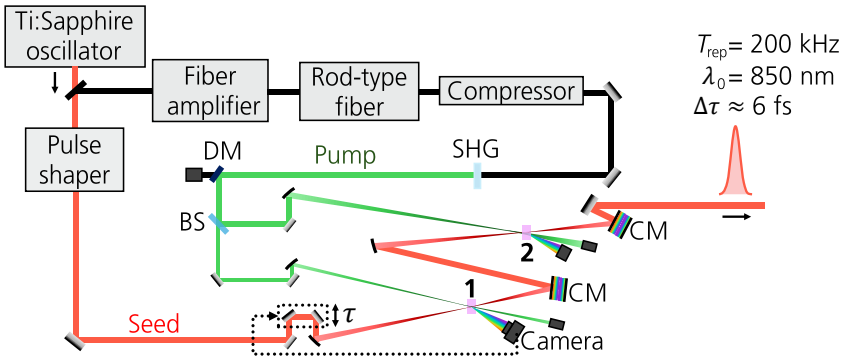

Figure 2.15: OPCPA laser system. Schematic of the OPCPA laser system. CM: chirped mirror pair. DM: dichroic mirror. SHG: Second harmonic generation. BS: beam splitter.

A beam splitter (BS) then separates the pump into two parts. The transmitted pump is focused into a BBO crystal (labeled 1) for nonlinear amplification. The reflected part is focused into another BBO crystal (labeled 2). In both BBO stages, the pump is spatially overlapped with the seed (in red). The temporal overlap is obtained via a delay stage in the seed arm, that is actively stabilized with a feedback loop that uses the angularly separated idler as a reference. Finally, the IR amplification (covered bandwidth and power) is optimized by applying high order terms of the spectral phase on the seed directly at the oscillator throughput using a pulse shaper. For example, the GDD and TOD can be individually changed following Eq. (2.5) to obtain the shortest pulse duration.

Figure 2.16a shows a typical output spectrum from the OPCPA. The spectrum has a structure composed of many peaks, with a center wavelength around 850 nm. The inhomogeneous shape of the spectrum has large implications for the photoionization experiments performed in **Papers III and VI**, which will be discussed in the next chapters. In Fig. 2.16b, the temporal profile and phase of the electric field, retrieved with the d-scan, is shown. A main pulse is visible, that has a duration <6 fs, with some pre- and post-pulses of smaller amplitudes. These additional small pulses have an impact for applications in solids, which is discussed in the context of photoemission electron microscopy in **Paper V**.

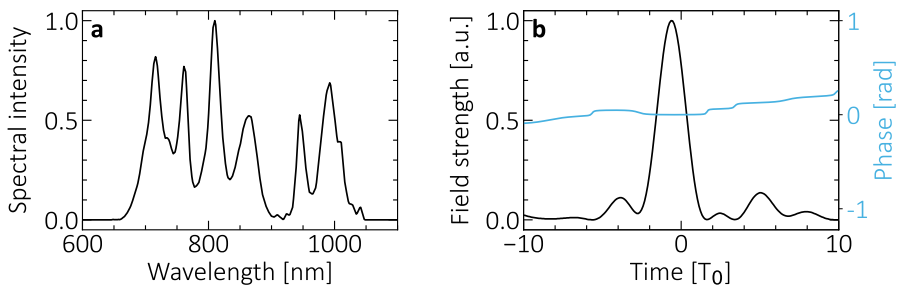

Figure 2.16: Experimental laser characterization. (a) Experimental spectrum at the output of the OPCPA. (b) Electric field amplitude (in black) and phase (in blue) retrieved from a second harmonic dispersion scan at the position of optimal wedge compression.

CHAPTER 3

Short attosecond pulse trains

This chapter studies high-order harmonic generation driven by few-cycle laser pulses, which is a nonlinear light-matter interaction used to generate attosecond pulses in the XUV range. First, we describe the spectro-temporal structure of attosecond pulse trains generated with high-order harmonic generation. Second, we put an emphasis on the spectro-temporal properties of attosecond pulses produced by a few-cycle driving pulse, as it is central to **Papers II, III and VI**. Finally, we discuss methods to control the attosecond pulse duration, in relation to **Papers I and II**.

1 Why generating short attosecond pulse trains?

In attosecond science, HHG is primarily used to produce SAPs or long APTs. Meanwhile, short APTs generated by few-cycle driving lasers are rarely used, even though they present unique spectral and temporal properties. A recent work has shown that the number of attosecond pulses in the train could be controlled by changing the CEP of the driving laser, providing means to manipulate ultrafast processes such as photoionization [56]. More generally, the CEP-dependence of strong-field physical phenomena has regularly been used as an effective control parameter, for example in pioneer works related to above-threshold-ionization [57] or photoemission from metallic nanostructures [58].

In this thesis, we exploit the spectral and temporal properties of short APTs to deepen the understanding of light-matter interactions. In **Paper III**, for instance, we demonstrate that employing short APTs in a laser-assisted photoionization scheme traditionally implemented with long APTs provides access to new experimental observables, as discussed in the following chapter. Moreover,

short APTs share some features with SAPs, in particular a broad spectrum. This makes them well suited for applications such as attosecond transient absorption spectroscopy, which is used in **Paper IV** to study charge carrier dynamics in a semiconductor. Finally, simple methods can be applied to reduce short APTs to SAPs. In **Paper I**, this is achieved by manipulating the polarization state of the driving laser pulses with the set-up described in Chapter 1.

Arguably, short APTs therefore combine many advantages of both types of XUV radiation. The following sections provide the theoretical and experimental tools about HHG driven by few-cycle laser pulses.

2 High-order harmonic generation

High-order harmonic generation is a nonlinear interaction between an intense laser field (from 10^{13} W/cm^2) and matter that leads to the generation of high-order harmonics of the laser field. Since its discovery in the late 1980s [4, 5], HHG is routinely used to produce coherent trains of attosecond pulses. Figure 3.1 shows the schematic of a typical HHG spectrum, in logarithmic scale. The spectrum is composed of peaks separated by twice the laser frequency, corresponding to odd high-order harmonics. Three distinct regions can be identified. First, the intensity decreases linearly with frequency ("perturbative regime"). This behavior is well-described by a Taylor expansion in the electric field strength E:

$$\alpha_1 E^1 + \alpha_3 E^3 + \dots \tag{3.1}$$

This decrease is followed by a plateau of constant intensity, which cannot be described with Eq. (3.1). Finally, a sudden drop in intensity arises, called "cut-off". To understand the origin of the plateau, the interaction between the intense laser field and the medium must be considered.

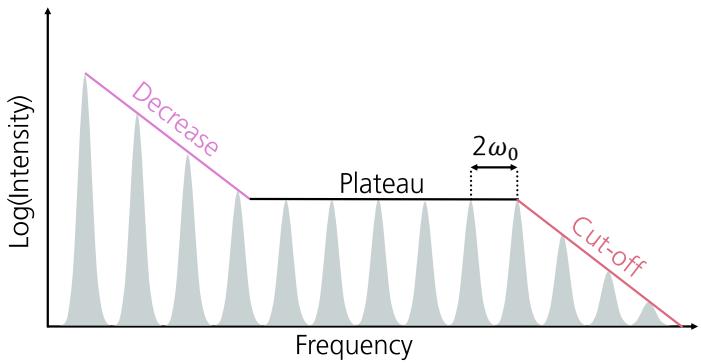

Figure 3.1: Schematic of a typical spectrum obtained with high-order harmonic generation in a gas. Logarithm of the relative intensity of high-order harmonics as a function of the frequency. Three distinct regions are indicated: a decrease in intensity, followed by a high-harmonic plateau persisting until a cut-off frequency, above which the intensity drops.

2.1 The three-step model

Many properties of the harmonic emission, including the spectral plateau, stem from the interaction between the laser field and a single-atom (microscopic response). This interaction is well described by a semi-classical model based on three steps [59, 60, 61], schematically illustrated in Fig. 3.2. First, the electric field distorts the Coulomb potential binding the electrons and the nucleus together, to such an extent that the electron can reach the continuum via tunneling. Since it requires large field strengths, this occurs at times close to a peak of the electric field. In the continuum, the electron is accelerated by the electric field, thus gaining kinetic energy. After a fraction of a period, the electric field sign changes and the electron is accelerated back towards its parent ion. There is a finite probability that it recombines, emitting the excess energy in the form of a high energy photon, typically in the XUV range.

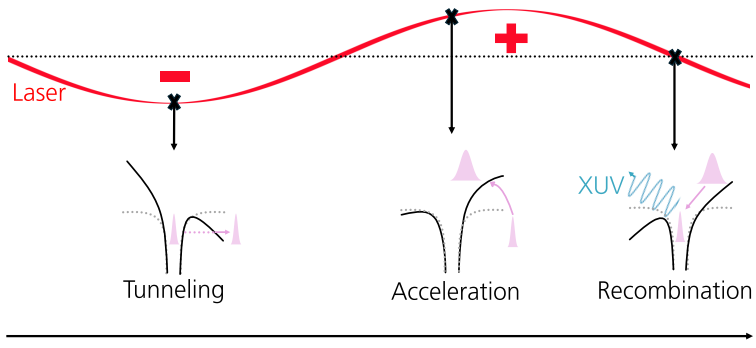

Figure 3.2: Schematic of the three-step model. Close to a peak of the laser electric field (in red), the distortion of the Coulomb potential (in black) is maximum. The electron can reach the continuum through tunnel ionization. It subsequently accelerates in the electric field, away from the ion, and then back, when the field changes sign. At last, it can recombine, and emit the excess kinetic energy in the form a high frequency photon (XUV or X-ray range).

The three-step model successfully predicts the maximum emitted photon energy, called cut-off energy [61, 62]:

$$E_c = I_p + 3.17U_p, \tag{3.2}$$

where I_p is the ionization energy of the atom and U_p the ponderomotive energy equal to $\alpha\hbar I/(m_e\omega^2)$, with $\hbar$ being the Planck's constant, q the harmonic order, m_e the electron mass and α the fine structure constant. The linear scaling with laser intensity and wavelength offers means to control the energy range.

According to this model, the process repeats itself each time the electric field changes sign, leading to trains of attosecond pulses separated by half the optical period, as illustrated on the left of Fig. 3.3. In the spectral domain (right), the spectrum consists of peaks separated by twice the laser frequency, analogous to multiple-pulse interference (see previous chapter). It is important to note that this model does not describe accurately important quantum aspects, included in the intensity-dependent single-atom dipole. In this thesis, the microscopic aspects of the APT generation are simulated by solving Eq. (3.5) and approximating the time-dependent dipole by a power law [$|d_q(t)|^2 = I^{2.6}(t)$] -valid in our intensity range [63, 64].

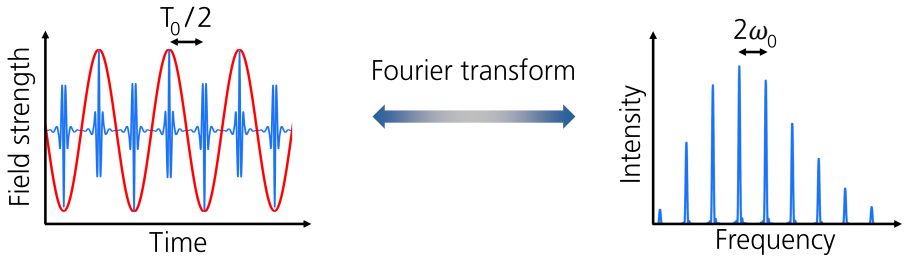

Figure 3.3: Temporal and spectral profiles of the high-order harmonic emission. Left panel: Electric field of an APT (blue) generated by an infinitely long driving laser (red). Right panel: Corresponding HHG spectrum.

2.2 Phase-matching

Although the single-atom response describes many of the harmonic emission properties, in reality, the laser propagates in a partially ionized medium composed of many atoms. The total harmonic field at the output of the medium is the coherent superposition of all emitted fields with a same frequency $q\omega$. The absence of phase relationship between these fields result in destructive interference that reduces the HHG yield, as schematically illustrated in Fig. 3.4a. For an efficient HHG process, the relative phases of the fields emitted by all the atoms must be "matched", see for example Fig. 3.4b. This is achieved by controlling the generation conditions such as to maintain a fixed phase relationship between the fundamental (generating) and harmonic (generated) field throughout the interaction length L_{gas}. This translates into the following "perfect phase-matching" condition:

$$\Delta\mathbf{k}(q) = q\mathbf{k}_0 - \mathbf{k}_\mathbf{q} = 0, \tag{3.3}$$

where $\mathbf{k}_0$ and $\mathbf{k}_\mathbf{q}$ are the wave vectors of the fundamental and XUV field, respectively.

In this thesis, HHG is performed in a gas, leading to four contributions to the total phase mismatch, originating from the focusing of the fundamental laser ($\Delta\mathbf{k}_{\mathrm{foc}}$), the microscopic generation process ($\Delta\mathbf{k}_{\mathrm{dip}}$), the dispersive neutral atoms ($\Delta\mathbf{k}_{\mathrm{at}}$) and the ionized electrons ($\Delta\mathbf{k}_{\mathrm{fe}}$). The total phase mismatch becomes:

$$\Delta\mathbf{k}(q) = \overbrace{\Delta\mathbf{k}_{\mathrm{at}}(q)}^{>0} + \underbrace{\Delta\mathbf{k}_{\mathrm{fe}}(q)}_{<0} + \overbrace{\Delta\mathbf{k}_{\mathrm{foc}}(q)}^{<0} + \underbrace{\Delta\mathbf{k}_{\mathrm{dip}}}_{>0 \text{ or } <0}(q). \tag{3.4}$$

Since the contributions have different signs, they can compensate each other to achieve perfect phase-matching [see Eq. (3.3)]. Finally, as each term depends on the harmonic order, phase-matching can lead to spectrally varying harmonic intensities, and thus plays a major role in the spectral and temporal properties of the harmonic emission.

The main message of this section is that the intricate time-frequency dependence of HHG arises from microscopic and macroscopic effects, which in turn depend on a multitude of variables, such as the laser parameters [see Eq. (3.2)] or the HHG target design [see Eq. (3.4)].

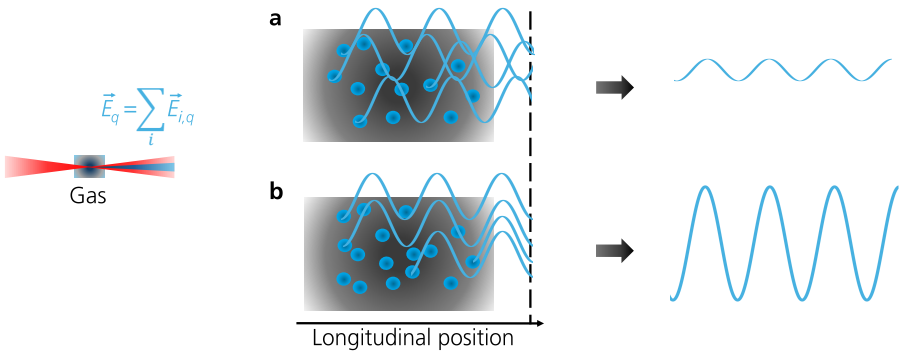

Figure 3.4: Schematic of phase-matching. Representation of the phase relationship between harmonic fields emitted by a multitude of atoms in a nonlinear medium. The emitted fields corresponding to a harmonic order q are (a) out-of-phase and (b) in-phase throughout the medium, resulting in a (a) small and (b) large amplitude.

3 Few-cycle driving pulses

Driving HHG with few-cycle laser pulses leads to fundamentally different XUV spectro-temporal properties than using long ones, due to their rapid intensity variations. Figure 3.5 shows the temporal (left panel) and spectral (right panel) profiles of the XUV radiation for a decreasing laser duration. Temporally, the number of attosecond pulses in the train decreases with the duration, due to the single-atom dipole dependence on intensity. Spectrally, this is associated to an increase in harmonic width. In the limit of a single attosecond pulse (bottom row), the spectrum presents a broad continuum, still modulated by twice the laser frequency due to the presence of two very weak satellite pulses.

In the following, the concepts introduced above are applied to few-cycle pulses, and used to develop a simple one-dimensional model of HHG driven by few-cycle lasers, which includes the microscopic and macroscopic response.

3.1 Electron trajectories in the continuum

First, we give a more detailed description on the use of the three-step model. Within the single-atom picture, the electron acceleration in the continuum is treated classically. After it is ionized at a time t_i, its motion until recombination at a time t_r is given by Newton's equation,

$$\ddot{x}(t) = -\frac{e}{m_e} E(t), \tag{3.5}$$

where x is the distance to the nucleus and e the electron charge. Solving this equation yields electron trajectories, as illustrated in Fig. 3.6a for a single half-cycle of the driving field. The kinetic energy of the electron when it recombines with the nucleus is indicated by the color scale and the gray curves correspond to trajectories for which the electron does not recombine with the ion. We see that a broadband continuum of frequencies is emitted, with a maximum energy given by the cut-off law [see Eq. (3.2)].

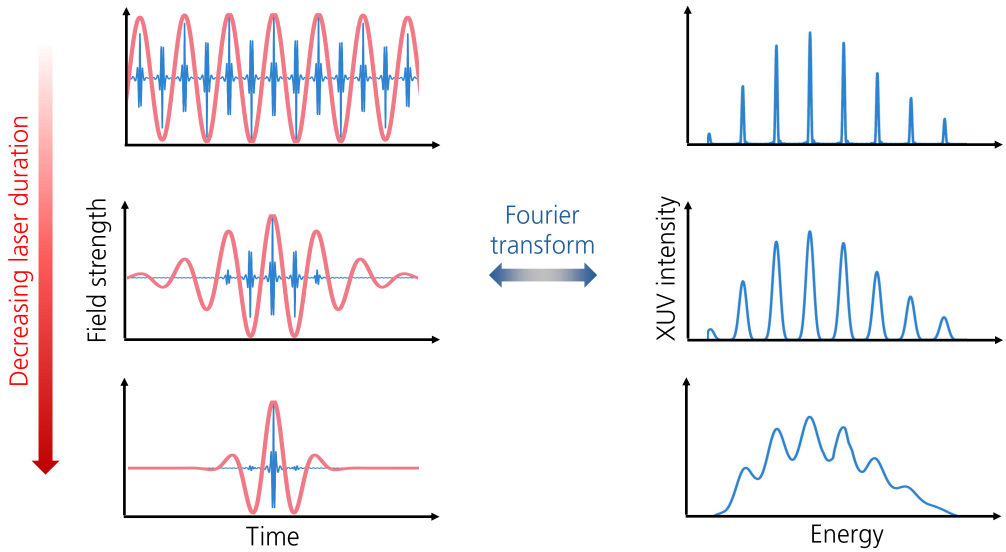

Figure 3.5: Temporal and spectral profiles of the harmonic emission for decreasing laser durations. Left panel: Electric field of the attosecond pulses (blue) generated by driving lasers (red) of different durations. Right panel: Corresponding HHG spectra.

Figure 3.6b shows the kinetic energy as a function of the ionization time (left) and recombination time (right). For a certain kinetic energy, two different trajectories contribute. These can be classified into two families: the "short" trajectories, that correspond to electrons that recombine between 0 and $0.45T_0$, and the "long" trajectories, that correspond to electrons recombining between $T_0/2$ and $3T_0/4$. In the former, lower photon energies are emitted first while it is the opposite in the latter. This energy-dependent delay in the emission is called attosecond chirp (attochirp) [65].

For real laser pulses that have a finite duration, the intensity varies from one half-cycle to the next, with more pronounced differences for few-cycle drivers. Electrons in the continuum therefore acquire a trajectory-dependent phase, called dipole phase, which is different for electrons emitted in different half-cycles. A simple approximation is derived in [66] by assuming that the XUV photon frequency varies linearly with the return time for plateau harmonics (see dashed line in Fig. 3.6b):

$$\Phi(\Omega) \approx t_p(\Omega - \Omega_p) + \frac{\gamma}{I(t)}(\Omega - \Omega_p)^2, \tag{3.6}$$

where

$$\gamma = (t_c - t_p)\frac{\hbar\epsilon_0 m_e c}{3.2e^2}\omega_0^2, \tag{3.7}$$

Ω is the XUV photon frequency, Ω_p the ionization frequency emitted at t_p and Ω_c the cut-off frequency emitted at t_c. This equation is valid for the short trajectory. The second term is the GDD, which is inversely proportional to the fundamental laser intensity and which leads to a chirp of the attosecond pulses (attochirp). Since the intensity varies over femtosecond time scales, it gives rise to a femtosecond chirp (femtochirp) [65]. This femtochirp breaks the $\pi/2$ periodicity by shifting an attosecond pulse temporally, analogous to changing the separation between two pulses

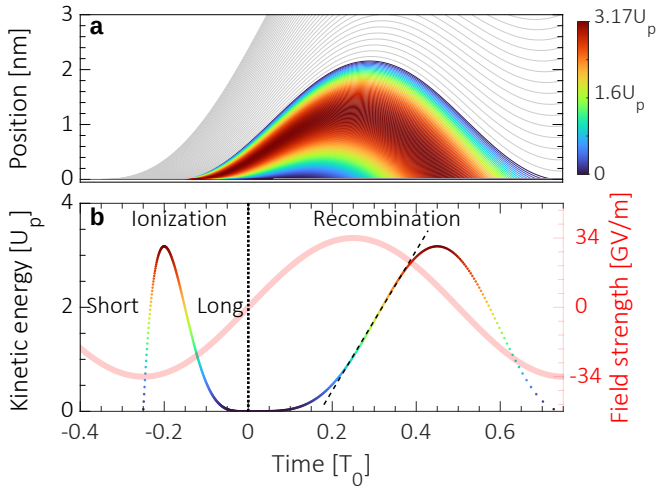

Figure 3.6: Electron trajectories in the continuum. (a) Distance from the nucleus of the electron as a function of time. The kinetic energy at recombination is indicated in color scale for each trajectory. (b) Electron kinetic energy as a function of the ionization (left) and recombination (right) time.

in multiple-pulse interference (see previous chapter). In the spectral domain, this translates to a shift of the harmonic peak energies.

In this thesis, HHG is driven by 6 fs laser pulses. The XUV photon energies emitted in each half-cycle of such a pulse can be calculated by solving Eq. (3.5), which yields the kinetic energy at return, and then applying the cut-off law [see Eq. (3.2)]. The resulting photon energy is shown in Fig. 3.7 as a function of the recombination time for a CEP of (a) 0° and (b) 90°. In both cases, the cut-off energy varies across the pulse, since the value of U_p depends on the peak intensity of the half-cycle in which the electron recombines. In particular, higher photon energies are only emitted during a few half-cycles of the electric field, at the center of the pulse. This can be understood with the cut-off law [Eq. (3.2)], from which the minimum field intensity $I_{\min}(q)$ required for a harmonic order q to reach the plateau region can be deduced:

$$I_{\min}(q) = \frac{m_e\omega^2}{3.17\alpha b}(q\hbar\omega - I_p). \tag{3.8}$$

It varies linearly in the harmonic order q. This behavior is specific to few-cycle drivers as it is a fair assumption to assume that consecutive half-cycles have similar intensities for long drivers.

Finally, a given harmonic order is emitted in a different number of half-cycles between the two CEP values. For example, energies above 38 eV are generated in three half-cycles of the pulse in Fig. 3.7a, against in two half-cycles in Fig. 3.7b. The reason is that the CEP governs the intensity of the half-cycles. A CEP of 0° presents a main half-cycle symmetrically surrounded by two half-cycles of slightly smaller amplitudes while a CEP of 90° presents two main half-cycles symmetrically surrounded by two half-cycles of comparatively small amplitudes. This CEP-dependent property has major consequences on the spectro-temporal properties of the harmonic emission, which is described in the following as it is central to the work of **Paper II**.

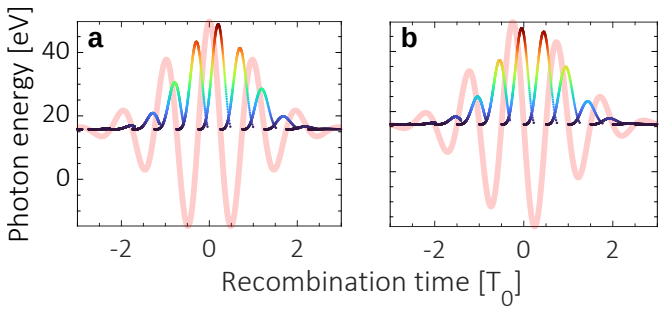

Figure 3.7: Photon energies for a few-cycle pulse. Electron kinetic energy as a function of the recombination time for HHG driven by a 6 fs pulse with a CEP of (a) 0° and (b) 90°. The field of the driving laser is indicated in red.

3.2 The role of the CEP

Figure 3.8 shows APTs simulated by a 6 fs laser pulse -similar to those delivered by the OPCPA laser system- for a CEP of 0°, 45° and 90°. At 0°, three main attosecond pulses are produced, consisting of a main one symmetrically surrounded by two less prominent ones. Shifting the CEP by 45° breaks the symmetry relative to the center of the pulse, leading to three attosecond pulses with different amplitudes, including a very small one. Finally, an additional step of 45° restores the symmetry, and two pairs of attosecond pulses are emitted, with two dominating ones. The total number of attosecond pulses is very important in experiments. For example, it leads to very different features in laser-assisted photoionization experiments, as explained in **Paper II** and in [56].

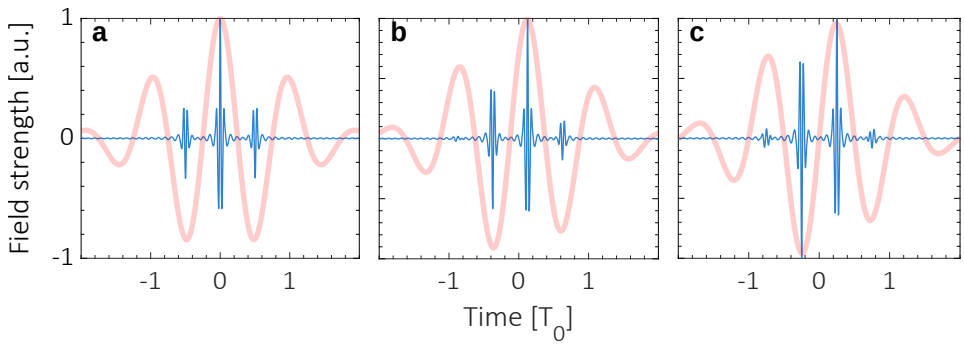

Figure 3.8: CEP-dependence of short pulse trains in the temporal domain. APTs produced by a field with a CEP of (a) 0°, (b) 45° and (c) 90°. The driving field is shown in red.

Although the temporal profile of the APTs provides information about the number of pulses, it was found in the previous section that different energies are emitted in a different number of half-cycles (see Fig. 3.7). This predicts a decreasing number of attosecond pulses with increasing energy. In Fig. 3.9, the XUV spectrum generated by a few-cycle pulse having 45° CEP is sketched. Each half-cycle of the laser field leads to attosecond pulses with different energy cut-offs E_{ci}. In the spectrum, three spectral regions are distinguished, that result from the interference of a different number of attosecond pulses in time. The lowest harmonic orders (up to E_{c1}, in orange) consist

of odd harmonic peaks separated by $2\omega_0$, with smaller even harmonics in-between, due to the interference between three attosecond pulses. At energies above E_{c1}, the harmonic structure consists of broad odd harmonics, due to the interference between two attosecond pulses (in blue and purple). Finally, a single half-cycle (in blue) produces photon energies beyond E_{c2}, leading to a continuum spectrum (single pulse). This slit-interference behavior of HHG in the few-cycle regime has many consequences for photoionization experiments, discussed in **Paper II**.

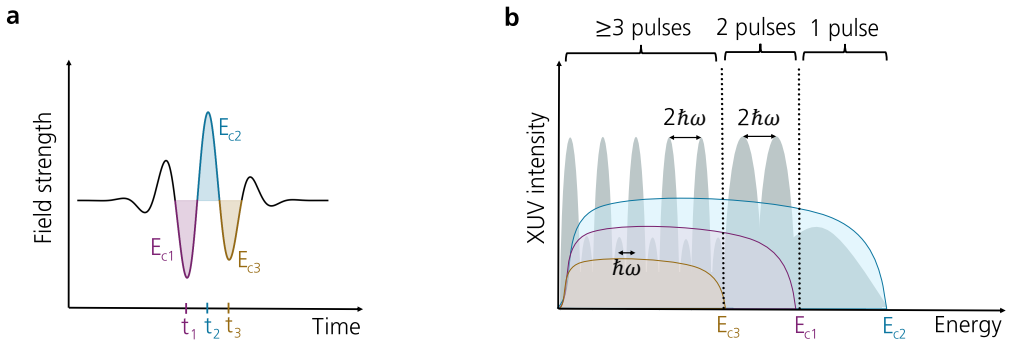

Figure 3.9: Spectral structure of a short APT in the spectral domain. (b) Sketch of the spectral content of attosecond pulses generated in each half-cycle of a short laser pulse, shown in (a). Each color (purple, blue, and orange) refers to a specific pulse, with a unique cut-off energy E_c. The pattern resulting from the interference is shown in gray. Schematic adapted from **Paper II**.

It is worth mentioning that for certain CEP values, the emission of a continuum at high energies, compatible with the generation of a SAP if spectrally selected, is predicted. However, it is not isolated in the temporal domain. Furthermore, the relatively narrow spectral width restricts the temporal duration. Several techniques exist to further confine the harmonic emission. In **Paper I**, we drive HHG with polarization-gated pulses to confine the harmonic emission to a single half-cycle of the driving pulse. In **Paper II**, we show that macroscopic effects can confine the harmonic emission.

3.3 Impact of macroscopic effects on short APTs

As previously stated, optimizing the yield of HHG relies on a trade-off between many parameters, which leads to an immense versatility in HHG light source design. Previous works established that the optimum yield follows an hyperbolic relationship between the gas pressure and gas medium length [64, 67], with each of the two hyperbola branches being dominated by certain phase mismatch terms. In the vertical branch, the total phase mismatch mostly depends on the neutral and plasma dispersion ($\Delta\mathbf{k} \approx \Delta\mathbf{k}_{\mathrm{at}} + \Delta\mathbf{k}_{\mathrm{fe}}$). In contrast, the plasma dispersion is negligible in the horizontal branch ($\Delta\mathbf{k} \approx \Delta\mathbf{k}_{\mathrm{at}} + \Delta\mathbf{k}_{\mathrm{foc}} + \Delta\mathbf{k}_{\mathrm{dip}}$). In this thesis, the experimental parameters place the HHG light source close to the crossover of both branches, where all terms can play a role. This is depicted in Fig. 3.10, where the intensity of the harmonic order 25 calculated by solving the time-dependent Schrödinger and propagation equations is plotted in color as a function of the pressure and of the gas length for our experimental parameters [63]. Below, we explain how the harmonic intensity is calculated with a simple one-dimensional model [63]. Based on this, a simple

approach to calculate the APTs, that accounts for the complete (micro- and macroscopic) HHG process, is described which was developed in the framework of **Paper II**.

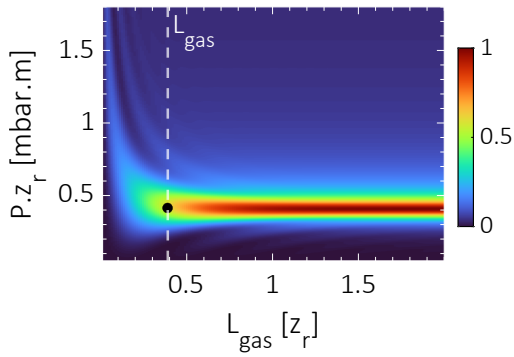

Figure 3.10: **Experimental hyperbola of the Lund HHG light source.** Simulated intensity for harmonic 25 generated in argon (in color) as a function of gas length and pressure. The medium is placed after the focus (z=18 µm) and the ionization degree is calculated at an intensity of $\sim 1.6\times10^{14}$ W/cm^2. The Rayleigh length is z_r=100 µm. The white dashed line indicates a medium length of 36 µm and the black dot the experimental set-up in Lund.

Transient phase matching

To calculate the harmonic yield, knowledge about the total phase mismatch [see Eq. (3.4)] is first required. Below, the different terms are given for our experimental parameters, assuming one-dimensional on-axis phase-matching along the longitudinal coordinate z. Their detailed description can be found in [64].

The phase of a Gaussian pulse changes under focusing, which is described by the Gouy phase $\varphi(z) = -\arctan(z/z_R)$, where z_R is the Rayleigh length. This leads to a phase mismatch given by

$$\Delta k_{\mathrm{foc}}(z) = -q\frac{z_r}{z^2+z_r^2} < 0. \tag{3.9}$$

In Fig. 3.11a, Δk_{foc} is plotted for harmonic orders between 11 and 27, for z=18 µm and z_r=100 µm. As expected, it decreases linearly with the harmonic order.

The microscopic single-atom response also leads to a wave vector mismatch. This term can be calculated as the spatial derivative of the dipole phase [see Eq. (3.6)]. For short trajectories, it takes the following form

$$\Delta k_{\mathrm{dip}}(z,t) = \frac{2z}{z_r^2}\frac{\gamma(q\omega_0-\Omega_p)^2}{I^2(t)}. \tag{3.10}$$

The sign depends on the position, and is opposite before and after the focus (z=0), at which the term cancels out. Figure 3.11b shows the variations of Δk_{dip} with the harmonic order and time for a 6 fs pulse of $\sim 1.6\times10^{14}$ W/cm^2 intensity and z=18 µm. It varies rapidly in time, due to the intensity inverse scaling. In addition, it is larger for higher order harmonics.

Finally, dispersion arises from the interaction with the nonlinear medium, with neutral atomic density ρ, and depends on the fraction of free electron η_{fe} arising from ionization of the atoms.

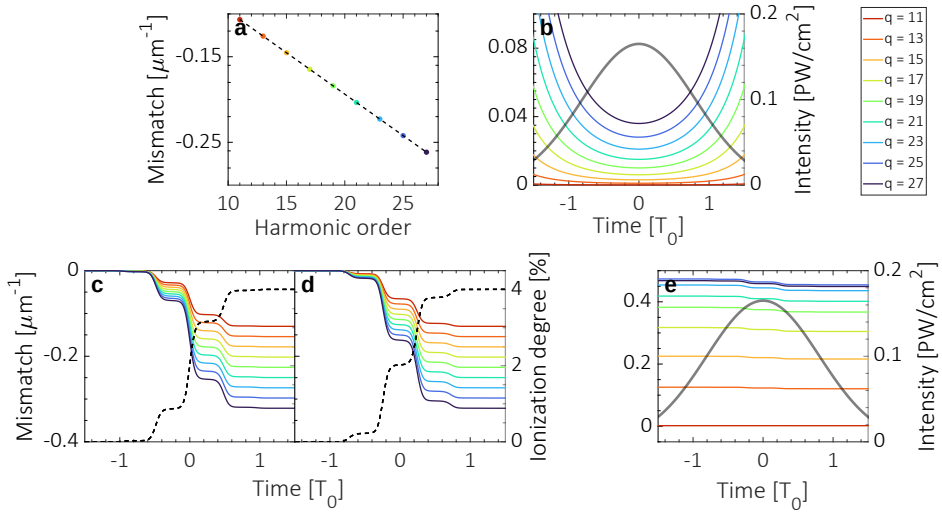

Figure 3.11: **Individual contributions to the total wave vector mismatch.** (a) Wave vector mismatch due to focusing as a function of the harmonic order. (b) Wave vector mismatch due to the dipole phase as a function of time for different harmonic orders (color). The intensity is shown in gray. (c,d) Temporal phase mismatch originating from the plasma dispersion for different harmonic orders (color) at a CEP of 0° and 90°. The ionization degree is shown in gray. (e) Temporal phase mismatch originating from argon atoms for different harmonic orders (color). The pulses are 6 fs long with a peak intensity of 1.6×10^{14} W/cm^2. The Rayleigh length is 100 µm. The pressure in the 36 µm-long medium is 5.5 bar.

The fraction of free electron is often computed with approximations that rely on a cycle-average of the free electron density variations, such as the Perelomov-Popov-Terent'ev (PPT) model [68]. In this thesis, the non-adiabatic Yudin-Ivanov model, described in [69], is used which accounts for subcycle variations of the ionization degree. Figure 3.11c,d shows the temporal variations of the ionization degree for a 6 fs pulse of peak intensity equal to 1.6×10^{14} W/cm^2 and CEP of 0° and 90°. Several plateaus occur at times when the electric field is zero, meaning no additional free electrons are created. The times at which plateaus occur depend on the CEP.

The electronic wave vector mismatch is calculated as the optical path length difference between the fundamental and harmonic fields. This leads to

$$\Delta k_{\mathrm{fe}}(t) \approx -q\frac{\rho\eta_{\mathrm{fe}}(t)}{\omega_0}\frac{e^2}{2c\epsilon_0 m_e} < 0. \tag{3.11}$$

It is proportional to the atomic density and harmonic order q. In Fig. 3.11c and d, the temporal variations of Δk_{fe} are plotted for the harmonic orders 11-27 and a CEP of 0° and 90°. The pressure is 5.5 bar. As expected, Δk_{fe} varies linearly with the harmonic order. For a given harmonic order, the same value of Δk_{fe} is reached at different times for the two CEPs.

The atomic wave vector mismatch Δk_{at} is expressed as

$$\Delta k_{\mathrm{at}}(t) \approx q\rho\Delta\alpha(q)\frac{\omega_0}{2c\epsilon_0}\left[1-\eta_{\mathrm{fe}}(t)\right] > 0, \tag{3.12}$$

where $\Delta\alpha(q) = (\alpha_0 - \alpha_q)$ with α_0 and α_q being the static and dynamic polarizabilities. In Fig. 3.11e, Δk_{at} is plotted as a function of time for the same spectral range and parameters as in the previous

figures. The value of Δk_{at} is positive, and varies with the harmonic order. The temporal variations can be neglected for the experimental conditions of this work, due to the small ionization degree. It is important to note that the atomic contribution is positive and can be controlled with the density of atomic gas to achieve perfect phase matching [see Eq. (3.3)].

Finally, the total phase mismatch calculated with Eq. (3.4) is shown in Fig. 3.12a,b for the same parameters as the above figures. The temporal evolution depends on the order. For instance, the harmonic 15 reaches perfect phase matching at the peak of the intensity against in the falling edge of the pulse ($t > 0$) for the other orders. At 90°, it occurs close to an ionization plateau. Due to the temporal variations of the ionization degree, the phase-matching window ($|\Delta k(q,t)| \approx 0$) is transient. Perfect phase matching occurs for a given critical ionization degree $\eta_{\mathrm{crit.}}$, determined by all phase matching terms. In particular, a larger neutral atomic density needs to be compensated by a higher ionization degree. In our experimental conditions, the ionization degree is small, typically a few percent explaining it can be reached in the falling edge of the pulse. We show in the following that it leads to a temporal confinement of the harmonic emission for the higher orders.

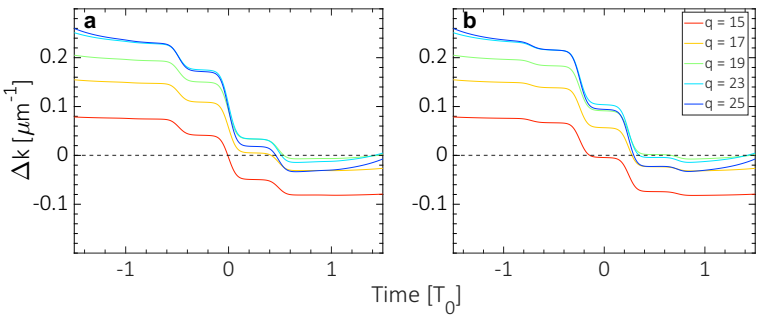

Figure 3.12: **Temporal variations of the total phase mismatch.** Total phase mismatch as a function of time for four different harmonic orders q and a CEP of (a) 0° and (b) 90°. The horizontal black dashed line corresponds to perfect phase matching.

Macroscopic confinement of the harmonic emission

In a one-dimensional model, considering the absorption of the harmonics under propagation in the gas, the harmonic intensity can be expressed as [63]:

$$I_q(t) \propto \overbrace{|d_q(t)|^2}^{\text{microscopic}} \underbrace{\rho \frac{\cosh\left[\kappa_q L_{\mathrm{gas}}\right] - \cos[\Delta k(t) L_{\mathrm{gas}}]}{\kappa_q^2 + \Delta k^2(t)} e^{-\kappa_q L_{\mathrm{gas}}}}_{\text{macroscopic}}, \tag{3.13}$$

where $L_{\mathrm{abs}} = 1/(2\kappa_q)$ is the finite absorption length with $\kappa_q = 1/(\rho\sigma)$ being the absorption coefficient and σ the absorption cross-section [70]. Figure 3.13a,b shows the harmonic yield associated to the total phase mismatches in Figure 3.12a,b. The high-order harmonics (harmonics 23-25) are confined in the falling edge of the pulse. For both CEPs, the harmonics are generated mainly after the maximum intensity of the driving pulse. At 90°, good yields (superior to half the

maximum) are achieved for a shorter temporal window, making the phase matching more transient. The single-atom alone, indicated by the black dashed line would predict that higher orders are produced uniformly over the course of the pulse.

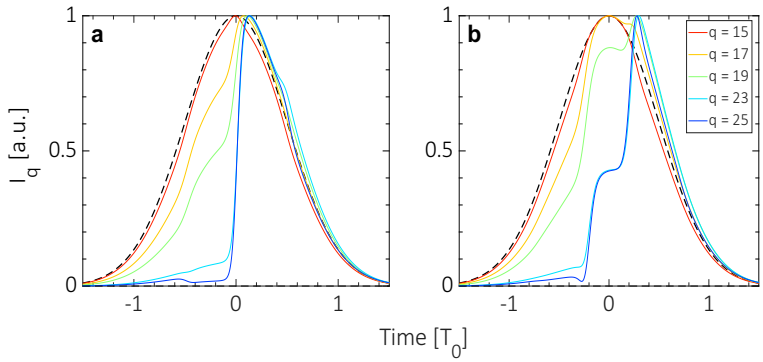

Figure 3.13: **Temporal variations of the harmonic yield.** Harmonic yield as a function of time for four different harmonic orders q and a CEP of (a) 0° and (b) 90°. Dashed lines indicate the temporal profile of the single-atom response.

This has consequences for the short APTs produced in this work which can be simulated using Eq. (3.13) as the sum of the harmonic fields [37, 65]:

$$E_{\mathrm{APT}}(t) = \sum_q E_q(t) = \sum_q \sqrt{I_q(t)} e^{-iq\omega_0 t + i\Phi_{\mathrm{dip}}(t)}, \tag{3.14}$$

where Φ_{dip} is the temporal dipole phase. Figure 3.14 shows the Wigner distribution of APTs simulated with the one-dimensional model for the parameters used throughout this section. The physical signal components correspond to the positive regions separated by half an optical period, while the in-between regions with alternating positive and negative signals corresponds to cross-terms inherent to the Wigner distribution (see previous chapter). In the top panel, Eq. (3.13) is used such that both micro- and macroscopic effects are considered while in the bottom panel, only the microscopic response, $I_q(t) \propto |d_q(t)|^2$ is included. The two cases exhibit pronounced differences. In particular, the relative strengths between the attosecond pulses is different with and without phase matching. In general, the number of dominating attosecond pulses is smaller when phase matching is included due to confinement of the harmonic emission.

In Fig. 3.14a and c, the driving laser CEP is equal to 0°. When phase matching is included, mainly two attosecond pulses arise at high energies while three equally strong attosecond pulses are visible when it is not included. For a CEP of 90° (Fig. 3.14b and d), one attosecond pulse in a half-cycle in the falling edge of the pulse dominates when there is the phase matching while there are mainly four attosecond pulses with the single-atom response only. This shows that phase matching reshapes the relative amplitudes between the attosecond pulses in the train, which in turn affects the spectral pattern resulting from multiple-pulse interference.

This model brings many physical insights into the phase matching dynamics. However, it cannot describe the complex three-dimensional spatio-temporal effects of the generation process, which can lead to a non-uniform dipole response. A more advanced model, that includes reshaping of the electric field (plasma and neutral dispersion) during propagation in the nonlinear medium, is also used in **Paper II** [71].

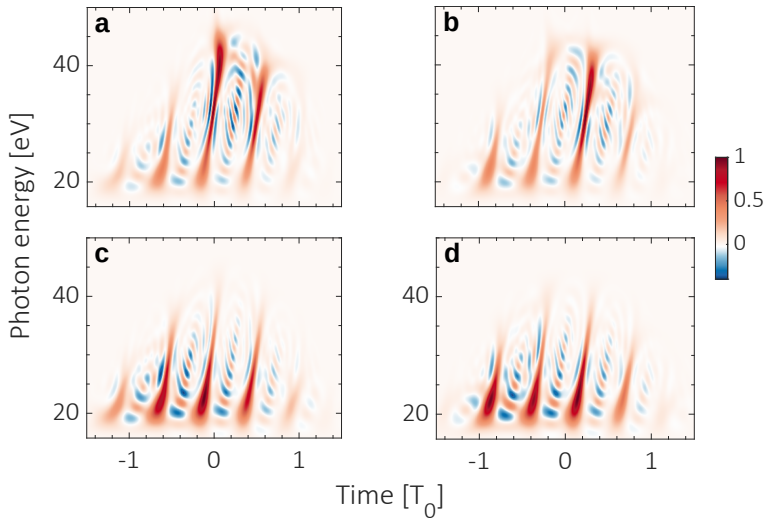

Figure 3.14: **Wigner distribution of the short APTs from the OPCPA.** APTs generated with the one-dimensional model using 6 fs pulses with a peak intensity of 1.6×10^{14} W/cm^2 and a CEP of 0° (left panel) and 90° (right panel). The top row corresponds to simulations including the macroscopic HHG effects while the bottom row shows the APTs simulated with the single-atom response only. The parameters are the same as in all of the figures in this section.

4 Experimental evidence of harmonic confinement

This section presents the main experimental evidence of harmonic confinement in relation to **Paper I and II**.

4.1 Harmonic-generation set-up

The attosecond light source in Lund is schematically illustrated in Fig. 3.15. The pulses from the OPCPA laser system (described in Chapter 2) enter a vacuum chamber kept at a static pressure of 10^{-6} mbar. At the entrance, a thin beamsplitter (BS) transmits 90% of the beam while the remaining 10% (not shown) is reflected and used for applications such as laser-assisted photoionization. Then, the transmitted pulses are tightly focused to a beam spot size of 5 µm by an off-axis parabola (OAP) with a focal length of 5 cm. The focus of the beam is located in the middle of another small vacuum chamber where a 30–40 µm long gas jet is inserted. The interaction of the laser with the gas generates a comb of broad high-order harmonics. High conversion efficiencies in this tight focusing geometry require large atomic densities (up to several kg/m^3) which may negatively affect the vacuum in the chamber [72]. To overcome this issue, a catcher is connected to the nozzle which is continuously pumped. A three-dimensional translation stage is finally used to further optimize the harmonic generation conditions. For all experiments, the gas jet is placed after the focus, to select harmonics corresponding to the short trajectories [73].

At the exit of the HHG chamber, an aluminium filter (F) blocks the remaining fundamental IR while transmitting the XUV through a hole-drilled mirror (HM). A retractable flat mirror (FM)

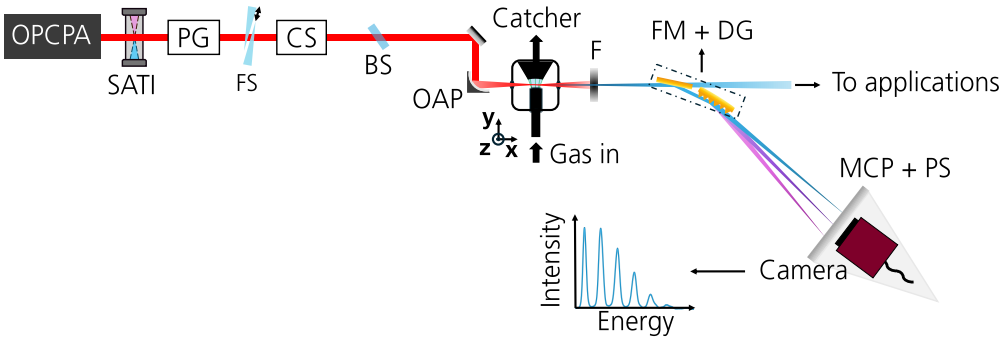

Figure 3.15: Schematic of the attosecond light source in Lund. Laser pulses from the OPCPA can be stabilized using the SATI. A large portion of these pulses is transmitted by a beamsplitter (BS) into a pump arm, and focused by an off-axis parabola (OAP) to perform HHG. The residual fundamental laser is removed with an aluminum filter (F). The generated XUV is guided by a flat mirror (FM) and a diffraction grating (DG) to a microchannel plate (MCP) coupled to a phosphorescent screen (PS). Optionally, a polarization gate (PG) can be implemented and then sent to a pre-compensation set-up (CS). A fused silica (FS) wedge pair is used to control the overall dispersion.

and diffraction grating (DG) spatially separates the output XUV frequencies onto a micro channel plate (MCP) and phosphor screen (PS) assembly in the far-field. A camera images the phosphor screen. A limited spectral range of the harmonic comb is recorded and can be tuned by changing the grating angle. By retracting the flat mirror and the grating, the XUV can be sent to application chambers.

High-order harmonic generation is a nonlinear process which requires high peak intensities. This means that the laser pulse must be the shortest possible in the HHG medium. Experimentally, this is achieved by controlling the dispersion with the fused silica (FS) wedge pair (see Fig. 3.15). More precisely, a harmonic dispersion scan is recorded, which consists in acquiring XUV spectra for different insertions Δx_{SiO_2} of the wedge pair. An example for HHG performed in argon with CEP-stabilized pulses is shown in Fig. 3.16. At the optimum compression point (see white dashed line), the XUV signal and the cut-off energy are maximum, since the peak intensity is largest. This is the wedge position one must choose to have the shortest, most intense pulse in the HHG medium.

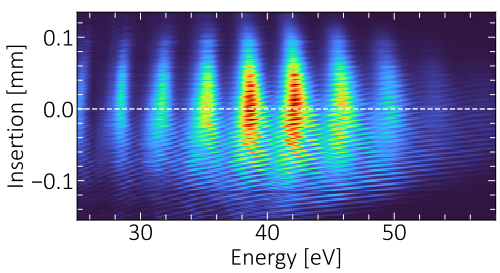

Figure 3.16: Harmonic dispersion scan in argon. Spatially integrated XUV spectrum as a function of the FS wedge pair insertion. The CEP is locked with the SATI.

Moreover, closely spaced tilted fringes can be observed. If the scan is performed without CEP locking, they are not visible. They should therefore be connected to CEP-effects. In fact, it was

shown in a previous work [66] that for small changes of Δx_{SiO_2} around the optimum compression point, the fringes exactly follow the CEP shifts induced by the wedges. This is because the dispersion introduced for very small changes (on the order of the micrometer) is negligible. The harmonic dispersion scan can therefore be used to study the effect of the CEP on XUV spectra, which is done in **Paper I** to investigate the CEP-dependent generation of a XUV continuum.

4.2 Passive macroscopic confinement

Experimental far-field HHG spectra are shown in Fig. 3.17 for two CEP values separated by 90° and different backing pressures (around twice the pressure in the gas medium) [72]. At low pressure (5 bar), the spectral widths of all harmonic orders are similar, suggesting that the number of attosecond pulses remains constant with energy. When the pressure is increased to 9 bar, however, higher-order harmonics broaden. This implies that these harmonics are generated over a shorter time. Figure 3.17a shows broad peaks compatible with generation of two attosecond pulses while Fig. 3.17b shows peaks in-between the odd orders, which suggests the presence of three attosecond pulses. This confirms that macroscopic effects can change the number of attosecond pulses in selective spectral regions, hence the spectro-temporal properties of the APTs.

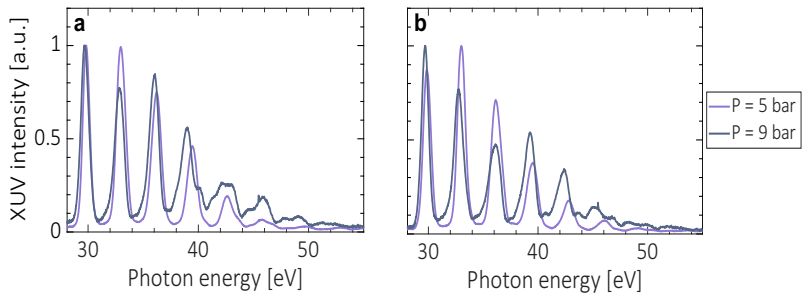

Figure 3.17: **Effect of atomic density on XUV spectra.** Far field XUV signal integrated radially as a function of the energy for two CEPs separated by 90°. The different colors indicate different backing pressures. The curves are normalized to their maximum.

4.3 Temporal confinement based on polarization gating

Alternative techniques to confining the harmonic emission involve manipulating the electron trajectories in the continuum through a driving field with tailored polarization. One widely used method is to drive HHG with a polarization gate, as elliptical fields are known to strongly reduce the efficiency of HHG [74]. For instance, the XUV yield has been observed to decrease by half at a threshold ellipticity $\varepsilon_{\mathrm{th}}$ of 13% [75]. This reduction can be understood within the three-step model. After ionization in the continuum, an electron accelerates along the electric field. For an elliptical field, a transverse component is always present, which continuously drives the electron away from its parent ion, thereby preventing it from recombining. Without recombination, photon emission cannot occur. Therefore, the complete HHG process only arises for (nearly) linear polarization. Driving HHG with polarization-gated pulses, where the polarization is linear in a narrow temporal

region, thus confines temporally the XUV emission. Many studies showed that polarization gating can reduce the duration of APTs and even produce SAPs [76, 34, 77].

In **Paper I**, an XUV continuum spanning over 10 eV is generated by driving HHG with the polarization-gate set-up described in Chapter 2.3. Figure 3.18a shows a harmonic dispersion scan acquired by finely tuning the insertion Δx_{SiO_2} of the wedge pair.

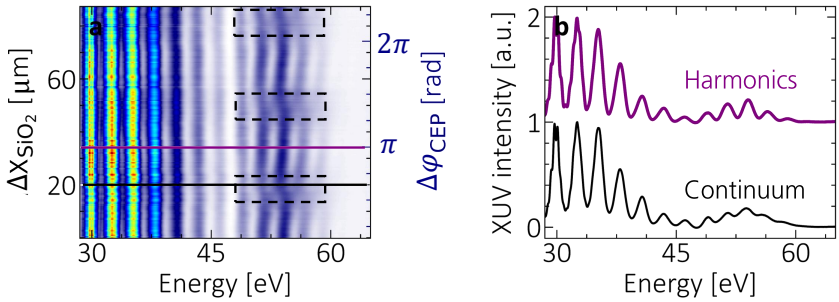

Figure 3.18: **CEP-dependent confinement of the XUV emission.** (a) Harmonic dispersion scan for HHG driven by polarization-gated few-cycle pulses. The dashed rectangles indicate the regions with XUV continua. (b) XUV spectra at two different CEPs, indicated by purple and black solid lines in (a). Figure adapted from **Paper I**

It can be seen that the harmonic spectrum changes with insertion at energies above 50 eV. The changes are visible for the high energies, since these correspond to electrons spending a longer time in the continuum, that are more sensitive to variations in ellipticity and to CEP-dependent energy cut-offs. In particular, continua appear in the regions indicated by black dashed rectangles. As seen before, $\Delta x_{SiO_2} \propto \Delta\varphi_{CEP}$, such that their periodicity is equal to π. These CEP values are those for which the emission of an attosecond pulse is confined to a single half-cycle near the peak of the electric field. The continuum can be better seen in Fig. 3.18b (black curve), where the harmonic spectrum for the insertion value indicated by the black line is plotted. At another CEP, for example indicated by the purple line, a harmonic structure is clearly visible (see purple curve in top plot) due to the gate spanning two optical half-cycles of the laser.

Finally, another approach to generating a SAP is to push the laser duration below the optical cycle [78, 33, 79, 80]. In practice, this requires complex laser systems composed of expensive and high maintenance equipment, whereas polarization gating relies on comparatively simple and cheaper experimental arrangements.

CHAPTER 4

Laser-assisted photoionization with ultrashort pulses

Studies of photoionization dynamics have attracted considerable interest with the development of synchrotron light sources [81]. An important aspect of these studies is the characterization of partial amplitudes and relative phases between different ionization channels as a function of the photon energy. However, measurements based only on the kinetic energy and angular distribution of the photoelectron are not sufficient, since the phase of the outgoing photoelectron is necessary to fully understand the dynamics [82]. In attosecond science, this phase can be accessed using laser-assisted photoionization. The principle, illustrated in Fig. 4.1a, consists in measuring the kinetic energy of electrons ionized by an XUV pulse in the presence of an IR laser field as a function of the delay between the two fields.

There exists two main approaches, which were initially introduced at the beginning of the millennium to characterize the XUV radiation: streaking [34, 33, 35] and RABBIT [36, 37]. In streaking, illustrated in Fig. 4.1b, the energy of an electron wavepacket produced by a SAP is changed by the presence of a strong IR field. This leads to a shift of the photoelectron energy spectrum (in blue) to lower (in gray) or higher (in red) energies. As a result, oscillations of the energy with the delay arise which encode information about the attosecond electron dynamics. In RABBIT, ionization by an APT is followed by the absorption or emission of a probe photon, as illustrated in Fig. 4.1c. Since the harmonic separation is twice the IR energy, photoelectrons produced by absorption of the harmonic q and of an IR photon reach the same final state as those due to the absorption of the harmonic $q+2$ and emission of an IR photon. This leads to sidebands (in red) in-between the main bands (in blue). Spectral interference arises between the absorption and emission paths, from which the attosecond electron dynamics is retrieved.

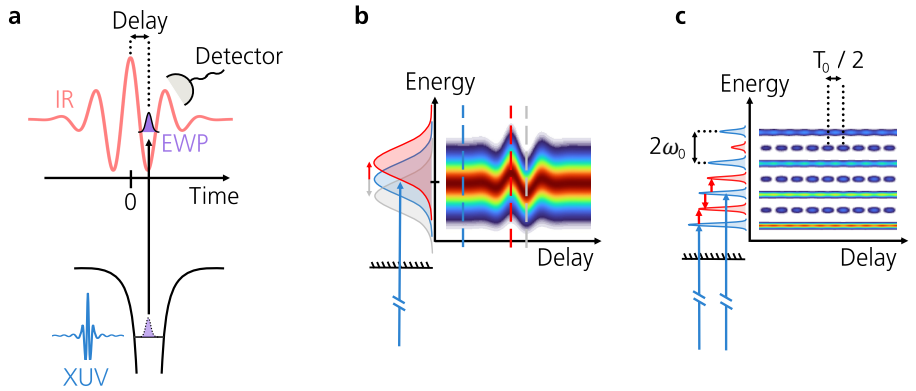

Figure 4.1: Schematic of LAP with SAPs and APTs. (a) Principle of a LAP measurement. An EWP is produced through photoionization by an attosecond pulse and interacts with an IR field. A detector measures a property of the electron. (b,c) Photoelectron counts as a function of the XUV-IR delay and kinetic energy in the case of (b) streaking and (c) RABBIT.

However, interpreting LAP measurements remains a complex task, due to their dependence on both the light fields properties and ionization processes. This may require prior knowledge of the fields or some simplifications of the process itself [38]. This complexity increases when ultrashort pulses are used, whose properties can significantly affect the measured signal, making the characterization of the fields particularly important [83, 84].

In this work, LAP measurements are performed using small sequences of attosecond pulses in the presence of a weak few-cycle laser field. In the first section, we provide the theoretical knowledge required to describe the photoionization processes involved in LAP, with an emphasis on the angular properties. Then, the experimental method, including tools to measure the photoelectron angular distribution, is detailed. Finally, three experiments are presented based on **Papers II, III and VI**, each of which can be interpreted as an interference phenomenon in either the time or the frequency domain.

1 Theoretical framework

1.1 Single-photon ionization

When an atom interacts with light in the XUV range, direct photoionization can occur, corresponding to an electronic transition from an initial discrete state $|i\rangle$ to a final continuum state $|\mathbf{p}\rangle$, as illustrated in Fig. 4.2. For XUV wavelengths, the field can be assumed uniform across the atom (dipole approximation), such that its interaction with the light can be expressed as

$$\hat{V}(t) = -\hat{\mathbf{d}} \cdot \boldsymbol{\mathcal{E}}_{\mathbf{XUV}}(t) \tag{4.1}$$

where $\mathcal{E}_{\mathrm{XUV}}$ is the XUV field and $\hat{\mathbf{d}} = -e\hat{\mathbf{r}}$ is the dipole operator. This can then be used to express the one-photon ionization transition amplitude within time-dependent perturbation theory

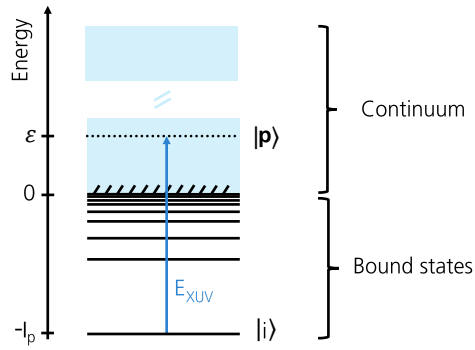

Figure 4.2: Direct photoionization of an atom following absorption of an XUV photon. Energy diagram showing the stationary states of an atom. The blue arrow indicates the transition in which an electron in the ground state $|i\rangle$ is promoted to a continuum state $|\mathbf{p}\rangle$.

(TDPT) as

$$\mathcal{A}^{(1)} = \underbrace{\frac{i}{\hbar}\langle \mathbf{p}|\,\hat{\mathbf{d}}\,|i\rangle}_{\mathcal{M}^{(1)}} \cdot \underbrace{\int e^{i\omega_{\mathbf{p}i}t}\,\boldsymbol{\mathcal{E}}_{\mathbf{XUV}}(t)\,dt}_{\tilde{\boldsymbol{\mathcal{E}}}_{\mathbf{XUV}}(\omega_{\mathbf{p}i})}, \tag{4.2}$$

where $\omega_{\mathbf{p}i} = \omega_{\mathbf{p}} - \omega_i$ is the frequency difference between the initial (energy ω_i) and the final state (energy $\omega_{\mathbf{p}}$), $\mathcal{M}^{(1)}$ is the one-photon transition matrix element and $\tilde{\boldsymbol{\mathcal{E}}}_{\mathbf{XUV}}$ is the Fourier transform of the XUV field. This formula shows that measuring the photoelectron yield ($|\mathcal{A}^{(1)}|^2$) as a function of kinetic energy depends on the spectrum of the ionizing radiation, as well as on the square of the energy-dependent dipole matrix elements $\langle \mathbf{p}|\,\hat{\mathbf{d}}\,|i\rangle$. This yield also depends on the electron emission angle relative to the linear polarization of the XUV, which we define along $\mathbf{z}$ throughout this chapter. In this work, the angularly-resolved photoelectron yield is the experimental observable.

In atoms, the wavefunction of an electron in the initial state can be separated into a radial and an angular part $\Psi(\mathbf{r}) = R_{nL}(r)Y_{Lm_L}(\theta,\phi)$, characterized by a principal quantum number n, an orbital angular momentum L and a magnetic quantum number m_L, and where $\mathbf{r} = \{r,\theta,\phi\}$ are the spherical coordinates. As ionization is a half-scattering process, the final state in the continuum is given by a linear superposition of waves with well-defined angular momentum:

$$|\mathbf{p}\rangle = \frac{1}{\sqrt{k}}\sum_{\lambda,m_\lambda} i^{\lambda}e^{-i\eta_\lambda(k)}\,Y^*_{\lambda m_\lambda}(\mathbf{k}/k)R_{k\lambda}(r)Y_{\lambda m_\lambda}(\mathbf{r}/r) \tag{4.3}$$

where $\mathbf{k} = \mathbf{p}/\hbar$ is the wavevector, $\eta_\lambda(k)$ a scattering phase and λ and m_λ the orbital angular momentum and magnetic quantum number of the final state, respectively. This is called the partial wave expansion.

The angular part of the wavefunction is described by spherical harmonics

$$Y_{\lambda m_\lambda}(\theta,\phi) = \sqrt{\frac{2\lambda+1}{4\pi}\frac{(\lambda+m_\lambda)!}{(\lambda-m_\lambda)!}}P_\lambda^{m_\lambda}(\cos\theta)\,e^{im_\lambda\phi}, \tag{4.4}$$

where $P_\lambda^{m_\lambda}$ are the generalized Legendre polynomials. Their real part is plotted in Fig. 4.3 for $m_\lambda = 0$ and λ=0, 1, 2 and 3. The signal is symmetric with respect to the x–y plane. The sign, indicated in

color, changes between the downward ($z < 0$) and upward ($z > 0$) direction for odd λ but does not for even λ, since the parity of spherical harmonics is given by $(-1)^\lambda$. This parity dependence has many consequences for photoionization with ultrashort broadband pulses.

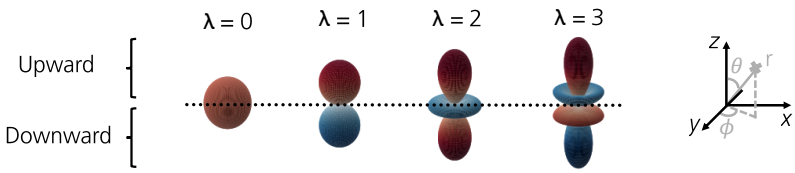

Figure 4.3: Angular properties of the spherical harmonics. Real part of the spherical harmonics for m_λ equal to 0 and λ to 0, 1, 2 and 3. The red (blue) color indicates positive (negative) values.

For linearly polarized light, the selection rules in the dipole approximation imply that the photoionization transition probability [see Eq. (4.2)] is non-zero when the change in orbital angular momentum Δl or in magnetic quantum number Δm fulfills:

$$\Delta l = L - \lambda = \pm 1 \quad \text{and} \quad \Delta m = m_L - m_\lambda = 0. \tag{4.5}$$

Therefore, absorption of a linearly polarized photon always changes the parity. Another major consequence is that several quantum pathways may lead to the same final state. The possible angular momentum channels for the single-photon ionization of ground state (a) helium and (b) neon are shown in Fig. 4.4. For helium, only the channel $L = 0 \rightarrow \lambda = 1$ is possible, and the final state is odd. For neon, the channels $L = 1 \rightarrow \lambda = 0$ or $L = 1 \rightarrow \lambda = 2$ exist, and the parity which is initially odd becomes even.

These selection rules therefore determine which angular momentum channels contribute to the partial wave expansion [see Eq. (4.3)]. Then, substituting Eq. (4.3) into Eq. (4.2) enables expressing the angular-resolved measured photoelectron yield, that is the photoelectron angular distribution (PAD), as

$$S^{(1)}_{\lambda L m_\lambda}(\theta,\phi) = \left|\mathcal{A}^{(1)}(\theta,\phi)\right|^2 = \Big|\sum_{\lambda,m_\lambda} a^{(1)}_{\lambda L m_\lambda} Y_{\lambda m_\lambda}(\theta,\phi)\Big|^2 \tag{4.6}$$

where

$$a^{(1)}_{\lambda L m_\lambda} = \tilde{\mathcal{E}}_{\mathrm{XUV}} M^{(1)}_{\lambda L m_\lambda} \tag{4.7}$$

with $M^{(1)}_{\lambda L m_\lambda}$ being the one-photon transition matrix element for the scattering channel λ.

In this thesis, photoionization of helium by a linearly polarized XUV field is considered. Since $m_L = m_\lambda = 0$, the magnetic quantum number notation is removed from now on and Eq. (4.6) simplifies to:

$$S^{(1)}_{10}(\theta) = |a^{(1)}_{10}|^2\, Y_{10}(\theta)^2 = \frac{3}{4\pi}|a^{(1)}_{10}|^2 \cos^2(\theta). \tag{4.8}$$

The PAD only depends on the polar angle θ, such that it exhibits azimuthal symmetry.

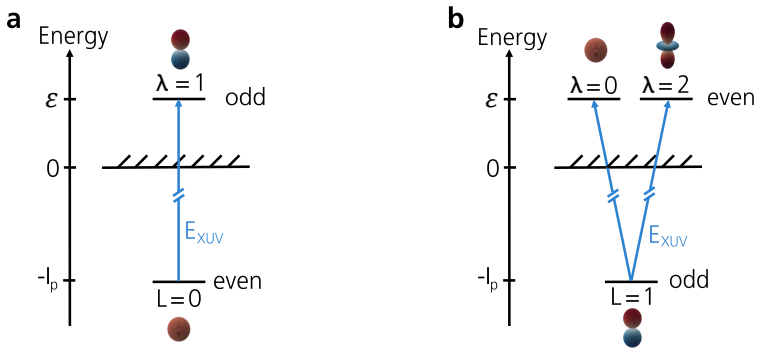

Figure 4.4: **Angular momentum channels in one-photon ionization.** Possible orbital angular momenta of the final states in XUV photoionization of ground state (a) helium and (b) neon for $m_L = 0$.

1.2 Two-photon ionization

In two-photon ionization involving XUV and IR fields, the interaction of the IR laser field with the atomic ground state can be neglected, meaning that the laser field primarily influences the electron in the continuum. Ionization therefore occurs through the absorption of an XUV photon and the additional absorption or emission of an IR photon. The corresponding two-photon transition amplitudes are expressed as

$$\begin{aligned} \mathcal{A}^{(2,+)} &= \tilde{\mathcal{E}}_{\mathrm{XUV}}(\Omega)\tilde{\mathcal{E}}_{\mathrm{IR}}(\omega)\mathcal{M}^{(2,+)}, \\ \mathcal{A}^{(2,-)} &= \tilde{\mathcal{E}}_{\mathrm{XUV}}(\Omega)\tilde{\mathcal{E}}^{*}_{\mathrm{IR}}(\omega)\mathcal{M}^{(2,-)}, \end{aligned} \tag{4.9}$$

where $\tilde{\mathcal{E}}_{\mathrm{IR}}$ is the Fourier transform of the IR field, Ω the XUV frequency and + (-) denotes the absorption (emission) of an IR probe photon. The two-photon transition matrix element is given by

$$\mathcal{M}^{(2,\pm)} = -\frac{i}{\hbar^2}\lim_{\eta\to 0^+}\sum_{\mathbf{p}'}\!\!\!\!\!\!\int \frac{\langle \mathbf{p}|\,\hat{d}\,|\mathbf{p}'\rangle\,\langle \mathbf{p}'|\,\hat{d}\,|i\rangle}{\omega_i + \Omega - \omega_{\mathbf{p}'} + i\eta}, \tag{4.10}$$

where $|\mathbf{p}'\rangle$ is an intermediate bound or continuum state with energy $\omega_{\mathbf{p}'}$. The two dipole matrix elements describe the transition from the initial to the possible intermediate states, and from the intermediate states to the final continuum state. The expression diverges when the light frequency matches the difference between two states ($\Omega = \omega_{\mathbf{p}'} - \omega_i$). Accordingly, any direct transition from a bound to a continuum state is resonant making photoionization by XUV light very efficient, in contrast to using an IR laser. Finally, the sum integral $\sum\!\!\!\!\!\!\int_{\mathbf{p}'}$ accounts for all possible quantum paths leading to the final state $|\mathbf{p}\rangle$.

In this thesis, broadband XUV and IR fields are employed, such that several combinations of XUV and IR frequencies can lead to the same final photoelectron energy. The coherent superposition of all these quantum paths must be taken into account. In **Paper III**, the effect of large bandwidths, and the associated manifold of possible quantum paths, is investigated in details.

1.3 Laser-assisted photoionization

In LAP measurements using a weak IR field, such as RABBIT, interference arises between two-photon quantum paths involving absorption of different harmonics. This is illustrated on the left of Fig. 4.5 for helium. Absorption of harmonics H_q and H_{q+2} (blue arrows) leads to main bands (blue Gaussian area). The additional absorption of an IR photon after absorption of harmonic H_q and emission of an IR photon after absorption of harmonic H_{q+2}, indicated by red arrows, forms sidebands (red Gaussian area) in-between the main bands. Parity is conserved since the same number of photons (two) is exchanged in both contributing pathways. The sideband signal is expressed as

$$S_{\mathrm{SB}} = \left| \mathcal{A}^{(2,+)}(\tau) + \mathcal{A}^{(2,-)}(\tau) \right|^2, \tag{4.11}$$

where τ is the XUV-IR delay. In general, the phase of a two-photon transition amplitude includes

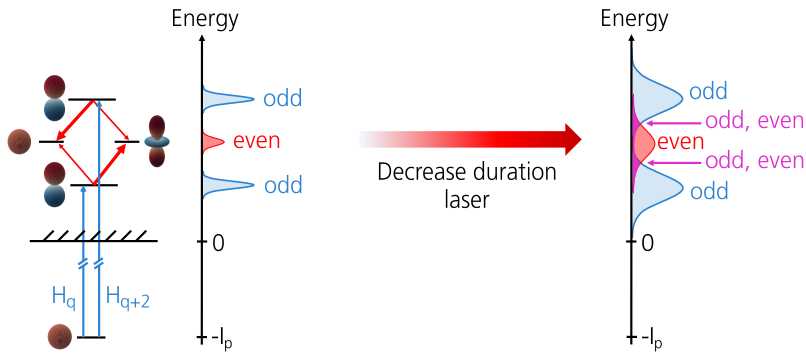

Figure 4.5: LAP scheme in the spectral domain. Left: Energy diagram illustrating LAP of ground state helium in the traditional RABBIT case (left). The blue (red) arrow represents transitions induced by the harmonics (probe field). The blue (red) Gaussian areas show the spectral region covered by the main bands (sideband). Right: same scheme for shorter driving and probe laser pulses. The increased spectral widths of the main bands and sideband lead to overlap regions, indicated in purple. The parity of the final states is indicated in text.

the phase of the $q(q+2)$-th harmonic field $\phi_q(\phi_{q+2})$, of the IR field $\varphi_{\mathrm{IR}} = \omega\tau + \varphi_{\mathrm{CEP}}$ and of the two-photon transition matrix element $\phi^{\pm}_{\mathrm{at.}}$ [85]. The sideband signal can then be shown to oscillate with delay at twice the IR frequency:

$$S_{\mathrm{SB}}(\tau) = |\mathcal{A}^{(2,+)}|^2 + |\mathcal{A}^{(2,-)}|^2 + 2|\mathcal{A}^{(2,+)}||\mathcal{A}^{(2,-)}| \cos\left[2\omega\tau - (\Delta\phi_{\mathrm{XUV}} + \Delta\phi_{\mathrm{at.}})\right] \tag{4.12}$$

where $\Delta\phi_{\mathrm{XUV}} = \phi_{q+2} - \phi_q$ and $\Delta\phi_{\mathrm{at.}} = \phi^{-}_{\mathrm{at.}} - \phi^{+}_{\mathrm{at.}}$. This shows that the sideband oscillations carry information about the light field properties and the ionization process.

In this work, however, few-cycle laser pulses are used to both drive HHG and as the probe field. Their short duration leads to broad harmonics and probe spectrum, thus enabling overlap between the main- and sidebands, as indicated in purple on the right of Fig. 4.5. This overlap allows one- and two-photon quantum paths of opposite parity to interfere. The measured signal can then be expressed as

$$S_{\mathrm{PM}}(\tau) = \Big| \underbrace{\mathcal{A}^{(1)}}_{\text{one-photon}} + \underbrace{\mathcal{A}^{(2,+)}(\tau) + \mathcal{A}^{(2,-)}(\tau)}_{\text{two-photon}} \Big|^2. \tag{4.13}$$

Several cross-terms arise, involving products between two-photon amplitudes, $\mathcal{A}^{(2,+)}\mathcal{A}^{(2,-)*}$, or between one- and two-photon transition amplitudes, $\mathcal{A}^{(1)*}\mathcal{A}^{(2,+)}$ or $\mathcal{A}^{(1)*}\mathcal{A}^{(2,-)}$. The former contribute to the RABBIT term oscillating at 2ω. The latter, however, give rise to new parity-mixing terms oscillating at ω, since only the two-photon transition amplitudes contain an IR phase dependence ($\mathcal{A}^{(2,\pm)} \propto e^{\pm i\omega\tau}$). These terms are discussed in **Paper III**.

For photoionization of helium with linearly polarized fields, the interference can involve three angular momentum channels, indicated in Fig. 4.5. Using the partial wave expansion [see Eq. (4.3)], the signal can then be expressed as a sum of contributions from each scattering channel

$$S_{\mathrm{PM}}(\tau,\theta) = \left| a_{10}^{(1)} Y_1(\theta) + \sum_{\ell} \left[a_{\ell 10}^{(2,+)}(\tau) + a_{\ell 10}^{(2,-)}(\tau) \right] Y_{\ell 0}(\theta) \right|^2, \tag{4.14}$$

where

$$\begin{aligned} a_{\ell 10}^{(2,+)}(\tau) &= \tilde{\mathcal{E}}_{\mathrm{XUV}}(\Omega)\tilde{\mathcal{E}}_{\mathrm{IR}}(\omega,\tau) M_{\ell 10}^{(2,+)}, \\ a_{\ell 10}^{(2,-)}(\tau) &= \tilde{\mathcal{E}}_{\mathrm{XUV}}(\Omega)\tilde{\mathcal{E}}_{\mathrm{IR}}^{*}(\omega,\tau) M_{\ell 10}^{(2,-)}, \end{aligned} \tag{4.15}$$

with $M_{\ell 10}^{(2,\pm)}$ being the two-photon transition matrix element for the scattering channel ℓ. The signal does not depend on the azimuthal angle ϕ since the magnetic quantum number is equal to zero.

Using $Y_{l0} \propto P_l^0$ [see Eq. (4.4)], the partial wave expansion naturally decomposes the PAD into a linear sum of associated Legendre polynomials, weighted by coefficients h_n [86]:

$$S_{\mathrm{PAD}}(\tau,\theta) = \sum_{n=0}^{2N} h_n(\tau) P_n^0[\cos(\theta)], \tag{4.16}$$

where N is the number of photons involved in the interaction. Interference involving quantum pathways of same parity produces a symmetric PAD relative to the *x*–*y* plane, perpendicular to the laser polarization (see Fig. 4.3). Detecting electrons emitted upwards or downwards is therefore equivalent. This means that odd Legendre polynomials, which are asymmetric relative to this plane, are not necessary to describe the PAD. However, those are used for describing the parity-mixing signal, which presents a pronounced asymmetry relative to the *x*–*y* plane.

1.4 Strong-field approximation

The photoionization transition amplitude in LAP can also be approximated using the strong-field approximation (SFA), which goes beyond lowest-order perturbation theory [87, 60]. It assumes that the electron is weakly affected by the Coulomb potential of the ion after photoionization by the XUV, leading to the following expression

$$b(\mathbf{p},\tau) = -i \int_{-\infty}^{+\infty} dt \underbrace{\boldsymbol{\mathcal{E}}_{\mathbf{XUV}}(t-\tau)\cdot\mathbf{d}\left[\mathbf{p}+e\mathbf{A}(\mathbf{t})\right]}_{\mathrm{I}} e^{\frac{i}{\hbar}\left(\frac{p^2}{2m_e}+I_p\right)t} \overbrace{e^{i\mathcal{S}(\mathbf{p},t)}}^{\mathrm{II}}. \tag{4.17}$$

Step I describes the photoionization to a continuum state by the XUV field at time $t - \tau$. In step II, the photoelectron accumulates a phase due to the IR vector potential $\mathbf{A}(\mathbf{t})$, equal to the action $\mathcal{S}(\mathbf{p}, t) = -\int_t^{+\infty} dt' \left[2e\mathbf{p}.\mathbf{A}(\mathbf{t}') + e^2\mathbf{A}^2(\mathbf{t}')\right]/(2m_e\hbar)$. Equation (4.17) can be solved numerically to simulate both streaking and RABBIT, which was done in Fig. 4.1b,c for photoelectrons having $p_z > 0$. For streaking, a Gaussian XUV with 20 eV bandwidth and a probe intensity of $1{\times}10^{13}$ W/cm^2 is used whereas in RABBIT, a long APT (harmonics of 0.2 eV bandwidth) and probe intensity of $2{\times}10^{11}$ W/cm^2 is used. The spectrograms exhibit different behaviors when varying the delay in the two regimes. In this work, the IR probe is weak and the APTs short, leading to an intermediate regime, as shown below.

Figure 4.6a,b shows simulated LAP spectra integrated over the upper hemisphere ($p_z > 0$) for APTs generated by a 6 fs driving field with CEP values of 0° and 90° and a weak IR probe (10^{11}W/cm^2). At long delays, the XUV and IR fields do not temporally overlap, and the spectra display main bands arising from the one-photon absorption of the harmonics. Near temporal overlap, the spectrograms obtained for the two CEP values differ significantly.

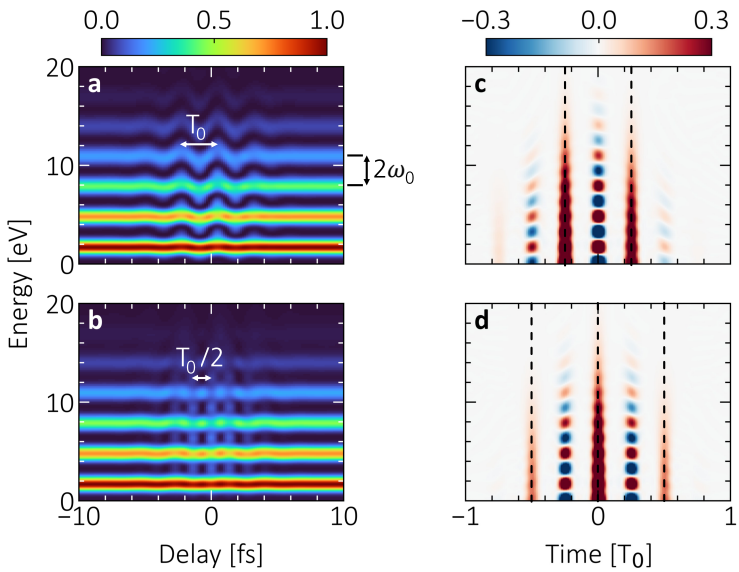

Figure 4.6: Simulated LAP spectrum for two and three attosecond pulses. Left panel: Photoelectron counts as a function of the XUV-IR delay and of the kinetic energy. A selection on electrons emitted in the upper hemisphere is performed. Right panel: Wigner distribution of the APTs (indicated by dashed lines) where the energy axis is shifted by the helium ionization potential. The laser that generates the APTs and dress the photoionization has a duration of 6 fs and a CEP of (a,c) 90° and (b,d) 0°.

For the CEP of 90°, see Fig. 4.6a, the electron kinetic energy oscillates as a function of delay with a periodicity equal to the laser period. This can be explained by first considering the Wigner distribution of the ionizing APT, calculated in Fig. 4.6c. The alternating positive and negative values correspond to the cross-correlation terms inherent to its mathematical definition (see Chapter 2). The positive regions appearing at $-0.25T_0$ and $0.25T_0$ (see dashed lines) indicate that the APT is predominantly composed by two attosecond pulses at all energies. The interference of the corresponding electron wavepackets leads to spectral interference in the LAP spectrogram, translating to energy peaks separated by $2\omega_0$. When the XUV and IR overlap, the IR phase modulates the

phase of each EWP, by a value which depends on the direction of emission (**p**), and on the vector potential (**A**). The phase difference is therefore opposite for the two wavepackets, due to their half-period separation (**A** has an opposite sign). As a result, the LAP spectral peaks associated with the two EWPs are shifted by equal magnitudes, but in opposite directions. This oscillatory behavior resembles streaking, but differs in that it originates from EWP interference, with opposite modulations of the kinetic energy. It requires significantly lower intensities than streaking. Consequently, it is not the full spectrum that is shifted around its center of mass, but rather the individual main bands.

For the CEP of 0°, the APT consists of three attosecond pulses, located at $-0.5\,T_0$, 0 and $0.5\,T_0$, as seen on the Wigner distribution in Fig 4.6d. The phase shift imprinted by the IR field is the same between the two outermost EWPs, since their temporal separation is equal to an optical period (same sign of **A**). In contrast, the shift of the central EWP is opposite to that of the outermost ones since the sign of **A** is opposite. However, whether it is the EWP at $-0.5\,T_0$ or at $0.5\,T_0$ which comes closer to the central one does not play a role. Therefore, the LAP spectrum, shown in Fig 4.6b, now resembles RABBIT with sidebands appearing in-between the main bands that oscillate at the laser period with delay.

These results show the strong connection between the LAP interference pattern and the number of attosecond pulses. Therefore, LAP spectra can be used to analyze the structure of the attosecond pulse train. For example, we consider the case where the CEP value is 45° in Fig. 4.7a. Two distinct spectral regions can be identified, delimited by the dotted line. At low (high) energies, a three-pulse (two-pulse) interference pattern arises due to the presence of three (two) attosecond pulses in the low (high) energy region, as seen on the Wigner distribution in Fig. 4.7b. This type of interpretation is used in **Paper II** to characterize the APT, and therefore the HHG process.

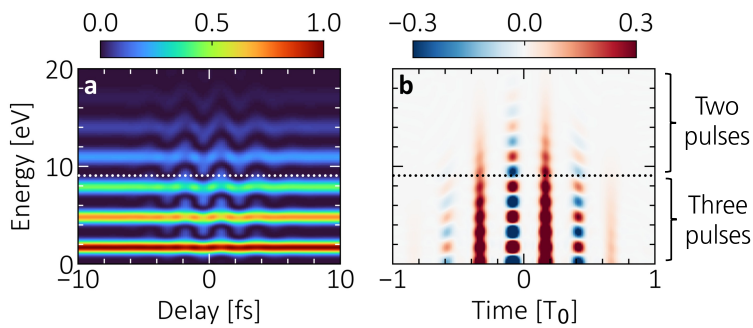

Figure 4.7: **Simulated LAP spectrum for a spectrally varying number of attosecond pulses.** (a) Photoelectron counts as a function of the XUV-IR delay and of the kinetic energy. A selection on electrons emitted in the upper hemisphere is performed. (b) Wigner distribution of the APT where the energy axis is shifted by the helium ionization potential. The laser used to generate the APT and dress the photoionization has a duration of 6 fs and a CEP of 45°.

2 Experimental method

2.1 Pump-probe interferometer

In **Papers II, III and VI**, LAP measurements are performed using the pump-probe interferometer shown in Fig. 4.8 [72]. Directly at the output of the OPCPA, the CEP of the few-cycle pulses is stabilized on a shot-to-shot basis with a feedback loop from the SATI to a wedge pair in the oscillator (see Chapter 2.1). The CEP-stable pulses are then split at the entrance of the HHG chamber into a pump (red) and a probe (orange) arm. In the former, HHG in argon produces a comb of broad harmonics (short APTs). The remaining IR is blocked with a 200 nm thick aluminum filter, through which the XUV is transmitted. The XUV pump is finally recombined with the IR probe using a hole-drilled mirror. Both co-propagating light fields are focused by a toroidal mirror into a vacuum chamber containing helium. The PAD of the photoelectrons is measured with the CIEL (Coïncidences entre Ions et Électrons Localisés) spectrometer, described in the next section.

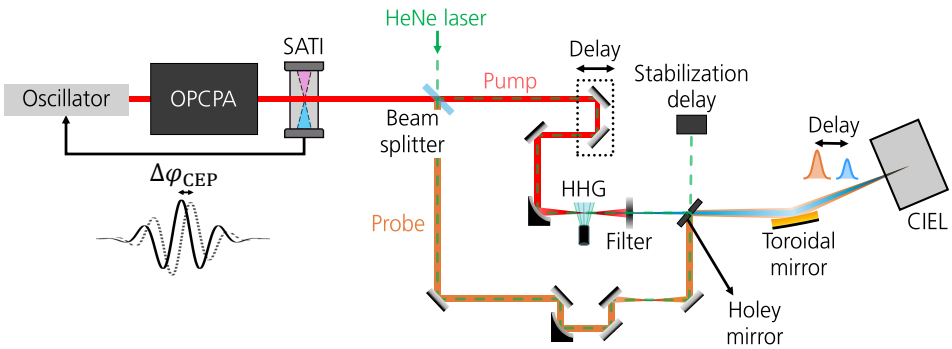

Figure 4.8: Pump-probe set-up for LAP experiments. Few-cycle CEP-stabilized pulses from the laser are split into a pump (red) and a probe (orange) arm by a beam splitter. In the pump arm, attosecond pulses are generated and temporally delayed relative to the probe field. The pump and probe are recombined with a holey mirror and focused by a toroidal mirror into the three-dimensional reaction microscope (CIEL).

Laser-assisted photoionization spectra are acquired by controlling the XUV-IR delay τ with a translation stage in the pump arm. An active delay stabilization with a typical accuracy of 26 as [72] is used, which relies on a helium-neon (HeNe) laser that follows the beam path of the pump and the probe (in green).

2.2 Three-dimensional momentum detector

In this thesis, we discuss aspects of photoionization which can only be experimentally observed if angle selection on the PAD is possible. Therefore, the three-dimensional momentum of the photoelectrons is measured with the CIEL, which is a so-called reaction microscope [88, 89]. Particle detection with the CIEL, schematically illustrated in Fig. 4.9a, relies on the use of electric and magnetic fields to collect the charged particles produced after each laser shot and to reconstruct their initial momentum $\mathbf{p}$.

Following their interaction with the light field, particles possessing large transverse momenta -which

might otherwise escape- are confined transversely by a homogeneous magnetic field, applied along the detector axis. An electric field is additionally used to accelerate particles of opposite charge in opposite directions. After traveling a distance L, the particles reach position sensitive detectors, consisting of a MCP coupled to a delay-line anode detector (DLD). These detectors provide the impact position (transverse position x and y) as well as the time-of-flight t_{TOF}, which is the time taken by a particle to reach the detector from its initial position, and is therefore related to the longitudinal position z. From the detectors' information, the initial momentum is calculated analytically by projecting on each axis Newton's law of motion, solely governed by the Lorentz force $\mathbf{F} = q\,(\mathbf{E} + \mathbf{v} \times \mathbf{B})$.

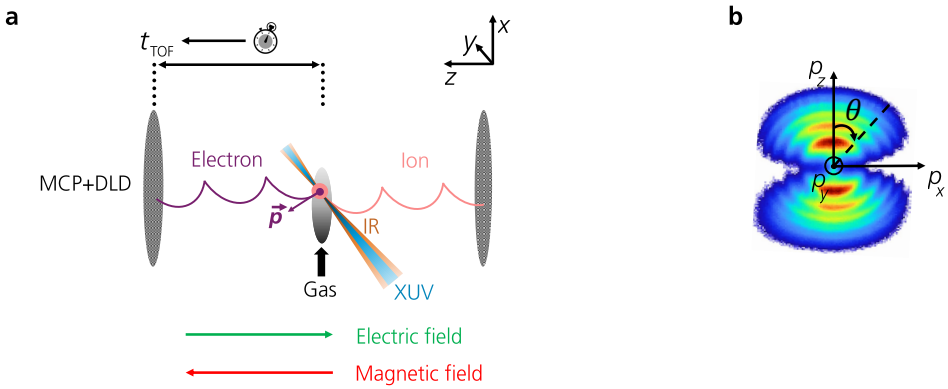

Figure 4.9: Working principle of the CIEL spectrometer. (a) Schematic of the CIEL. After interaction with the light, an electric and magnetic field collect the electrons. The time-of-flight and impact position on the detector is recorded, thus giving information about the initial momentum of the electrons. MCP: Microchannel plate. DLD: Delay-line anode detector. (b) Experimental PAD arising from photoionization of helium by short APTs, linearly polarized along $\mathbf{z}$. Rings arise due to photoionization by different harmonics.

In Fig. 4.9b, the momentum of photoelectrons ionized from helium by an attosecond pulse train with linear polarization along z is shown in the x–z plane. Circular wings, due to absorption of harmonics, are seen in the upward and downward directions, and are characteristic of a p–wave. Given that the time-of-flight depends on the particle energy and mass, knowledge about the parent ion for each electron is accessible with post data processing, and electrons and ions are said to be measured in coincidence. This enables photoionization studies of gas mixtures. It is also important to mention that the detectors have a dead time and radius, such that two close impact events (in space or time) can lead to a detection ambiguity. For single photoionization, a straightforward solution consists in restricting the number of photoionization event per laser shot to less than one, for example by using low gas densities or controlling the flux of the ionizing radiation. The trade off is a longer acquisition time, which is compensated for by the high repetition rate of our laser system.

The particularity of this LAP set-up comes from two main experimental choices. On the one hand, few-cycle laser pulses with controllable CEP are used to generate the harmonics but also to dress the photoionization experiments. On the other hand, the CIEL detector gives access to the angularly-resolved PAD. Together, these features enable us to study LAP with ultrashort pulses in both the time and spectral domains.

3 Experimental results

In this section, we discuss the LAP measurements performed in **Papers II, III and VI** using the set-up described above. An intermediate regime between streaking and RABBIT arises, where interference patterns are highly sensitive to the light field properties. It then becomes possible to carry out different experiments "simply" by tuning the driving laser parameters (e.g. CEP, duration, intensity). First, LAP experiments with APTs made up by two to four attosecond pulses are interpreted in the temporal domain to learn more about the intricate temporal and spectral properties of the XUV radiation. Then, the point of view is shifted to the spectral domain in order to describe the interference between quantum paths of different parities. Finally, the sensitivity of interference effects involving highly excited states of helium to the properties of the laser probe field is investigated.

3.1 Characterization of APTs

In **Paper II**, LAP spectra are acquired in helium for two different values of the CEP having a relative separation of 90°. The results are presented in Fig. 4.10a and c, and three-dimensional simulations detailed in the paper allow determining their CEP values to 70° and 160°, respectively. As seen in Section 2.2, the spectrograms can be interpreted as interference between EWPs, and therefore depend on the number of attosecond pulses that interfere in the temporal domain. As a consequence, a decreasing number of attosecond pulses with energy is expected due to harmonics with higher energies being generated during a shorter time (see Chapter 3). For the 70° CEP (Fig. 4.8a), the spectra have the expected behavior.

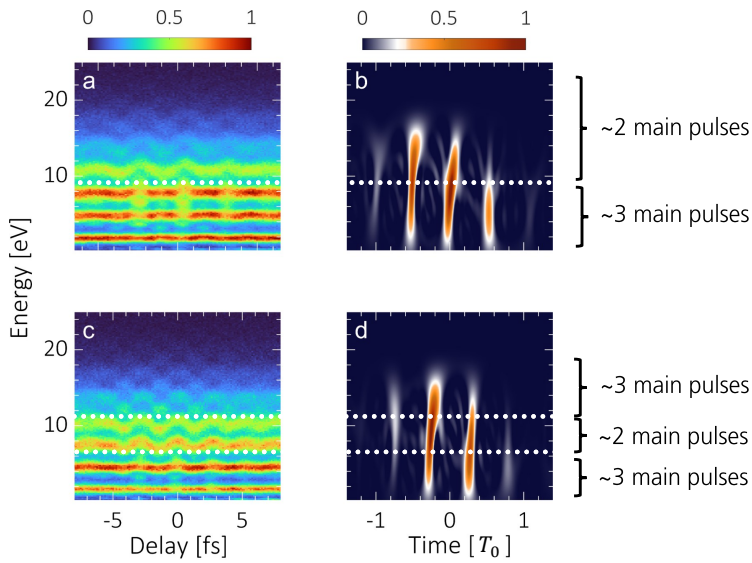

Figure 4.10: **Experimental LAP spectra in helium for two different CEP values.** (a,c) Photoelectron counts in the upward direction as a function of the XUV-IR delay and of the kinetic energy. (b,d) Wigner distribution of the APT where the energy axis is shifted by the helium ionization potential. Adapted from **Paper II**.

The interference pattern in Fig. 4.10c, however, presents a different energy-dependence from what we have seen so far. The pattern exhibits RABBIT-like features at low energies, from 0 to 6 eV, as well as oscillations of the kinetic energy with the delay between 6 and 11.5 eV. Above 11.5 eV, it presents main- and sidebands, with a "chessboard" pattern. This unexpected feature in the highest energy spectral range should be associated with three attosecond pulses in the temporal domain. We verify this by extracting the spectro-temporal properties of the XUV radiation from the photoelectron spectra.

The complete spectro-temporal characterization of the XUV can be obtained from retrieval techniques, developed as direct extensions of frequency-resolved optical gating (FROG) [90, 91, 92, 93, 94, 95]. These methods rely on minimizing the root mean square error between the entire experimental spectrum and a spectrum simulated with the SFA. Starting from an initial guess for the light fields, the algorithm iteratively refines them until a convergence criterion is reached. In **Paper II**, we apply the refined extended Ptychographic Iterative Engine (ePIE) [91, 92] to retrieve short attosecond pulse trains. The procedure begins with a reduced number of ePIE iterations, that make use of the central momentum approximation (CMA), in which the photoelectron momentum is approximated by its central value in the SFA equation. The resulting XUV and IR fields then become the initial guess in the so-called "Volkov transform" generalized projections algorithm (VTGPA), which can converge to a more physical solution as it does not rely on the CMA approximation [94].

The Wigner distributions of the retrieved APTs are shown in Fig. 4.10b,d. In Fig. 4.10b, three main pulses are visible at low energies and two main ones at higher ones. In contrast, Fig. 4.10d displays two dominating pulses up to 10 eV and three pulses at energies above, which give the chessboard pattern. Until now, the three step model alone could explain the spectra. However, it cannot account for the non-trivial change in the number of pulses observed in Fig. 4.10d. With the help of the three-dimensional macroscopic HHG simulations and the analytical one-dimensional model developed in the previous chapter, we found that the macroscopic temporal confinement of high-order harmonics could modulate the spectral amplitude of each attosecond pulse in the train. This means that macroscopic effects during HHG can impact the energy-dependent number of attosecond pulses, which in return can be detected with a very sensitive pulse characterization method like LAP.

3.2 Parity-mixing interference

In **Paper III**, LAP of helium atoms is performed in a situation where there is a constant number of attosecond pulses at all energies, while still having broad harmonics (3 or 4 attosecond pulses). The resulting photoelectron spectrum is shown in Fig. 4.11a. Only photoelectron emitted in the upper hemisphere of the detector ($p_z > 0$) are shown. At long delays, the XUV and IR fields do not temporally overlap such that broad main bands are visible, indicated by white dotted lines. At short delays (around 0 fs), broad sidebands oscillating at 2ω appear between the main bands, indicated by white dashed lines. It is possible to see that the sidebands extend up to the main bands. This overlap is expect to give rise to parity-mixing (see Fig. 4.5).

The amplitude of the Fourier transform, computed along the delay axis, is presented in Fig. 4.11b. The frequency axis is normalized to the central IR probe frequency ω_0. Both the main- (white dotted lines) and sidebands (white dashed lines) present signal in a finite range of frequencies around $2\omega_0$,

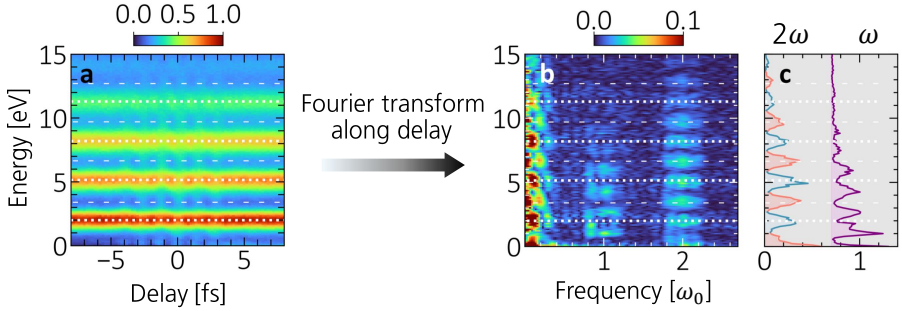

Figure 4.11: Measurement of the parity-mixing signal. (a) Counts of photoelectrons emitted upwards (in color) as a function of kinetic energy and XUV-IR delay. (b) Amplitude of the spectrum Fourier transform. (c) Projection on the energy axis of the signal at ω (purple) and 2ω (red and blue). White dotted (dashed) lines indicate the positions of the main- (side-) bands.

while the main bands exhibit additional oscillations close to ω_0. The signal at 2ω is projected onto the energy axis in Fig. 4.11c. It is strongest at the center of the main- (blue) and sidebands (red) and is directly related to the traditional RABBIT scheme in which long APTs are used (see Fig. 4.5). On the other hand, the signal at ω is neither centered on the main bands nor on the sidebands, as shown by the purple curve. It overlaps with the red and blue curves, and its strength decreases towards the centers of the main- and sidebands, where the overlap is reduced. This confirms that it originates from parity-mixing.

Figure 4.12a shows the logarithm of the Fourier amplitude for the two lowest-energy main bands. The signal at ω splits into two components, red- and blue-shifted relative to the central IR frequency ω_0. The results are reproduced theoretically for our experimental parameters by solving the three-dimensional time-dependent Schrödinger equation (TDSE) [96, 97, 98, 99]. The resulting Fourier transform amplitude is shown in Fig. 4.12b in logarithmic scale. The fourfold pattern is reproduced, with each substructure being indicated by roman numbers. Their physical origin is detailed below.

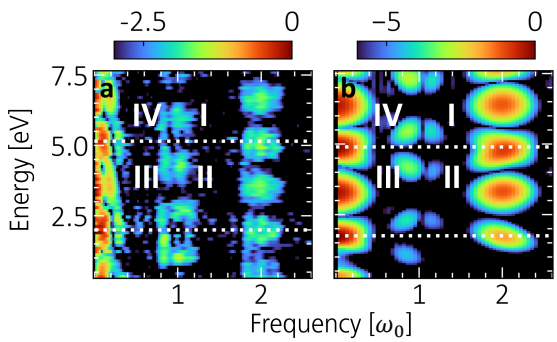

Figure 4.12: Spectral amplitude of the parity-mixing signal. (a) Experimental and (b) theoretical spectral amplitudes for the two lowest energy main bands. Roman numbers indicate the four different substructures. The central energy of the main bands are indicated by white dotted lines. Adapted from **Paper III**.

Figure 4.13a illustrates the interference pathways involving different frequencies of the probe spec-

trum (Fig. 4.13b) by colored arrows. It can be seen that the blueshifted components arise from interference involving two different main bands ("inter-harmonic" interference). For instance, a final state in region I (II) can be reached by a two-photon transition involving absorption of the harmonic $q+2$ ($q-2$) and emission (absorption) of a probe photon but also by a one-photon transition involving absorption of the harmonic q. These two-photon transitions require high probe frequencies (above ω_0), as indicated for two different ones with purple and blue arrows in Fig. 4.13b.

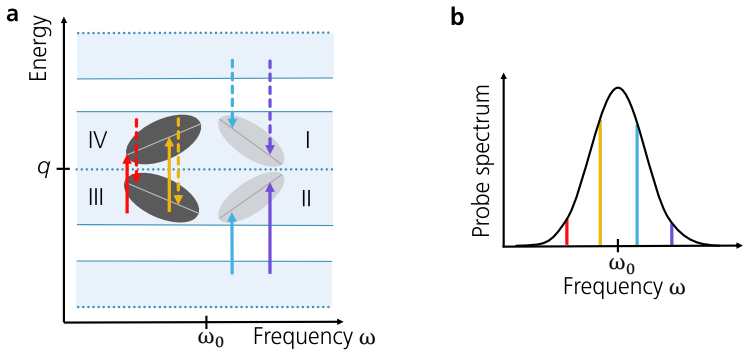

Figure 4.13: Quantum pathways leading to parity-mixing in the main bands. (a) Schematic illustrating interference pathways between final states of even and odd parity corresponding to "inter-" (I and II) and "intra-" harmonic (III and IV) interference. Interference involving different IR frequencies are shown with different colors, see probe spectrum in (b). Adapted from **Paper III**.

Conversely, the redshifted components arise from interference involving a unique main band ("intra-harmonic" interference). Typically, a final state in region III (IV) can be reached by a two-photon transition involving absorption of the harmonic q and absorption (emission) of a probe photon but also by a one-photon absorption of the same harmonic (q). These two-photon transitions occur for low probe frequencies (below ω_0), as indicated by red and yellow arrows in the schematic.

For a sufficiently large spectral range of the probe, the substructures can overlap at the central probe frequency and in the middle of the main bands. However, no signal is observed, which can be understood by considering the experimental and theoretical phase map, shown in Fig. 4.14a,b. Adjacent substructures indeed exhibit a π phase difference, which is due to the fact that I and III involve the emission of a probe photon, whereas II and IV involve the absorption of a probe photon.

In the paper, we derived a simple theoretical framework based on TDPT and the partial wave expansion, which leads to the following expression for the parity-mixing signal integrated in the upper hemisphere of the detector

$$\begin{aligned} S_{\mathrm{PM}}(\tau) = 2\sum_{\ell=0,2} c_\ell \Re\Big\{ & \mathcal{E}^*_{\mathrm{IR}}(\omega)\mathcal{E}_{q+2}(\Omega_+)\mathcal{E}^*_q(\Omega)e^{-i\omega\tau}M^{(2,-)}_{\ell 10}M^{(1)*}_{10} \quad \rightarrow \text{(I)} \\ \text{(II)} \leftarrow \quad & +\mathcal{E}_{\mathrm{IR}}(\omega)\mathcal{E}_{q-2}(\Omega_-)\mathcal{E}^*_q(\Omega)e^{i\omega\tau}M^{(2,+)}_{\ell 10}M^{(1)*}_{10} \\ \text{(III)} \leftarrow \quad & +\mathcal{E}^*_{\mathrm{IR}}(\omega)\mathcal{E}_{q}(\Omega_+)\mathcal{E}^*_q(\Omega)e^{-i\omega\tau}M^{(2',-)}_{\ell 10}M^{(1)*}_{10} \\ \text{(IV)} \leftarrow \quad & +\mathcal{E}_{\mathrm{IR}}(\omega)\mathcal{E}_{q}(\Omega_-)\mathcal{E}^*_q(\Omega)e^{i\omega\tau}M^{(2',+)}_{\ell 10}M^{(1)*}_{10}\Big\}. \end{aligned} \tag{4.18}$$

where $c_0 = \sqrt{3}/4$, $c_2 = \sqrt{15}/16$, $\Omega_\mp = \Omega \mp \omega$ and Ω are the intermediate and final state

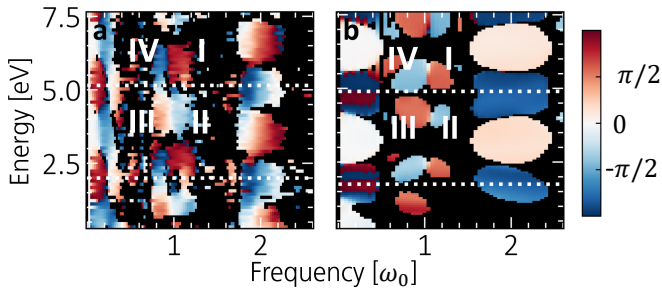

Figure 4.14: Spectral phase of the parity-mixing signal. (a) Experimental and (b) theoretical spectral phase for the two lowest energy main bands. Roman numbers indicate the four different substructures. The central energy of the main bands are indicated by white dotted lines. Adapted from **Paper III**.

frequencies, $M_{\ell 10}^{(2,\pm)}$ and $M_{\ell 10}^{(2',\pm)}$ are the two-photon transition matrix elements involving different harmonics and only the q-th harmonic, respectively. Each of the four terms correspond to one of the interference regions (I, II, III and IV) and involves different two-photon matrix elements or harmonic fields. Interestingly, one can see that the sum of the first and second term resemble a RABBIT expression such that similar information than that given by RABBIT can be obtained, in addition to new information from the intra-harmonic interference terms. From Eq. (4.2) and (4.9), one can see that $\mathcal{A}^{(1)} \propto i$. Neglecting the small contributions to the phase, this gives $\Re\{ie^{\pm i\omega\tau}\} = \pm\sin(\omega\tau)$, showing that the two terms corresponding to regions I and II or similarly III and IV are approximately out-of-phase. The same argument applies for the two terms corresponding to region II and III (or I and IV). This phase shift enables distinguishing the various terms in the Fourier domain, making LAP schemes with broadband fields very powerful.

3.3 Quantum beats

In previous sections, direct photoionization to a continuum state by absorption of an XUV photon was discussed. However, it may occur that an harmonic is resonant with Rydberg states, which are highly excited bound states lying below the ionization threshold. The electron yield then exhibits features due to those below-threshold states [100, 101], which we investigate below in connection to **Paper VI**.

Figure 4.15a shows a spectrogram acquired in helium for a long delay range (-15 to 70 fs). In the low-energy region, below the first main band, the electron yield oscillates as a function of delay with a period of 14 fs (see black arrow). In this experiment, the 15-th harmonic is resonant with the $1s3p$, $1s4p$, $1s5p$ and $1s6p$ Rydberg states, as illustrated schematically by the blue arrow and Gaussian area in Fig. 4.15b. As a result, the excited atom is in a superposition of these states, which can be described by

$$|\Psi\rangle = |i\rangle + \sum_{j>0} c_j |j\rangle \,, \tag{4.19}$$

where $|j\rangle$ are the electronic states and c_j their coefficients with $\rho_{jj} = |c_j|^2$ being the population. The binding energies ε_{1snp} ($n = 3, 4, 5, 6$) of the Rydberg states being small, subsequent absorption of an IR probe photon (red arrows) ionizes the system.

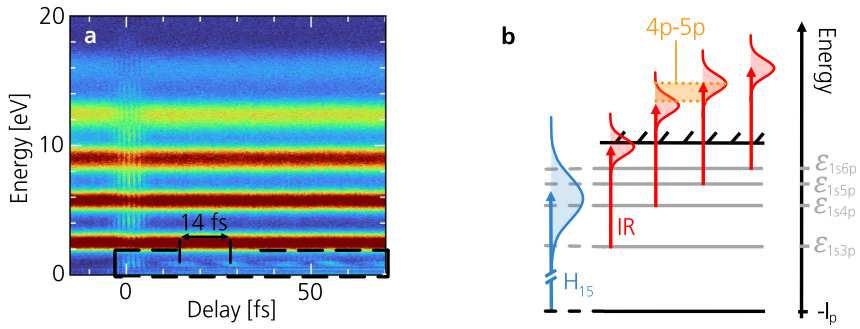

Figure 4.15: Long LAP measurement in helium. (a) Experimental photoelectron yield (in color) as a function of energy and delay. Slow oscillations with a period of 14 fs (black arrow) arise in the low energy region, indicated by the black dashed lines. (b) Schematic of the two-photon transitions involved in the energy signal below 1 eV (quantum beats). The harmonic 15 excites helium (blue arrow) since it is resonant with the $1snp$ Rydberg states ($n = 3, 4, 5, 6$), indicated in gray. The IR produces electron wavepackets (red arrows). Due to its broad bandwidth, quantum paths involving different Rydberg states interfere coherently, for example the $1s4p$ and $1s5p$ (in orange).

Because of the IR broad spectral width (red Gaussian areas), two-photon ionization pathways involving different Rydberg states may overlap spectrally, and thereby interfere coherently. This type of interference is known as quantum beat, and has an oscillation period given by

$$T_{np-mp} = h(\varepsilon_{1snp} - \varepsilon_{1smp})^{-1}, \tag{4.20}$$

where $n \neq m$. In the data presented here, the experimental signal primarily arises from interference between the $1s4p$ ($\varepsilon_{1s4p} = -0.85$ eV) and $1s5p$ ($\varepsilon_{1s5p} = -0.54$ eV) states, where the period $T_{4p-5p} = 13.3$ fs is consistent with the experimental one.

A closer inspection of the energy region below 1 eV in Fig. 4.16a reveals an energy-dependent shift of the oscillation maxima, resulting in a linear tilt with a slope of approximately -0.1 fs/eV (black dashed line). In **Paper VI**, a retrieval algorithm based on Monte-Carlo methods is developed to find the complex IR field and coefficients c_j. Starting from an initial guess, the parameters are iteratively refined to reproduce the spectrogram until a convergence criterion is reached.

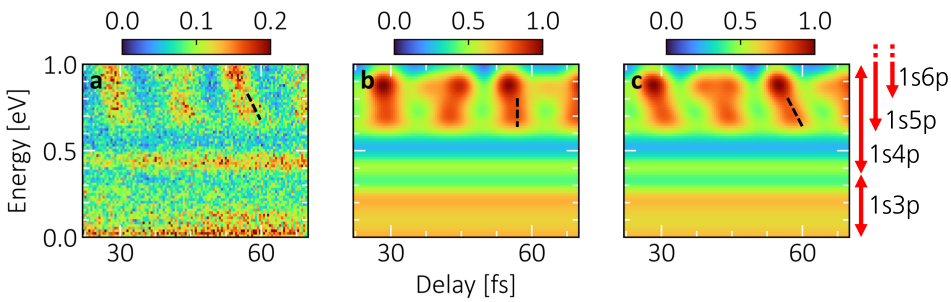

Figure 4.16: Quantum beats. Low-energy region of the spectrogram corresponding to the area indicated by black dashed lines in Fig. 4.15. Red arrows indicate in which spectral regions the contribution due to a given Rydberg state is relevant. (a) Experimental spectrogram. Spectrogram simulated (b) with and (c) without a flat IR spectral phase.

Figure 4.16b displays the reproduced spectrogram assuming a flat IR spectral phase. The main

features, including the oscillation period and relative amplitudes, are well reproduced thus already demonstrating that the IR spectral amplitude and excited states distribution across the resonant harmonic play a major role in the measurement. Nevertheless, the energy-dependent tilt is not reproduced within this approximation. Allowing the IR spectral phase to vary in the retrieval leads to excellent qualitative and quantitative agreement with the experiment, including the energy-dependent tilt (see Fig. 4.16c). Therefore, the tilt is a direct consequence of the probe field spectral phase.

Importantly, this study shows that the Gaussian and flat spectral phase approximations fail. Characterizing the spectral amplitude and phase of the light fields is thus essential to understand and extract information from measurements, since in general few-cycle pulses unavoidably present a complex structure (see Chapter 2). More broadly, a robust method to extract the probe field properties is also developed.

4 Further developments

This section presents unpublished studies related to the results of **Paper III**.

4.1 Extraction of quantitative information about photoionization

Laser-assisted photoionization measurements using long pulses have been extensively used to extract the atomic time delays associated to the one- or two-photon transitions. The idea is to study the phase and amplitude of the sideband signal and extract information from it. However, this method suffers from the various contributions to the phase, in particular due to the light fields or to the various angular momentum channels. For a given scattering channel, the two-photon transition atomic phase can be written as the sum of two terms [85]:

$$\phi^{\pm}_{\ell\lambda L} = \eta_{\lambda L} + \phi^{\pm}_{\mathrm{cc},\ell\lambda}, \tag{4.21}$$

where $\eta_{\lambda L}$ is the one-photon phase from the XUV-induced $L \rightarrow \lambda$ transition and $\phi^{\pm}_{\mathrm{cc},\ell\lambda}$ arises from the continuum-continuum transition due to interaction with the IR. A method to access the individual terms in this phase currently consists in applying the following procedure [102, 103, 38]:

(1) The PAD is decomposed in Legendre polynomials by fitting the electron yield as a function of the polar angle θ to Eq. (4.16) for each energy and delay. The fitted b_n coefficients provide a "data set", i.e. a system of equations with shared parameters. The experimental b_0, b_2 and b_4 for the experimental data in **Paper III** are shown in Fig. 4.17. The electron yield oscillates at 2ω with the delay.

(2) The theoretical expression for the PAD, given by

$$S_{\mathrm{SB}}(\tau,\theta) = \left| \sum_{\ell} \left[a^{(2,+)}_{\ell 10}(\tau) + a^{(2,-)}_{\ell 10}(\tau) \right] Y_{\ell 0}(\theta) \right|^2, \tag{4.22}$$

is expanded. The resulting terms, which involve squared spherical harmonics or cross-products between different ones, are converted into a linear sum of Legendre polynomials using Eq. (4.4). This yields an expression for h_0, h_2 and h_4, which we give in Appendix 1 for helium.

(3) Finally, the shared parameters are simultaneously fitted to the experimental h_n, yielding information about each scattering channel.

In helium, the number of unknown parameters and of equations should allow retrieving two information about the two-photon process: the difference between the continuum-continuum phases in each scattering channel $\phi^{\pm}_{\mathrm{cc},01} - \phi^{\pm}_{\mathrm{cc},21}$ as well as the ratio between the channel-resolved two-photon transition amplitudes $|M^{(2,\pm)}_{010}|/|M^{(2,\pm)}_{210}|$. However, it can be shown that there are convergence issues since the system of even h-parameters (h_0, h_2 and h_4) remains unchanged under the simultaneous substitutions

$$\begin{aligned} \phi^{+}_{\mathrm{cc},01} &\leftrightarrow \phi^{+}_{\mathrm{cc},21}, & |M^{+}_{010}| &\leftrightarrow |M^{+}_{210}|, \\ \phi^{-}_{\mathrm{cc},01} &\leftrightarrow \phi^{-}_{\mathrm{cc},21}, & |M^{-}_{010}| &\leftrightarrow |M^{-}_{210}|. \end{aligned} \tag{4.23}$$

This ambiguity in solution, detailed in Appendix 1, requires prior knowledge about the photoionization process. For example, Fano's propensity rule [104, 105] was assumed in [38], which states that upon absorption (emission) of a laser photon, the scattering channel of highest (lowest) orbital angular momentum is favored.

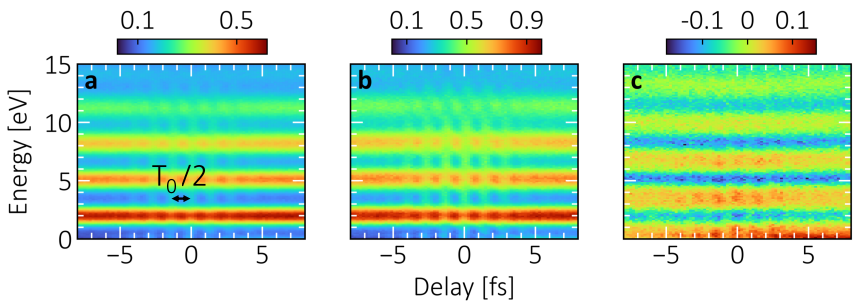

Figure 4.17: **Expansion of experimental data in Legendre polynomials.** Extracted (a) h_0, (b) h_2, (c) h_4 coefficients obtained by fitting the experimental data of **Paper III**.

For LAP with broadband fields, an asymmetry relative to the plane perpendicular to the light field polarization arises in parity-mixing regions due to the parity properties of spherical harmonics, which is described using odd Legendre polynomials. The experimental h_1 and h_3 are shown in Fig. 4.18, in which the photoelectron yield oscillates at ω, as expected for parity-mixing interference.

We show that applying a global fit procedure to the odd parameters allows retrieving the scattering channel information without convergence issues nor requirement for prior knowledge. For intra-harmonic parity-mixing interference (region III and IV), the odd parameters are expressed as

$$\begin{aligned} h_1(\tau) = \mathcal{F}_{\mathrm{IR}}(\omega)\mathcal{F}_q(\Omega_{\mp})\mathcal{F}_q(\Omega)|M^{(1)}_{10}|\big[\sqrt{3}|M^{(2',\pm)}_{010}|\cos\left(\omega\tau \pm \Delta\Phi^{\pm}_0\right) \\ + \frac{2\sqrt{15}}{5}|M^{(2',\pm)}_{210}|\cos\left(\omega\tau \pm \Delta\Phi^{\pm}_2\right)\big], \end{aligned} \tag{4.24}$$

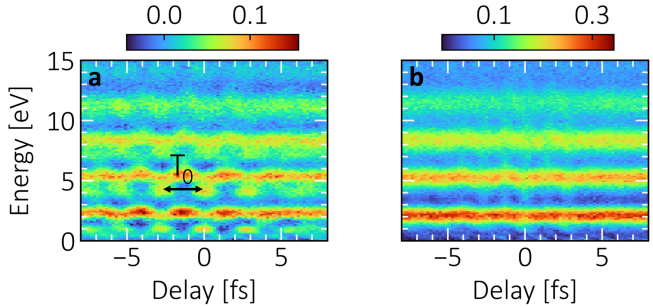

Figure 4.18: Expansion of experimental data in odd Legendre polynomials. Extracted (a) h_1 and (b) h_3 coefficients obtained by fitting the experimental data of **Paper III**.

$$h_3(\tau) = \frac{3\sqrt{15}}{5}\mathcal{F}_{\mathrm{IR}}(\omega)\mathcal{F}_q(\Omega_\mp)\mathcal{F}_q(\Omega)|M_{10}^{(1)}||M_{210}^{(2',\pm)}|\cos\left(\omega\tau \pm \Delta\Phi_2^\pm\right), \tag{4.25}$$

where $\mathcal{F}_i = |\mathcal{E}_i|$ denotes the modulus field amplitudes, $\Delta\Phi_\ell^\pm(\Omega) = \varphi_{\mathrm{CEP}} + \Delta\phi_{\mathrm{XUV}}(\Omega_\mp) + \Delta\eta_{10}(\Omega_\mp) + \phi_{\mathrm{cc},\ell 1}^\pm(\Omega)$ with $\Delta\eta_{10}$ being the phase difference between one-photon transitions induced by absorption of the XUV frequency Ω and $\Omega_\mp$.

Both $\Delta\Phi_0^\pm$ and $\Delta\Phi_2^\pm$ contain the same offset $\varphi_{\mathrm{CEP}} + \Delta\phi_{\mathrm{XUV}} + \Delta\eta_{10}$, such that fitting them gives access to the difference between the continuum-continuum phase differences:

$$\Delta\Phi_0^\pm - \Delta\Phi_2^\pm = \phi_{\mathrm{cc},01}^\pm - \phi_{\mathrm{cc},21}^\pm. \tag{4.26}$$

In addition, the prefactors in h_1 and h_3 scale as $A_{\ell 10}^\pm \propto |M_{10}^{(1)}||M_{\ell 10}^{(2',\pm)}|$, such that they only differ by the two-photon transition matrix elements. Fitting $A_{\ell 10}^\pm$ allows retrieving the two-photon amplitude ratios:

$$\frac{A_{010}^\pm}{A_{210}^\pm} = \frac{|M_{010}^{(2',\pm)}|}{|M_{210}^{(2',\pm)}|}. \tag{4.27}$$

This equation is related to Fano's propensity rule [104, 105]. When only the radial part is considered, the ratio is superior (inferior) to 1 for the emission (absorption) case.

Figure 4.19 shows the results from this global fit procedure performed on the TDSE data for the intra-harmonic interference signal (selected by applying a filter in the Fourier domain). Black dots indicate the fit results while the purple and blue curves are theoretical data obtained from [106] and [107], respectively. The fitted continuum-continuum phase differences, displayed in Fig. 4.19a and c, align with the theory. The agreement is also good for the radial amplitude ratios (see Fig. 4.19b and d), as the correct favored scattering channel is retrieved. As explained before, only two energies are accessible in the experiment and there is a limited spectral resolution, such that application to the experimental data would require better measurements. We note that a similar approach can be applied to the inter-harmonic interference signal.

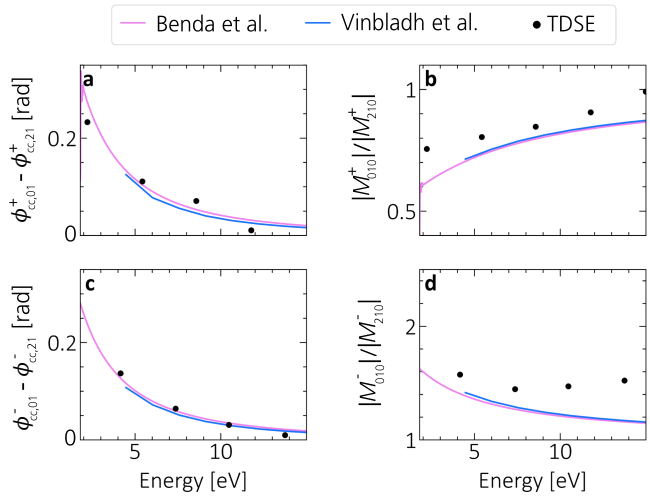

Figure 4.19: **Extraction of continuum-continuum phases and radial scattering channel amplitude ratios from the parity-mixing signal.** Global fit results for the odd b_n parameters (black points), obtained from the intra-harmonic interference signal in helium TDSE calculations. (a,c) Difference of continuum-continuum phases for the absorption and emission of an IR photon. (b,d) Ratio of scattering channel radial matrix element amplitudes for the absorption and emission of an IR photon. The blue and purple curves are theoretical data obtained from [106, 107].

4.2 Interference pattern at low-beating frequencies

Fourier analysis of LAP measurements (see Fig. 4.11b) reveals electron-yield oscillations at low frequencies, below $0.4\omega_0$. Signal due to parity-mixing interference can be suppressed by integrating over all photoemission directions. The resulting Fourier amplitude is presented in Fig. 4.20a. The persistence of the low-frequency signal indicates that it originates from the interference between ionization pathways of same parity. A notable feature of this signal is the pronounced variations of its amplitude with frequency. Similar observations can be made for the spectral phase, displayed in Fig. 4.20b.

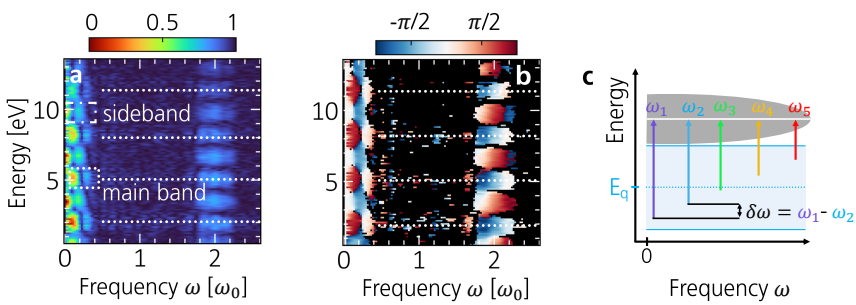

Figure 4.20: **LAP measurement for all photoelectrons.** Measured spectral (a) amplitude and (b) phase of photoelectrons emitted in all directions. White dotted lines indicate the positions of the main bands. (c) Energy transitions involved in the signal at low frequencies for the absorption scheme. The different IR frequencies are represented by the colored arrows. For sake of simplicity, only transitions from a given main band q to a sideband are shown. Similar interference exists for the emission case.

This contribution stems from interference between two-photon ionization pathways that involve the absorption (or emission) of IR photons with different frequencies. The relevant energy transitions are illustrated in Fig. 4.20c for the absorption process. Transition involving absorption of an IR photon of frequency ω_1 (purple arrow) can interfere with those absorbing an IR photon of lower frequency ω_2 (blue arrow), leading to oscillations at the difference frequency $\delta\omega = \omega_1 - \omega_2 \ll \omega_0$. Naturally, many such frequency combinations also contribute (e.g. see green, yellow and red arrows). Similar interference occurs between transitions involving the emission of IR photons having different frequencies (not shown in the schematic). This interference scheme bares many similarities with an already existing technique called KRAKEN (Kvanttillstånds tomogRafi av AttoseKund ElektroNvågpaket) [20].

Figures 4.21a and b show TDSE simulations performed using Gaussian light fields with a flat spectral phase. Most features cannot be reproduced, e.g. the sideband phase or amplitude modulations. An interesting study would therefore consist in understanding this interference, starting with evaluating the role of the IR spectral phase and amplitude or of the femtosecond chirp of the XUV radiation.

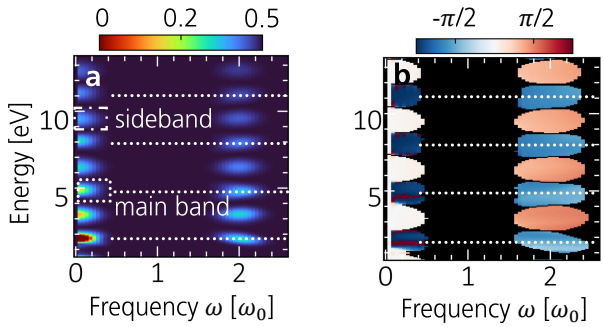

Figure 4.21: LAP simulations for all photoelectrons. Theoretical spectral (a) amplitude and (b) phase of photoelectrons emitted in all directions. White dotted lines indicate the positions of the main bands.

CHAPTER 5

Ultrafast spectroscopy of semiconductors

Ultrafast light–matter interactions in solids give rise to electronic and structural dynamics spanning a wide range of time scales, from attoseconds to picoseconds. Resolving these dynamics requires light sources with sufficiently short pulse durations, such as few-cycle laser and attosecond pulses. In this work, such ultrashort pulses are used for exploring the behavior of electrons in semiconductors using optical and charged-particle detection techniques. Semiconductors are the foundation of modern electronics, from data storage and communication to quantum devices. Silicon has been the workhorse of the semiconductor industry, representing approximately 90% of photovoltaic applications and being ubiquitous in electronic chips [108, 109]. However, continued demands in ever decreasing material dimensions and improved performance have driven the development of commercial devices based on other materials. In particular, compound semiconductors have been replacing silicon in various applications and represent an important area of current ultrafast spectroscopy research.

This thesis focuses on two such systems. In **Paper IV**, SnS thin films in a newly synthesized phase are investigated using ATAS, an all-optical technique combining short attosecond pulses and NIR few-cycle pulses. In **Paper V**, InP nanowires are studied with an energy-resolved PEEM and few-cycle laser pulses, with an emphasis on the effect of their small dimensions on photoemission processes.

This chapter starts by describing the experimental techniques used in this work, ATAS and PEEM. Then, two applications aiming at investigating ultrafast electron dynamics in compound semiconductors are presented.

1 Experimental methods for time-resolved spectroscopy

In isolated atoms, electrons occupy discrete atomic orbitals with well-defined energies. In solids, the atomic orbitals of neighboring atoms overlap due to interactions between valence electrons, resulting in the formation of broad energy bands. The properties of valence electrons are of particular interest since they determine the optical and electronic properties of the material, and can be accessed using visible and NIR light. In contrast, core electrons remain localized around their parent atoms and largely preserve their atomic character. Transitions involving core levels are therefore sensitive to the local environment of a specific element in the material. Such transitions typically lie in the XUV or X-ray spectral range, making XUV spectroscopy adapted to element-specific studies of ultrafast electron dynamics in solids.

ATAS is a technique combining electronic and elemental sensitivity by initiating ultrafast dynamics with a NIR pump pulse and probing the temporal evolution through core-level transitions using XUV attosecond pulses. Since broad spectral bandwidths are needed to resolve the dynamics and access multiple electronic transitions, ultrashort pulses are well suited for this technique.

Beyond probing electron dynamics, intense few-cycle NIR pulses enable the investigation of strong-field and nonlinear photoemission processes. To study these effects in semiconducting nanostructures, a PEEM set-up was implemented during this thesis work. Such a set-up provides surface-sensitive spatial imaging together with access to the emitted electron energy spectrum, making it appropriate for studying ultrafast electron dynamics at the nanoscale.

1.1 Attosecond transient absorption spectroscopy

ATAS relies on absorption spectroscopy, which consists in transmitting light through a sample and measuring changes in the spectrum after propagation. In a typical experimental arrangement, shown in Fig. 5.1, the transmitted intensity is recorded by a spectrometer and follows the Beer-Lambert law:

$$I(\omega) = I_0(\omega)e^{-\alpha(\omega)L} \tag{5.1}$$

where I_0 is the incident intensity, α the absorption coefficient and L the sample thickness. Experimental results are generally presented in terms of the optical density:

$$\mathrm{OD}(\omega) = -\log_{10}\left(\frac{I(\omega)}{I_0(\omega)}\right). \tag{5.2}$$

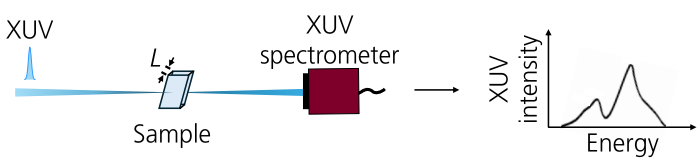

Figure 5.1: Principle of extreme ultraviolet absorption spectroscopy. XUV light is focused onto a sample and the transmitted intensity recorded by a spectrometer.

Absorption spectroscopy in the XUV and X-ray spectral range is referred to as core-level absorption spectroscopy, since photons in this energy range can induce transition from bound core levels to unoccupied states. Figure 5.2a shows the calculated absorption spectra of 0.2 µm thick silicon (Si) and tin (Sn) layers, reproduced from [110]. At the onset of transitions from core levels to the lowest energy unoccupied states, absorption edges occur which correspond to a sudden rise in absorption. Their location is indicated by dotted lines. Absorption edges are conventionally named after the initial electronic shell involved in the transition: K–edge for the 1*s*, L–edge for 2*s* and 2*p*, M–edge for 3*s*, 3*p* and 3*d*, etc... In silicon, two absorption edges are visible, corresponding to a transition from the 2*s* (∼100 eV) and 2*p* (∼150 eV) core levels (L–edge). The edge at 100 eV is significantly sharper, making it easier to detect. In tin, a single pronounced absorption edge appears around 24 eV, and originates from excitations involving the 4*d* core levels (N–edge). In contrast to the deep Si core levels, the N–edge is shallow, and only corresponds to the onset of the 4*d* core levels [111].

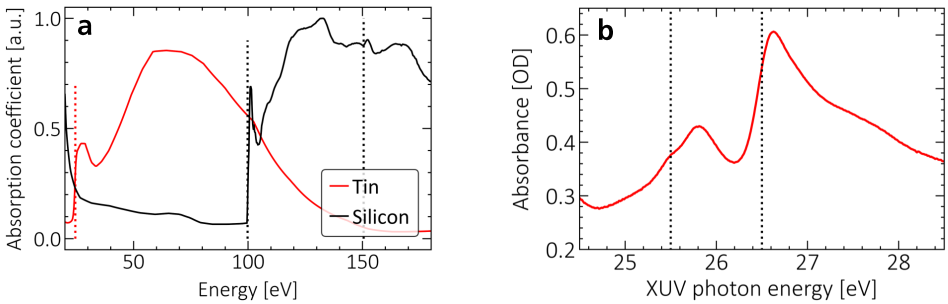

Figure 5.2: Absorption edges of silicon, tin and tin(II) sulfide. (a) Absorption coefficients of Sn and Si as a function of the energy. (b) Absorption spectrum of π-SnS measured with a linearly polarized XUV. The absorption edges are indicated by the vertical dotted lines.

Figure 5.2b shows the optical density of a π-SnS thin film measured using a short APT. Two absorption edges can be identified corresponding to transitions from the Sn $4d_{3/2}$ and $4d_{5/2}$ core levels to the conduction band minimum. This shows that core-level spectroscopy provides good elemental selectivity. This selectivity is beneficial in attosecond experiments employing broadband pulses, where multiple electronic transitions can contribute simultaneously to the measured signal and overlap. In charged-particle detection techniques, these overlapping contributions may complicate the interpretation of ultrafast dynamics.

This thesis focuses on studying electron dynamics with very high temporal and energy resolutions. For this, a pump-probe set-up designed for ATAS, from the group of Stephen R. Leone in Berkeley, was used [112]. The simplified schematic is shown in Fig. 5.3. First, a NIR ultrashort laser pulse (4–5 fs), called the pump, induces changes in the electronic distribution of a sample. Then, a weaker attosecond pulse is recombined with the pump at the sample and its transmitted spectrum is recorded using a diffraction grating and a charge-coupled device camera (15-40 eV energy range). To isolate pump-induced effects, absorption spectra are systematically measured both in the presence and absence of the pump, using a shutter in the pump arm. Results are finally presented in terms

of the differential XUV absorbance:

$$\Delta A(\tau, \epsilon) = -\log_{10}\left[\frac{I_{\mathrm{XUV+pump}}(\tau, \epsilon)}{I_{\mathrm{XUV}}(\tau, \epsilon)}\right], \tag{5.3}$$

where τ is the delay between the pump and the probe, $I_{\mathrm{XUV+pump}}$ and I_{XUV} is the XUV intensity with and without pump field, respectively. By controlling the delay, the temporal evolution of the differential absorbance is obtained, providing insight into the electronic processes at play.

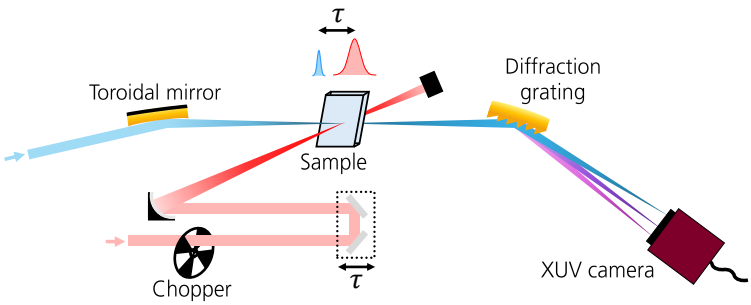

Figure 5.3: **Attosecond transient absorption spectroscopy set-up.** Few-cycle and attosecond pulses are noncollinearly focused onto a sample. At the output, a flat-field grating diffracts the XUV frequencies at different angles, which are recorded with a charge-couple device camera. By varying the delay of the laser, temporal resolution is obtained.

A limitation of ATAS is the restricted range of compatible samples, which must fulfill thickness requirements. If the sample is too thick, the transmitted XUV intensity is strongly attenuated and too weak to measure. In contrast, if the sample is too thin, the changes in absorption cannot be distinguished from the background noise. Therefore, even though nanostructures are of considerable interest, alternative techniques are generally more suitable.

1.2 Energy-resolved photoemission electron microscopy

Investigating electron dynamics in nanostructures can be done using PEEM. It consists in imaging electrons photoemitted from the surface of a sample following interaction with light. More precisely, a set of electrostatic lenses produces a magnified image of the sample surface with high spatial resolution. In this work, a commercial PEEM (Focus GmbH) equipped with a time-of-flight detector was installed, which is schematically illustrated in Fig. 5.4a. A light pulse incident at a 65° angle on a sample's surface photoemits electrons. The electrons reach an extractor, where they are accelerated with a 14 kV voltage. An intermediary image is then formed by the objective lens. At this stage, a contrast aperture may be inserted to improve the resolution. Finally, the electrons go through two consecutive projective lenses, which project the image onto an MCP and a fluorescent screen where the electrons are converted to visible light. The final image is recorded by a camera.

Although the theoretical spatial resolution is limited by electron diffraction, the experimental resolution suffers from aberrations. In principle, the resolution should be in the range of a few nanometers for low energy electrons but in practice is on the order of a few tens of nanometers. Because electron trajectories depend on their kinetic energy, the image focus is typically optimized for a narrow energy bandwidth during experiments. Electrons with different energies are out-of-focus, thereby

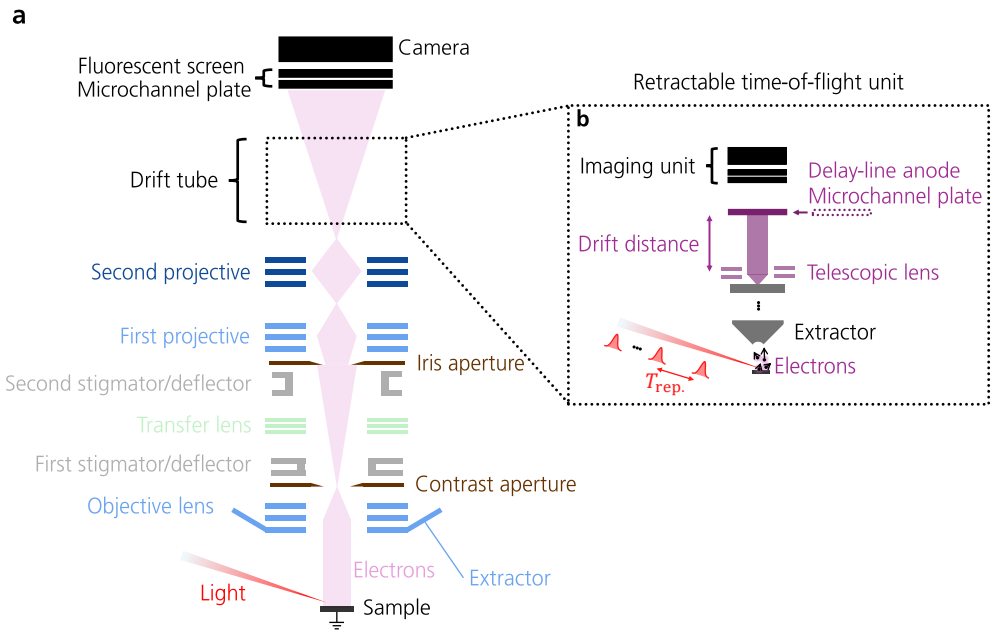

Figure 5.4: Schematic of the Focus TOF-PEEM. (a) Electrons photoemitted by a light pulse enter the PEEM column in the extractor, where they are accelerated before going through a set of various complex lenses. A final magnified image is formed on the imaging unit, consisting of a MCP-fluorescent screen and a camera. In the drift tube, a retractable DLD-MCP detector can be inserted, detailed in (b). This unit operates with a pulsed light source and measures the time-of-flight of the photoelectrons.

blurring the image. In this thesis, photoemission in strong local electric fields is studied, which leads to broad energy bandwidths (up to tens of eV). The spatial feature of the PEEM then allows selecting individual nanowires and measure their photoelectron kinetic-energy spectrum.

The PEEM time-of-flight unit is schematically illustrated in Fig. 5.4b. Two drift tubes kept at a low voltage are inserted after the projective lenses to decelerate the electrons. A retractable DLD-MCP system is placed before the camera imaging unit to measure the time taken by the electrons to reach the detector after photoemission relative to the laser trigger signal at the 200 kHz repetition rate. Electrostatic calculations then relate the time-of-flight to the electron kinetic energy. Figure 5.5a presents the calculated energy resolution against the drift-tube voltage. Lowering drift voltages improve the energy resolution, until a threshold around 10 V. In our experiments, a drift voltage between 20 and 40V is typically used, leading to an energy resolution of approximately 100 meV.

A major limitation of PEEM measurements arises from space-charge effects due to Coulomb repulsion within the cloud of photoemitted electrons. This repulsion changes electron trajectories in the PEEM, thus broadening or shifting the energy spectra and affecting the spatial resolution. To mitigate such issues, the number of electrons per laser shot is kept to an average of one.

Figure 5.5b presents a photoelectron spectrum measured by focusing the OPCPA laser pulses onto an InP nanowire. The shape is a modified Gaussian with a maximum at low kinetic energies. After interaction with the light, an electron may scatter on its way to reach the vacuum, thereby transfer-

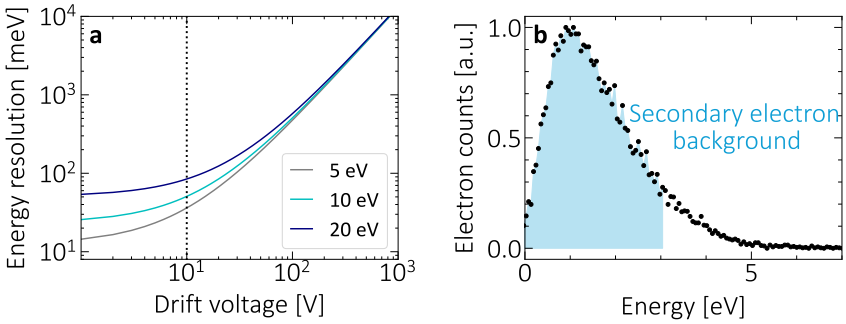

Figure 5.5: PEEM energy feature. (a) Calculated energy resolution as a function of the drift voltage for different electron kinetic energies. A realistic ripple drift voltage of 20 mV and time resolution of 160 ps is used. (b) Electron spectrum measured by focusing the OPCPA laser on an InP nanowire. The blue area approximately indicates the secondary electron background.

ring energy to surrounding electrons. This scattering process produces a large amount of secondary electrons with low kinetic energies. As a consequence, the low-energy region of the spectrum is predominantly due to secondary electrons while contributions to the high-energy regions are mostly due to direct photoemission.

Finally, Fig. 5.6 shows the average distance an electron travels in a solid before it undergoes inelastic scattering as a function of its initial kinetic energy referenced to the Fermi level. Although the curve might vary depending on the material, it provides a satisfactory trend and is generally considered universal. The curve exhibits a minimum around 50-100 eV, going as low as 1 nm. This corresponds to a few atomic layers. Accordingly, electrons photoemitted with these kinetic energies provide highly surface-sensitive information. At lower kinetic energies, such as those typically encountered in NIR strong-field photoemission experiments (∼1.5 eV), it reaches up to 5-10 nm, which remains surface-sensitive.

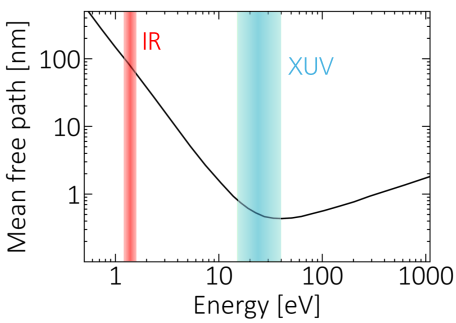

Figure 5.6: Inelastic mean free path of electrons. Curve for the inelastic electron mean free path in elements, taken from [113]. The energy is given relative to the Fermi level. The red and blue shaded area indicate the photon energies of the light sources used in this work.

1.3 Time-resolved photoemission electron microscopy

To resolve electron dynamics with both high temporal and spatial resolution, interferometric optical measurements can be implemented. To this end, an additional toroidal mirror at grazing incidence was installed after the pump-probe interferometer used for LAP experiments to refocus the beams on the PEEM sample, as schematically illustrated in Fig. 5.7a. The spatial profile of the refocused pump (in red) and probe (in orange) is shown in Fig. 5.7b. Their diameter is much larger than that of the nanostructures studied in this work, which ensures uniform illumination. The temporal evolution is then accessed by varying the actively stabilized translation stage in the pump arm, similarly to LAP experiments in atoms.

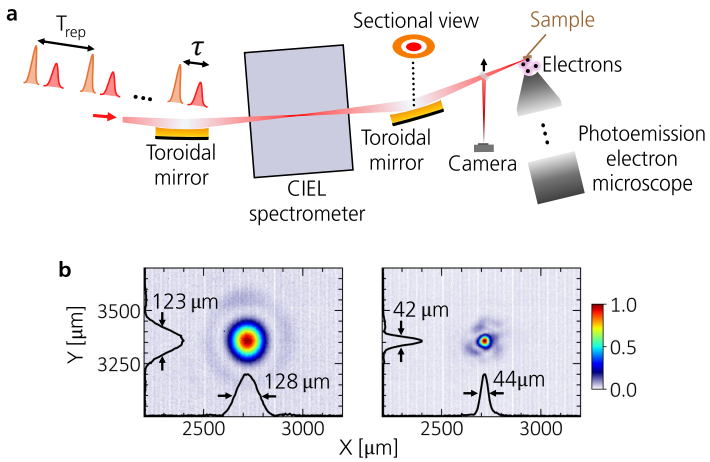

Figure 5.7: Time-resolved PEEM set-up. (a) Two replica of the NIR few-cycle pulses are refocused by a toroidal mirror on the sample in the PEEM. Their relative delay is controlled with an attosecond accuracy using the same pump-probe interferometer as used for LAP (see Fig. 4.8). (b) Beam profile of the pump (left) and the probe (right) at refocus.

In contrast to solids with larger dimensions, nanostructures locally enhance the electric field of the impinging light, leading to strong local fields. Accordingly, nonlinear photoemission, for example through the simultaneous absorption of several laser photons is easily enabled. In the perturbative multiphoton regime, the transition probability is then predicted to be directly proportional to the total electric field raised to the multiphoton order n. The photoelectron signal at a certain kinetic energy and delay is then given by the n-th order nonlinear interferometric autocorrelation function:

$$I_{\mathrm{PE}}(\tau, E) = \int dt |E_{\mathrm{loc.}}(t) + E_{\mathrm{loc.}}(t-\tau)|^{2n} \tag{5.4}$$

where $E_{\mathrm{loc.}}(t)$ and $E_{\mathrm{loc.}}(t-\tau)$ are the local electric fields induced by the pump and probe fields at the surface. Figure 5.8a computes this function for $n = 3$, and for the experimental electric field used in the experiments of **Paper VI**, retrieved with a d-scan (see inset). No field enhancement is included, such that $E_{\mathrm{loc.}}(t) = E_{\mathrm{L}}(t)$ and $E_{\mathrm{loc.}}(t-\tau) = rE_{\mathrm{L}}(t-\tau)$ with E_{L} being the most intense laser beam and $r = 0.5$ their relative ratio. In Fig. 5.8b, the total electric field is plotted for two different delays between the fields. The total fields differ mostly in strength.

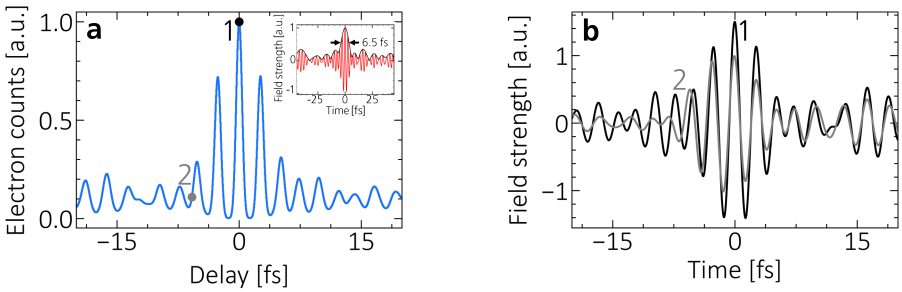

Figure 5.8: Cross-correlation electron signal. (a) Third order ($n = 3$) nonlinear interferometric autocorrelation function calculated for the experimental electric field shown in the inset. (b) Total electric field at -5.8 fs (gray) and 0 fs (black).

The long-term purpose of the beamline is to study LAP from nanostructures in a similar fashion than in atoms, using our short APTs as a pump and characterize them by operating the reaction microscope in parallel. Preliminary datasets were acquired on InP substrate and nanowires. A preliminary analysis shows that the samples were oxidized, which is unfortunate, and that photoelectrons emitted from the oxygen core levels overlapped with those emitted from the indium ones, leading to spectral congestion. This problem, which is largely absent in ATAS, is a major limitation of charged-particle detection schemes.

2 Experimental measurements of compound semiconductors

In this section, experimental measurements of electron dynamics in compound semiconductors are presented.

2.1 Compound semiconductors

Compound semiconductors are materials composed by two or more chemical elements. Since elements from different groups of the periodic table have different structural, optical or electronic properties, combining them provides additional features that are not available in single-element materials. In particular, they enable a wide spectral range of energy bandgaps and band structure. This is depicted in Fig. 5.9 for binary compounds of the group III-V (an element from group III and V) and IV-VI (an element from group IV and VI).

IV-VI semiconductors usually have small band gaps, making them suitable for mid-infrared optoelectronic devices. While many crystallize in a rock-salt structure (e.g. lead-based compounds), others crystallize in orthorombic phases such as SnS, SnSe, GeS and GeSe. In **Paper IV**, a recently synthesized metastable cubic phase of SnS, relevant to optoelectronic and energy-conversion applications, is investigated using ATAS.

III-V semiconductors are widely used in high-speed electronics and optoelectronics, due to a high electron mobility and strong optical absorption. Many possess direct bandgaps, that enable a more

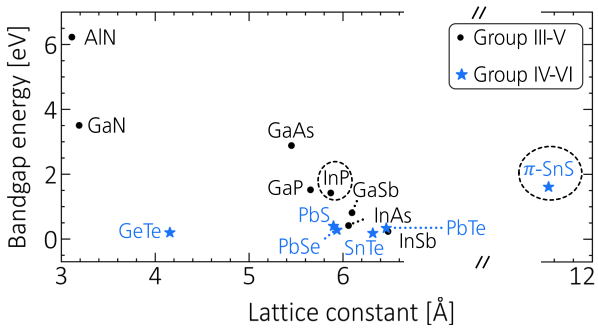

Figure 5.9: Bandgap map of binary III-V and IV-VI semiconductors. Bandgap energy as a function of the lattice constant for selected semiconductors of the group III-V (black) and IV-VI (blue). Data taken from [114, 115, 116, 117, 118, 119, 120, 121]. The compound semiconductors studied in this thesis are indicated by the dashed circles.

efficient radiative recombination compared to silicon. These materials can be synthesized as low-dimensional structures having nanoscale sizes in at least one-dimension. Typically, semiconductor nanowires can be grown via a gold (Au) metal seed thus forming metal-semiconductor hybrid structures, useful for a wide range of applications [122, 123, 124]. They adopt regular cylindrical shape. In **Paper V**, InP nanowires are studied as a structural platform for controlled photoemission.

2.2 Charged carrier dynamics in π-SnS

Many research works have been carried out on SnS thin film solar cells, owing to its strong visible-light absorption and abundance on Earth. However, its photovoltaic performance has remained low, primarily due to defects, impurities, and pronounced anisotropy [125, 126, 127]. In the last years, a metastable high-symmetry cubic phase (π-SnS) has been synthesized, with promising prospects for photovoltaic applications [128, 121]. In the following, the ATAS set-up introduced earlier (see Fig. 5.3) is used to study carrier relaxation dynamics in this material with high temporal resolution and elemental sensitivity, following the experiments of **Paper IV**.

The differential XUV absorbance [see Eq. (5.3)] of 30 nm π-SnS thin films is measured in Fig. 5.10a as a function of pump-probe delay and XUV photon energy across the Sn $N_{4,5}$ absorption edge. At positive delays, the laser pulse (pump) arrives before the XUV, thus photoexciting electrons in the conduction band (CB), as illustrated by the red arrow in Fig. 5.10b.

For delays above 0 ps, the XUV probes the pump-induced changes, leading to variations in the absorbance at 25.5 and 26.5 eV (see black dashed lines). These energies match with core-level transitions from the Sn $4d_{5/2}$ and $4d_{3/2}$ spin–orbit-split states to the conduction band minimum (CBM) [129, 130, 131], indicated by dark blue arrows in Fig. 5.10b. Specifically, the differential absorbance decreases (increases) just above (below) the absorption edge for both spin–orbit components. The increase in absorption arises from pump-induced state filling in the CB, while the decrease in absorption arises from a depletion of available states in the VB (state blocking).

Figure 5.11 presents the differential absorbance averaged over short (0–100 fs) and long (1–3 ps) delays. The onset of the absorption edge has shifted at longer times, which is due to the interplay

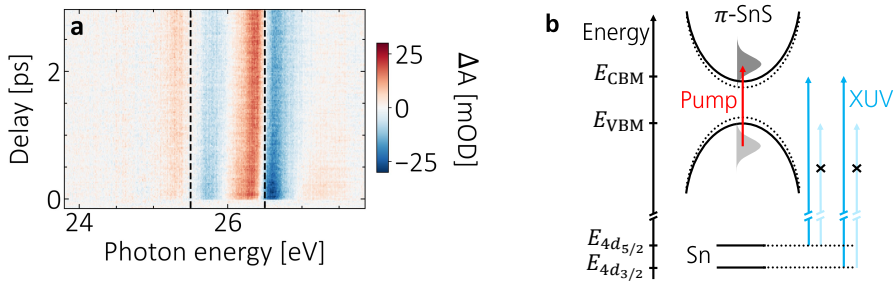

Figure 5.10: ATAS measurement of π-SnS. (a) Differential XUV absorbance of π-SnS as a function of pump-probe delay and XUV photon energy. (b) Simplified energy diagram of π-SnS with the XUV (blue arrows) and pump (red arrow) transitions. The dark (light) gray Gaussian areas represent the photoexcited electrons (holes). The solid (dotted) parabolas represent the valence and conduction bands with (without) bandgap renormalization. Adapted from **Paper IV**.

of electronic and structural effects. On the one hand, state filling increases the energy onset of the absorption edge in time by occupying states while many-body interactions among carriers lead to a redshift that reduce the bandgap, called bandgap renormalization (see dotted lines in Fig. 5.10b) [132, 133]. Finally, pump-induced lattice motions may also shift the core-level potential energy. In addition to the energy shift, the signal amplitude varies with time. It is larger at early times, in which case it is dominated by hot carriers. At later times, the system relaxes toward equilibrium through cooling of the CB electrons and their subsequent recombination with the VB holes.

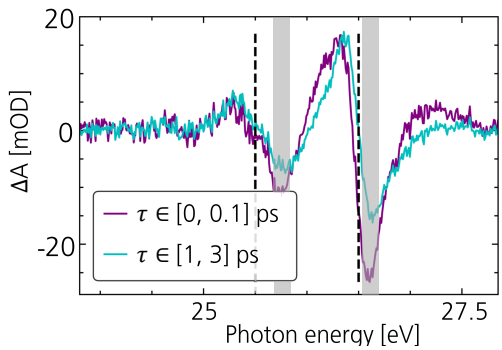

Figure 5.11: Differential XUV absorbance at short and long delays. Differential XUV absorbance across the Sn $N_{4,5}$ absorption edge as a function of the XUV photon energy. The purple and blue curves show averages over pump-probe delays between 0 and 100 fs and between 1 and 3 ps, respectively. Adapted from **Paper IV**.

The measurement was repeated for carrier densities ranging from 1.6×10^{19} to 3.1×10^{20} electrons/cm^{-3}, corresponding to 0.04% to 0.775% of the equilibrium valence band population. It is possible to assume that electron dynamics can be decomposed into a fast intraband cooling followed by a slower hole-electron recombination. Therefore, the signal is averaged over the energy window indicated by

gray shaded area in Fig. 5.11 for each measurement and fitted to a bi-exponential Gaussian function:

$$\Delta A_{CB}(\tau) = \big(\underbrace{1 - e^{-\Gamma_r \tau}}_{\text{rise}}\big)\big(\overbrace{A_f e^{-\Gamma_f \tau}}^{\text{“carrier cooling”}} + \underbrace{A_s e^{-\Gamma_s \tau}}_{\text{“carrier recombination”}}\big), \tag{5.5}$$

where Γ_r describes the rise of the signal, Γ_f the fast decay rate and Γ_s the slow decay rate, with associated amplitudes A_f and A_s, respectively.

The fast decay rate, shown in Fig 5.12a, provides information about carrier cooling [134]. Two regimes are observed depending on the carrier density: a slowly varying rate below 1.6×10^{20} electrons/cm^{-3} (pink area) and an increasing rate above (blue area). Analysis using a two-temperature model in **Paper IV** indicates that cooling is non-radiative in both regimes. At low densities, it is primarily governed by the ability of the system to absorb heat, leading to intraband relaxation toward the band edges, as illustrated schematically in Fig. 5.13 (label 1, left). At higher densities, many-body interactions between carriers, referred to as Auger processes, enable an additional cooling channel, where CB electrons transfer their energy to holes in the VB via Coulomb scattering, see label 1 on the right of Fig. 5.13.

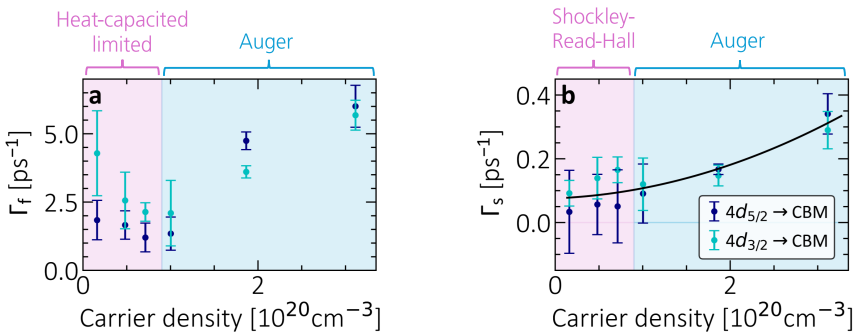

Figure 5.12: **Decay rates in π-SnS.** Decay rates extracted from a bi-exponential fit as a function of the carrier density. Blue and cyan colors correspond to the $4d_{5/2}$ (at 25.5 eV) and $4d_{3/2}$ (at 26.5 eV) state filling window. The error bars indicate one standard deviation. (a) Fast decay rate, corresponding to cooling. (b) Slow decay rate, corresponding to recombination. The solid curve shows a fit to a polynomial rate equation. Adapted from **Paper IV**.

The fitted slow decay rate, shown in Fig. 5.12b, is used to study carrier recombination mechanisms [135]. Its density dependence is described by a polynomial rate equation including multiple recombination channels. By fitting the slow rates to this equation (black solid line), two dominant mechanisms are identified: Shockly-Read-Hall (SRH) at low densities and Auger-recombination at high densities. These recombination pathways are shown in Fig. 5.13 (label 2). In SRH, intermediate discrete energy states arising in the forbidden bandgap due to impurities and defects trap carriers, leading to non-radiative recombination. In the Auger process, the recombination energy is non-radiatively transferred to a third carrier. The onset of Auger-recombination from a density of 1.6×10^{20} electrons/cm^{-3} coincides with the onset of Auger-cooling, indicating that it is the threshold density for many-body effects in π-SnS. These non-radiative processes are major limiting factors in the efficiency of thin film photovoltaic cells, since they dissipate energy as heat rather than generating a photocurrent. This makes π-SnS an ideal platform to investigate loss mechanisms in solar cells.

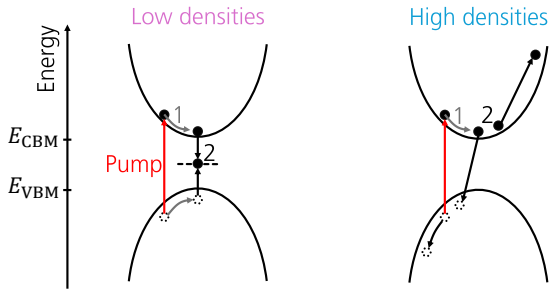

Figure 5.13: **Cooling and recombination mechanisms in π-SnS.** Following photo-excitation by the pump (red arrow), the hot electron and hole distributions undergo cooling (1) before recombining (2). At low densities (left), fast intraband cooling toward the band edges occurs, followed by Shockly-Read-Hall recombination mediated by defects or impurities in the forbidden bandgap. At high densities (right), Auger cooling and recombination takes place, which involves energy exchange between at least three carriers. Adapted from **Paper IV**.

This investigation of electron dynamics in π-SnS was motivated by the higher symmetry compared to its natural orthorombic phase. In particular, many structural properties relevant to photovoltaic applications (e.g. thermal ones) are governed by collective lattice vibrations known as phonons. In some of the measurements, coherent phonon oscillations excited by the pump laser could be resolved. While several phonon properties could be extracted (period, dephasing time or phase), it was not possible to unambiguously assign the phonon mode due to the primitive cell of π-SnS being large, with 64 atoms yielding 192 vibrational modes [121, 120, 128, 136]. However, comparing phonon oscillations in π-SnS with the ones in its orthorhombic phase could unravel the role of structural symmetry, and may help assess the potential of π-SnS for photovoltaic applications. An interesting follow-up experiment would thus consist in measuring both phases under similar conditions and compare their phonon dynamics.

2.3 Controlled ultrafast photoemission from InP nanowires in locally enhanced fields

In light-matter interactions, photoemission is conveniently described by the Keldysh parameter, given by $\gamma = \sqrt{\Phi/(2U_p)}$ with Φ being the material work function [137, 138]. At relatively weak field strengths ($\gamma > 1$), multiphoton emission arises, in which the electron absorbs several photons n. The photoemission probability decreases when the number of exchanged photons increases. For large field strengths ($\gamma < 1$), the electron can escape through tunneling due to field-induced distortions of the atomic potential. In this case, the electron can acquire energy in the electric field of the light and even rescatter at the surface, thereby reaching high energies. The photoelectron spectra exhibit a broad energy plateau (constant electron yield with energy), followed by a slowly decreasing cut-off.

Recent studies of photoemission from metallic nanostructures induced by few-cycle IR pulses demonstrated their potential as ultrafast, spatially localized electron sources supporting sub-femtosecond durations -down to the attosecond regime [139, 140, 58]. These remarkable properties arise from the underlying nonlinear light-matter interaction, in which the nanostructure plays a major role by its capability to locally enhance the electric field and enable strong-field tunneling even for moderate

laser intensities [139, 140, 58, 141, 142, 143]. In **Paper V**, photoemission from semiconductor InP nanowires, which have comparatively received little attention, is studied since their structure should lead to field enhancement as well.

Figure 5.14a schematically illustrates the principle of the experiment, performed with the previously described set-up (see Fig. 5.7). Due to local field enhancement, the interaction between the incident far-field laser (in red) and an InP nanowire leads to photoelectron sources spatially localized at the wire's edges (in purple). This can be shown by simulating the electric field distribution in the vicinity of the wire. For this, the wire is modeled as a cylinder of 2.65 µm length and 0.2 µm height with a gold seed at its tip, in accordance with the geometrical features extracted from the Scanning Electron Microscopy image shown in Fig. 5.14b. Maxwell equations are then solved with Finite-Difference Time-Domain simulations [144]. Figure 5.14c shows the electric field distribution resulting from the interaction with a 6 fs Gaussian pulse normalized at 1 V/m. The field is enhanced at the corners of the wire up to twice its value, see for example the red rectangular area.

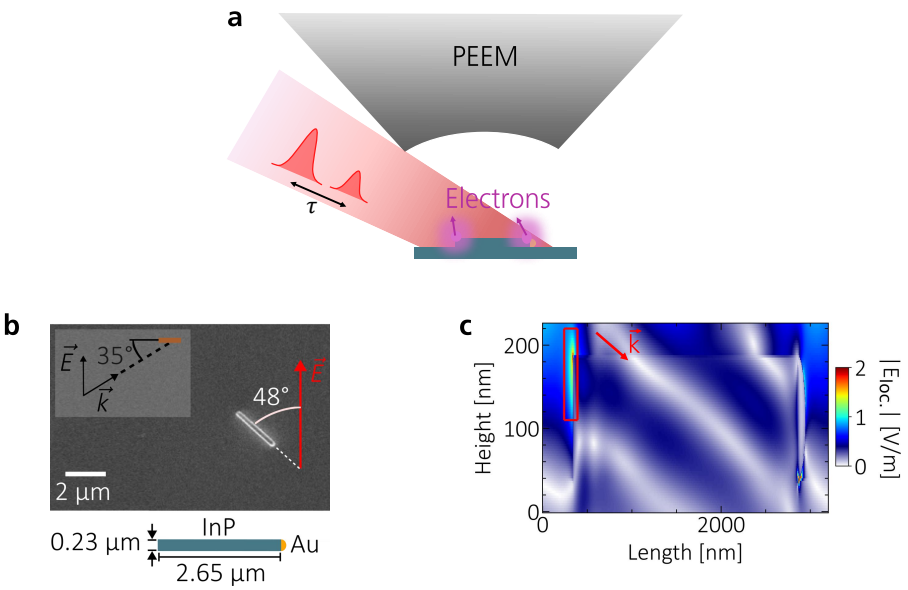

Figure 5.14: Field-enhanced photoemission from InP nanowires. (a) Two delayed replica of a NIR laser (in red) impinge on an InP nanowire. The nanostructure enhances the field, leading to localized photoemission at its edges. The photoelectrons (in purple) reach the PEEM extractor, where their energy is recorded. (b) Scanning Electron Microscopy image of a measured isolated wire. The red arrow indicates the orientation of the electric field with respect to the nanowire longitudinal axis. Inset: angle of incidence and field polarization direction relative to the nanowire on the sample (top view). (c) Finite-Difference Time-Domain simulations of the local field $E_{\mathrm{loc.}}$ distribution. The red arrow indicates the propagation direction of the field.

In this experiment, the intensity of the total field at the optimum overlap is about a few 10^{11} W/cm^2. By considering the work function of InP [145], this should place the experiment in the multiphoton regime ($\gamma \sim 7 \gg 1$). However, the local Keldysh parameter is considerably different in the regions where the electric field is enhanced, such that the semiconductor nanostructure can lead to a change of photoemission regime, where strong-field effects become important. Local-field enhancement is therefore a powerful benefit when studying photoemission in strong fields, as it removes the need to use considerably higher intensities, which in general damage the samples.

Figure 5.15a shows the spectrally-resolved cross-correlation measurement, that is the electron counts as a function of delay between the fields and electron kinetic energy. Electrons are emitted with a periodicity of 2.8 fs, corresponding to the laser period, such that the electron emission closely follows the electric field of the light.

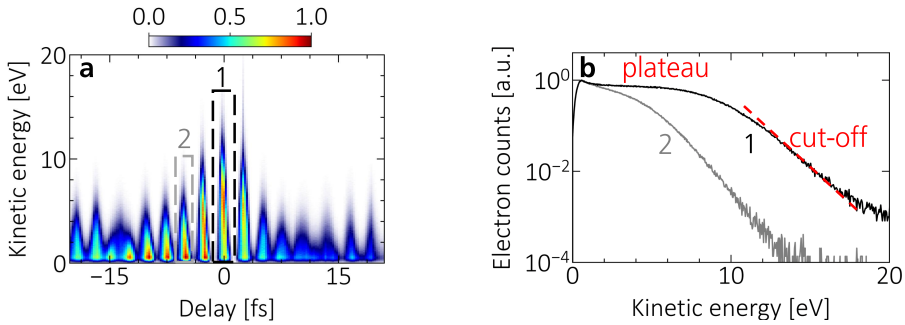

Figure 5.15: Properties of photoelectrons. (a) Electron counts (in color) as a function of the kinetic energy and pump-probe delay. (b) Electron energy spectra obtained after a delay average in the optical cycle indicated by the (1) gray and (2) black dashed lines in (a). The spectrum corresponding to the optical cycle with highest field strength exhibits a broad plateau, followed by a slowly decreasing cut-off (red dashed line)

By varying the delay, hence the strength of the total field, the energy spectrum changes. The highest kinetic energies are produced at 0 fs, when the total field is strongest. The average energy spectrum of electrons emitted around this delay, taken in the range indicated by the black dashed rectangle, is shown in Fig. 5.15b in logarithmic scale. The electron counts are constant over a broad energy range until a cut-off at approximately 14 eV. This plateau-like feature is characteristic of strong-field photoemission regime, suggesting that the local field enhancement could enable tunneling. A remarkable property of the photoelectrons is the broad energy bandwidth, which is compatible with sub-femtosecond durations (several hundreds of attoseconds). In gray, the energy spectrum averaged between -6.1 and -3.5 fs (gray area in Fig. 5.15a) is plotted. Since this delay corresponds to comparatively small intensity, the cut-off energy is lower. We note that even larger energy bandwidths were produced in some measurements, however, space charge effects then impacted the results, precluding thorough analysis.

In addition, the delay stabilization system which provides ∼26 as precision (see previous chapter) enables resolving a tilt of the kinetic energy with delay within each period. In particular, higher energies seem to be emitted first. This tilt, which could be reproduced by measuring other InP wires, is unexpected since the electron yield should vary symmetrically in time around an oscillation maximum (see Fig. 5.8a). These features currently remain under investigation. Theoretical collaborations with the group of Claudio Verdozzi in the Mathematical Physics divion of Lund University are ongoing. More precisely, a microscopic approach combining ab initio calculations and quantum many-body methods is employed. A low-energy Hamiltonian is derived from density functional theory using maximally localized Wannier functions in a minimal sp^3 basis and used in nonequilibrium Green's function simulations of electron dynamics under pump–probe fields.

CHAPTER 6

Conclusion

1 Summary of the thesis

In this thesis, we explored the potential of short APTs in advancing the field of ultrafast science and related applications. The work focused on both the development of the source and its application to laser-assisted photoionization in helium, used as a benchmark system, as well as to charge carrier dynamics in solids. The key findings of this work point to several interesting phenomena. In particular, the use of few-cycle driving pulses allowed us to observe subcycle phase-matching effects in high-order harmonic generation. In addition, the broad spectral bandwidth of the pulses led to the appearance of new quantum interference in photoionization measurements.

More specifically, regarding high-order harmonic generation, we thoroughly characterized the complex spectral and temporal structure of the APTs. To this end, LAP was used to measure short APTs for different driving laser CEP values (**Paper II**). The results showed that both microscopic and macroscopic effects play an important role in the energy-dependent number of attosecond pulses in the train. In particular, evidence of confinement of the harmonic emission, attributed to subcycle phase matching, was observed. Further confinement of the XUV emission is of interest for the production of single attosecond pulses (SAPs). To address this, a method based on driving HHG with polarization-gated few-cycle pulses (**Paper I**) was implemented. The HHG yield as a function of the CEP exhibited features consistent with a temporal confinement of the XUV emission approaching the SAP regime. Hence, the implementation of polarization gating provides additional control over the generated attosecond pulses and makes the source more flexible for future applications.

Applications concerning ultrafast spectroscopy of atoms and solids were then carried out. Two studies focused on short-pulse effects in photoionization of helium by a comb of broad harmonics in

the presence of a few-cycle dressing laser field (**Papers III and VI**). **Paper III** investigated broadband effects in photoionization and found that the large spectral widths give rise to four types of interference involving quantum paths of different parities. While this adds complexity, we showed that the pathways can be distinguished, thus providing four new observables with their own properties. In **Paper VI**, interference between broadband electron wavepackets involving non-resonant and resonant quantum paths were studied. The phase and amplitude of the interference pattern were found to be influenced by the complex spectral properties of the light fields. In this study, we develop an efficient numerical methodology to retrieve information without prior knowledge of the light fields, thus circumventing the downsides of using ultrashort pulses while emphasizing their advantages.

Paper IV focused on ATAS measurements, which rely on ultrashort attosecond pulses, close to SAPs. The purpose was to investigate charge carrier dynamics in a metastable cubic phase of SnS. This technique proved to be very powerful to investigate conduction-band related dynamics, particularly relevant to photovoltaic applications. It brought insights about non-radiative carrier cooling and recombination mechanisms, which are limiting factors for the efficiency of thin film solar cells.

Finally, the few-cycle laser pulses themselves were used for studying photoemission from semiconductor nanostructures (**Paper VI**). InP nanowires are ideal sources of ultrashort and spatially localized electrons, having energy bandwidths compatible with sub-femtosecond durations.

2 Outlooks

This thesis explored several applications, for which we foresee follow-up studies. Those mainly build on the experimental set-ups developed during this thesis and on the properties of the short APTs.

2.1 Toward new attosecond metrology tools for probing matter

The set-up developed in **Paper I** for manipulating the time-dependent polarization of the few-cycle laser pulses offers many possibilities to control the short APTs, beyond the simple polarization-gating. For example, it enables the creation of two cross-polarized attosecond pulses with a controllable delay. Figure 6.1 shows the PAD of electrons produced through ionization of helium by two short APTs, linearly polarized along $\mathbf{x}$ and $\mathbf{z}$. In this scheme, the dipole selection rules are altered, now allowing electronic transitions with $\Delta m = \pm 1$ in addition to those with $\Delta m = 0$. This is depicted in Fig. 6.1d, which shows the available one-photon energy transitions from ground state helium.

Since photoelectrons with various magnetic quantum numbers, associated to spherical harmonics of different phases ($Y_{lm} \propto e^{im\phi}$) and angular properties, contribute to the PAD, the azimuthal symmetry along the detector axis ($\mathbf{z}$) is broken. This is shown in Fig. 6.1c, where the PAD projected along $\mathbf{x}$ behaves like that of a p-wave oriented at 45° with respect to the $\mathbf{y}$ and $\mathbf{z}$ axes. Information about the quantum channels of different m are therefore encoded in the angular and radial coordinates, when a single such channel ($m = 0$) was accessible in helium using only linearly polarized light.

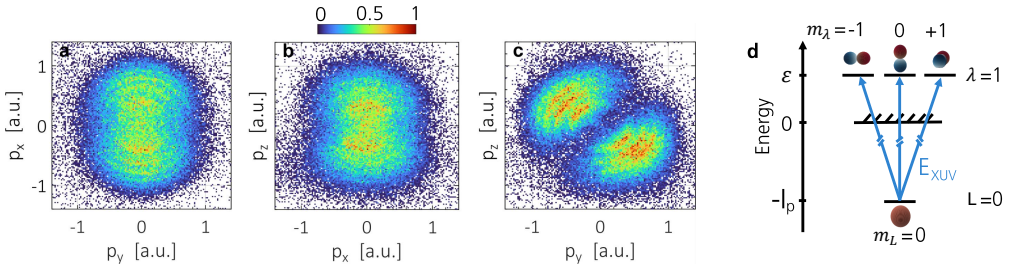

Figure 6.1: **Measured photoelectron angular distribution for two delayed cross-polarized APTs**. (a-c) Two-dimensional projection of the momentum of electrons ionized by cross-polarized APTs separated by 0 fs. $\mathbf{z}$ is the axis of the detector. The APTs are linearly polarized along $\mathbf{x}$ and $\mathbf{z}$. (d) Channels involved in the XUV-induced one-photon ionization of ground state helium.

Furthermore, as the delay between the attosecond pulses can be controlled, phenomena analogous to spectral interferences between electron wavepackets are expected. We aim to use it to investigate electron wave packet dynamics, while adding control over the light polarization, since the visibility of interference fringes from two sources is an indicator of their mutual coherence. This principle has recently been applied, by measuring ions, to study the interplay between entanglement and coherence in the photoionization of hydrogen molecules [24].

We are currently developing methods to determine the contributions of the different magnetic quantum numbers, and a first application using the electron spectrometer to perform polarimetry of the light has been achieved. Beyond resolving partial waves with different m, this could allow probing symmetry in matter, since several systems behave differently depending on the XUV polarization (e.g. chiral molecules) [11, 146].

2.2 Toward quantum state tomography in LAP

In this thesis, effects arising from the complex light field properties, in particular their broad bandwidths, were investigated in the context of LAP measurements. Notably, **Paper VI** successfully exploited these short-pulse effects to retrieve the relative amplitudes and phases of highly excited states. Future research directions therefore point toward the implementation of quantum state tomography protocols [19, 20], which are methods that consist in reconstructing the full quantum state of a system, that would exploit short-pulse effects.

In particular, it was found in Chapter 4 that using short APTs leads to interference between quantum paths of same parity that are not observed in traditional RABBIT schemes, most notably at low frequencies ($\omega < 0.4\omega_0$), for example in Fig. 4.20. Here, the broadband IR creates a coherent superposition between different parts of the EWP produced by XUV-induced one-photon transitions. More precisely, two IR probe photons with frequency ω_1 and $\omega_2 = \omega_1 + \delta\omega$ ($\delta\omega$ is a small detuning) create quantum interference between two different intermediate states. By varying the delay of the IR probe field, oscillations at $\delta\omega = \omega_1 - \omega_2$ arise which amplitude and phase depend on the coherence between the two different energies of the one-photon EWP. In other words, the possibility to encode information about the off-diagonal elements of the density matrix exists, with many resemblance to an already existing quantum state tomography protocol called KRAKEN

(Kvanttillstånds tomogRafi av AttoseKund ElektroNvågpaket) [20]. It would therefore be of very high interest to explore these interference structures further.

2.3 PEEM-related outlooks

Finally, measurements with the PEEM were also performed on InP using short APTs. However, the samples were not uniform and presented oxydation layers, thus leading to overlap between electrons from oxygen and from indium, which made the interpretation more difficult. While it shows that PEEM can be sensitive to elemental structure (like oxidation), it also puts forwards its limitations. ATAS can be a more appropriate method for such studies. It could, however, be valuable to repeat the experiment on a sample with better quality.

In connection with the photoemission experiments performed in **Paper V**, CEP-dependent studies of the electron yield could be of very high interest, since strong-field effects often depend on this parameter as seen throughout this thesis or in measurements on metallic nanotips [58].

Appendix A

Chapter 4 discussed the expansion of the PAD in Legendre polynomials, and proposed a method to extract the continuum-continuum phase differences and amplitude ratios between different scattering channels from the odd coefficients (h_1 and h_3). This appendix demonstrates that extracting these quantities using even coefficients (h_0, h_2 and h_4) does not converge to a unique solution in helium, preventing an unambiguous characterization of the photoionization process.

A.1 Expansion of photoelectron angular distribution

For two-photon ionization of helium by long pulses, the PAD can be expressed as

$$S_{\mathrm{SB}}(\tau,\theta) = h_0(\tau)P_0^0[\cos(\theta)] + h_2(\tau)P_2^0[\cos(\theta)] + h_4(\tau)P_4^0[\cos(\theta)]. \tag{1}$$

According to TDPT, the same quantity can be written in terms of partial waves:

$$\begin{aligned} S_{\mathrm{SB}}(\tau,\theta) = 4\pi^2\big|&a_{010}^{(2,+)}(\tau)Y_{00}(\theta) + a_{010}^{(2,-)}(\tau)Y_{00}(\theta) \\ &+ a_{210}^{(2,+)}(\tau)Y_{20}(\theta) + a_{210}^{(2,-)}(\tau)Y_{20}(\theta)\big|^2. \end{aligned} \tag{2}$$

The $4\pi^2$ factor accounts for the integration over the azimuthal angle, since the magnetic quantum number is zero in helium and linearly polarized fields are used. Expanding this equation produces terms proportional to $(Y_{\ell 0})^2$ or $Y_{\ell 0}Y_{\ell' 0}$ ($\ell \neq \ell'$), which can be linearized using Eq. (4.4):

$$Y_{00}^2 = \frac{1}{4\pi}P_0^0, \tag{3}$$

$$Y_{20}^2 = \frac{1}{4\pi}\left(\frac{18}{7}P_4^0 + \frac{10}{7}P_2^0 + P_0^0\right), \tag{4}$$

$$Y_{00}Y_{20} = \frac{1}{4\pi}\sqrt{5}P_2^0. \tag{5}$$

By comparing Eq. (1) with the linearized Eq. (2), explicit expressions for the coefficients h_n can be found.

At a given energy in a sideband, the even coefficients are given by:

$$\begin{aligned} h_0(\tau) =& |a_{010}^{(2,+)}|^2 + |a_{010}^{(2,-)}|^2 + |a_{210}^{(2,+)}|^2 + |a_{210}^{(2,-)}|^2 \\ &+ 2|a_{010}^{(2,+)}||a_{010}^{(2,-)}| \cos\left[2\omega\tau + \left(\varphi_{010}^{+} - \varphi_{010}^{-}\right)\right] \\ &+ 2|a_{210}^{(2,+)}||a_{210}^{(2,-)}| \cos\left[2\omega\tau + \left(\varphi_{210}^{+} - \varphi_{210}^{-}\right)\right], \end{aligned} \tag{6}$$

$$\begin{aligned} h_2(\tau) =& \frac{10}{7}\Bigg\{ |a_{210}^{(2,+)}|^2 + |a_{210}^{(2,-)}|^2 \\ &+ 2|a_{210}^{(2,+)}||a_{210}^{(2,-)}| \cos\left[2\omega\tau + \left(\varphi_{210}^{+} - \varphi_{210}^{-}\right)\right] \Bigg\} \\ &+ 2\sqrt{5}\Bigg\{ |a_{010}^{(2,+)}||a_{210}^{(2,+)}| \cos\left[\varphi_{010}^{+} - \varphi_{210}^{+}\right] \\ &+ |a_{010}^{(2,-)}||a_{210}^{(2,-)}| \cos\left[\varphi_{010}^{-} - \varphi_{210}^{-}\right] \\ &+ |a_{010}^{(2,+)}||a_{210}^{(2,-)}| \cos\left[2\omega\tau + \left(\varphi_{010}^{+} - \varphi_{210}^{-}\right)\right] \\ &+ |a_{010}^{(2,-)}||a_{210}^{(2,+)}| \cos\left[2\omega\tau + \left(\varphi_{210}^{+} - \varphi_{010}^{-}\right)\right] \Bigg\}, \end{aligned} \tag{7}$$

$$\begin{aligned} h_4(\tau) =& \frac{18}{7}\Bigg\{ |a_{210}^{(2,+)}|^2 + |a_{210}^{(2,-)}|^2 \\ &+ 2|a_{210}^{(2,+)}||a_{210}^{(2,-)}| \cos\left[2\omega\tau + \left(\varphi_{210}^{+} - \varphi_{210}^{-}\right)\right] \Bigg\}. \end{aligned} \tag{8}$$

Here, the two-photon phase $\varphi_{\ell 10}^{\pm}(\Omega) = \phi_{\mathrm{XUV}}(\Omega_{\mp}) + \eta_{10}(\Omega_{\mp}) + \phi_{\mathrm{cc},\ell 1}^{\pm}(\Omega) + \varphi_{\mathrm{CEP}}$ is introduced with $\Omega_{\mp} = \Omega \mp \omega$ and Ω being the intermediate and final state frequencies.

A.2 Global fit on the even coefficients

Notably, the even weights contain only cosine terms of phase differences and are invariant under simultaneous exchange of the $\ell = 0$ and $\ell = 2$ contributions:

$$\begin{aligned} &\varphi_{010}^{+} \leftrightarrow \varphi_{210}^{+}, \qquad && |M_{010}^{+}| \leftrightarrow |M_{210}^{+}|, \\ &\varphi_{010}^{-} \leftrightarrow \varphi_{210}^{-}, \qquad && |M_{010}^{-}| \leftrightarrow |M_{210}^{-}|. \end{aligned} \tag{9}$$

This invariance property implies that the system of equations h_0, h_2, h_4 possesses two distinct solutions. Since only the continuum-continuum phases are different between $\varphi_{010}^{\pm}$ and $\varphi_{210}^{\pm}$, it is straightforward to understand the substitutions given in Eq. (4.23) of Chapter 4. As a consequence, simultaneously fitting the two-photon amplitudes and phases to obtain $\varphi_{010}^{\pm} - \varphi_{210}^{\pm} = \phi_{\mathrm{cc},01}^{\pm} - \phi_{\mathrm{cc},21}^{\pm}$ and $|M_{010}^{(2,\pm)}|/|M_{210}^{(2,\pm)}|$ gives rise to two sets of solutions.

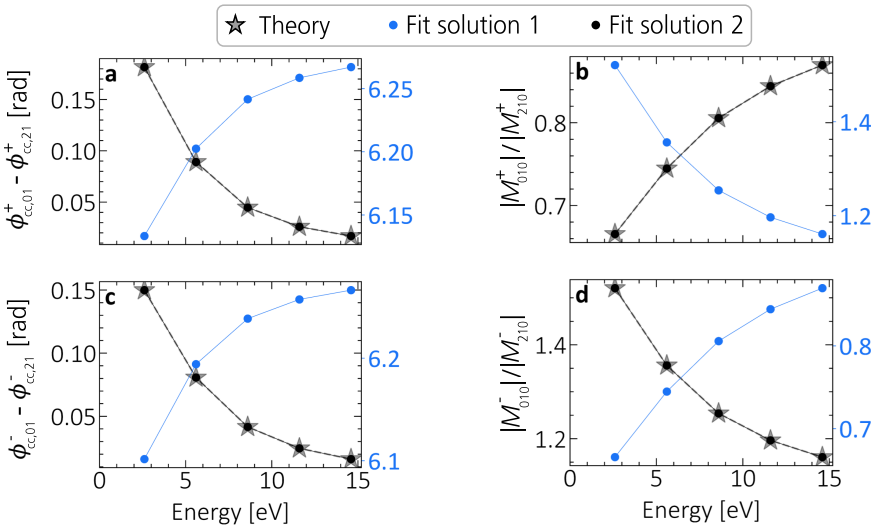

Figure 2: **Extraction of continuum-continuum phases and radial scattering channel amplitude ratios from even Legendre coefficients.** Results of a global fit on the even h_n (black and blue dots) for datasets generated with ab initio data taken from [107], indicated by gray stars. (a,c) Difference of continuum-continuum phases for the absorption and emission of an IR photon. (b,d) Ratio of scattering channel radial matrix element amplitudes for the absorption and emission of an IR photon. The blue and black dots are two fit results that yield similar accuracy. Only the solution in black is physical.

In Fig. 2, star-like symbols show the theoretical continuum-continuum phase differences and amplitude ratios taken from [107], for either the (a,b) absorption or (c,d) emission of an IR photon. The theoretical values are used to calculate h_0, h_2 and h_4, which are then simultaneously fitted using equations (6), (7) and (8). The fitted parameters are: $|M_{010}^{(2,+)}|$, $|M_{010}^{(2,-)}|$, $|M_{210}^{(2,+)}|$, $|M_{210}^{(2,-)}|$, φ_{010}^{+}, φ_{010}^{-}, φ_{210}^{+} and φ_{210}^{-}. The fit is repeated for $N = 1000$ sets of initial conditions. It is found that two sets of solutions typically give excellent fit results, which are indicated by blue and black dots on the figure. To converge toward the physical solution prior knowledge is needed, for example of Fano propensity rules [105]. This highlights the potential of broadband effects, which enable using the odd Legendre polynomials and thus circumvent such convergence issues.

References

[1] H. Hertz. Ueber einen einfluss des ultravioletten lichtes auf die electrische entladung. *Annalen der Physik*, 267(8):983–1000, 6 1887.

[2] A. Einstein. Über einen die erzeugung und verwandlung des lichtes betreffenden heuristischen gesichtspunkt. *Annalen der Physik*, 322(6):132–148, 3 1905.

[3] A. H. Zewail. Femtochemistry: atomic-scale dynamics of the chemical bond. *J. Phys. Chem. A*, 104(24):5660–5694, 5 2000.

[4] A. McPherson, G. Gibson, H. Jara, U. Johann, T. S. Luk, I. A. McIntyre, K. Boyer, and C. K. Rhodes. Studies of multiphoton production of vacuum-ultraviolet radiation in the rare gases. *J. Opt. Soc. Am. B*, 4(4):595–601, 4 1987.

[5] M. Ferray, A. L'Huillier, X. F. Li, L. A. Lompre, G. Mainfray, and C. Manus. Multiple-harmonic conversion of 1064 nm radiation in rare gases. *J. Phys. B: Atom. Mol. Opt. Phys.*, 21(3):L31, 2 1988.

[6] K. Klünder, J. M. Dahlström, M. Gisselbrecht, T. Fordell, M. Swoboda, D. Guénot, P. Johnsson, J. Caillat, J. Mauritsson, A. Maquet, R. Taïeb, and A. L'Huillier. Probing single-photon ionization on the attosecond time scale. *Phys. Rev. Lett.*, 106(14):143002, 4 2011.

[7] E. P. Månsson, D. Guénot, C. L. Arnold, D. Kroon, S. Kasper, J. M. Dahlström, E. Lindroth, A. S. Kheifets, A. L'Huillier, S. L. Sorensen, and M. Gisselbrecht. Double ionization probed on the attosecond timescale. *Nat. Phys.*, 10(3):207–211, 3 2014.

[8] S. Heuser, Á. Jiménez Galán, C. Cirelli, C. Marante, M. Sabbar, R. Boge, M. Lucchini, L. Gallmann, I. Ivanov, A. S. Kheifets, J. M. Dahlström, E. Lindroth, L. Argenti, F. Martín, and U. Keller. Angular dependence of photoemission time delay in helium. *Phys. Rev. A*, 94(6):063409, 12 2016.

[9] V. Gruson, L. Barreau, Á. Jiménez-Galan, F. Risoud, J. Caillat, A. Maquet, B. Carré, F. Lepetit, J-F. Hergott, T. Ruchon, L. Argenti, R. Taïeb, F. Martín, and P. Salières. Attosecond dynamics through a fano resonance: Monitoring the birth of a photoelectron. *Science*, 354(6313):734–738, 11 2016.

[10] M. Huppert, I. Jordan, D. Baykusheva, A. von Conta, and H. J. Wörner. Attosecond delays in molecular photoionization. *Phys. Rev. Lett.*, 117(9):093001, 8 2016.

[11] S. Beaulieu, A. Comby, A. Clergerie, J. Caillat, D. Descamps, N. Dudovich, B. Fabre, R. Géneaux, F. Légaré, S. Petit, B. Pons, G. Porat, T. Ruchon, R. Taïeb, V. Blanchet, and Y. Mairesse. Attosecond-resolved photoionization of chiral molecules. *Science*, 358(6368):1288–1294, 12 2017.

[12] S. Nandi, E. Plésiat, S. Zhong, A. Palacios, D. Busto, M. Isinger, L. Neoričić, C. L. Arnold, R. J. Squibb, R. Feifel, P. Decleva, A. L'Huillier, F. Martín, and M. Gisselbrecht. Attosecond timing of electron emission from a molecular shape resonance. *Sci. Adv.*, 6(31):eaba7762, 7 2020.

[13] R. Locher, L. Castiglioni, M. Lucchini, M. Greif, L. Gallmann, J. Osterwalder, M. Hengsberger, and U. Keller. Energy-dependent photoemission delays from noble metal surfaces by attosecond interferometry. *Optica*, 2(5):405–410, 5 2015.

[14] L. Kasmi, M. Lucchini, L. Castiglioni, P. Kliuiev, J. Osterwalder, M. Hengsberger, L. Gallmann, P. Krüger, and U. Keller. Effective mass effect in attosecond electron transport. *Optica*, 4(12):1492–1497, 12 2017.

[15] A. Moulet, J. B. Bertrand, T. Klostermann, A. Guggenmos, N. Karpowicz, and E. Goulielmakis. Soft x-ray excitonics. *Science*, 357(6356):1134–1138, 9 2017.

[16] R. Géneaux, C. J. Kaplan, L. Yue, A. D. Ross, J. E. Bækhøj, P. M. Kraus, H-T. Chang, A. Guggenmos, M-Y. Huang, M. Zürch, K. J. Schafer, D. M. Neumark, M. B. Gaarde, and S. R. Leone. Attosecond time-domain measurement of core-level-exciton decay in magnesium oxide. *Phys. Rev. Lett.*, 124(20):207401, 5 2020.

[17] M. Lucchini, S.A. Sato, G. D. Lucarelli, B. Moio, G. Inzani, R. Borrego-Varillas, F. Frassetto, L. Poletto, H. Hübener, U. De Giovannini, A. Rubio, and M. Nisoli. Unravelling the intertwined atomic and bulk nature of localised excitons by attosecond spectroscopy. *Nat. Commun.*, 12(1):1021, 2 2021.

[18] R. Quintero-Bermudez and S. R. Leone. Deciphering core-exciton dynamics in CaF_2 with attosecond spectroscopy. *Phys. Rev. B*, 109(2):024308, 1 2024.

[19] C. Bourassin-Bouchet, L. Barreau, V. Gruson, J-F. Hergott, F. Quéré, P. Salières, and T. Ruchon. Quantifying decoherence in attosecond metrology. *Phys. Rev. X*, 10(3):031048, 8 2020.

[20] H. Laurell, S. Luo, R. Weissenbilder, M. Ammitzböll, S. Ahmed, H. Söderberg, C. L. M. Petersson, V. Poulain, C. Guo, C. Dittel, D. Finkelstein-Shapiro, R. J. Squibb, R. Feifel, M. Gisselbrecht, C. L. Arnold, A. Buchleitner, E. Lindroth, A. Frisk Kockum, A. L'Huillier, and D. Busto. Measuring the quantum state of photoelectrons. *Nat. Photon.*, 19(4):352–357, 4 2025.

[21] M. Berkane, R. Taïeb, G. Granveau, P. Salières, C. Bourassin-Bouchet, C. Lévêque, and J. Caillat. Complete retrieval of attosecond photoelectron dynamics from partially coherent states in entangled photoemission. *Phys. Rev. A*, 111(4):L041101, 4 2025.

[22] W. Jiang, G. S. J. Armstrong, J. Tong, Y. Xu, Z. Zuo, J. Qiang, P. Lu, D. D. A. Clarke, J. Benda, A. Fleischer, H. Ni, K. Ueda, H. W. van der Hart, A. C. Brown, X. Gong, and J. Wu. Atomic partial wave meter by attosecond coincidence metrology. *Nat. Commun.*, 13(1):5072, 8 2022.

[23] M. Kretschmar, E. Svirplys, M. Volkov, T. Witting, T. Nagy, M. J. J. Vrakking, and B. Schütte. Compact realization of all-attosecond pump-probe spectroscopy. *Sci. Adv.*, 10(8):eadk9605, 2 2024.

[24] L-M. Koll, A. J. Suñer-Rubio, T. Witting, R. Y. Bello, A. Palacios, F. Martín, and M. J. J. Vrakking. Entanglement and electronic coherence in attosecond molecular photoionization. *Nature*, 652(8108):82–88, 4 2026.

[25] Z-H. Loh, M. Khalil, R. E. Correa, R. Santra, C. Buth, and S. R. Leone. Quantum state-resolved probing of strong-field-ionized xenon atoms using femtosecond high-order harmonic transient absorption spectroscopy. *Phys. Rev. Lett.*, 98(14):143601, 4 2007.

[26] Z-H. Loh and S. R. Leone. Ultrafast strong-field dissociative ionization dynamics of CH2Br2 probed by femtosecond soft x-ray transient absorption spectroscopy. *J. Chem. Phys.*, 128(20):204302, 5 2008.

[27] E. Goulielmakis, Z-H. Loh, A. Wirth, R. Santra, N. Rohringer, V. S. Yakovlev, S. Zherebtsov, T. Pfeifer, A. M. Azzeer, M. F. Kling, S. R. Leone, and F. Krausz. Real-time observation of valence electron motion. *Nature*, 466(7307):739–743, 8 2010.

[28] E. Papalazarou, D. Boschetto, J. Gautier, T. Garl, C. Valentin, G. Rey, P. Zeitoun, A. Rousse, P. Balcou, and M. Marsi. Probing coherently excited optical phonons by extreme ultraviolet radiation with femtosecond time resolution. *Appl. Phys. Lett.*, 93(4):041114, 7 2008.

[29] C. J. Kaplan, P. M. Kraus, A. D. Ross, M. Zürch, S. K. Cushing, M. F. Jager, H-T. Chang, E. M. Gullikson, D. M. Neumark, and S. R. Leone. Femtosecond tracking of carrier relaxation in germanium with extreme ultraviolet transient reflectivity. *Phys. Rev. B*, 97(20):205202, 5 2018.

[30] I. J. P. Molesky, S. K. Cushing, L. M. Carneiro, A. Lee, J. C. Ondry, J. C. Dahl, H-T. Chang, A. P. Alivisatos, and S. R. Leone. Photoexcited small polaron formation in goethite (α-feooh) nanorods probed by transient extreme ultraviolet spectroscopy. *J. Phys. Chem. Lett.*, 9(14):4120–4124, 7 2018.

[31] E. Sistrunk, J. Grilj, J. Jeong, M Samant, A. Gray, H. Dürr, S. Parkin, and M. Gühr. Broadband extreme ultraviolet probing of transient gratings in vanadium dioxide. *Opt. Express*, 23(4):4340–4347, 2 2015.

[32] J. D. Gaynor, A. P. Fidler, Y-C. Lin, H-T. Chang, M. Zuerch, D. M. Neumark, and S. R. Leone. Solid state core-exciton dynamics in NaCl observed by tabletop attosecond four-wave mixing spectroscopy. *Phys. Rev. B*, 103(24):245140, 6 2021.

[33] M. Hentschel, R. Kienberger, C. Spielmann, G. A. Reider, N. Milosevic, T. Brabec, P. Corkum, U. Heinzmann, M. Drescher, and F. Krausz. Attosecond metrology. *Nature*, 414(6863):509–513, 11 2001.

[34] G. Sansone, E. Benedetti, F. Calegari, C. Vozzi, L. Avaldi, R. Flammini, L. Poletto, P. Villoresi, C. Altucci, R. Velotta, S. Stagira, S. De Silvestri, and M. Nisoli. Isolated single-cycle attosecond pulses. *Science*, 314(5798):443–446, 10 2006.

[35] E. Goulielmakis, M. Schultze, M. Hofstetter, V. S. Yakovlev, J. Gagnon, M. Uiberacker, A. L. Aquila, E. M. Gullikson, D. T. Attwood, R. Kienberger, F. Krausz, and U. Kleineberg. Single-cycle nonlinear optics. *Science*, 320(5883):1614–1617, 6 2008.

[36] P. M. Paul, E. S. Toma, P. Breger, G. Mullot, F. Augé, P. Balcou, H. G. Muller, and P. Agostini. Observation of a train of attosecond pulses from high harmonic generation. *Science*, 292(5522):1689–1692, 6 2001.

[37] Y. Mairesse, A. de Bohan, L. J. Frasinski, H. Merdji, L. C. Dinu, P. Monchicourt, P. Breger, M. Kovačev, R. Taïeb, B. Carré, H. G. Muller, P. Agostini, and P. Salières. Attosecond synchronization of high-harmonic soft x-rays. *Science*, 302(5650):1540–1543, 11 2003.

[38] J. Peschel, D. Busto, M. Plach, M. Bertolino, M. Hoflund, S. Maclot, J. Vinbladh, H. Wikmark, F. Zapata, E. Lindroth, M. Gisselbrecht, J. M. Dahlström, A. L'Huillier, and P. Eng-Johnsson. Attosecond dynamics of multi-channel single photon ionization. *Nat. Commun.*, 13(1):5205, 9 2022.

[39] C. I. Froehly, A. Lacourt, and J. C. Viénot. Time impulse response and time frequency response of optical pupils:experimental confirmations and applications. *Nouv. Rev. Opt.*, 183(4):183–196, 7 1973.

[40] J. Piasecki, B. Colombeau, M. Vampouille, C. Froehly, and J. A. Arnaud. Nouvelle méthode de mesure de la réponse impulsionnelle des fibres optiques. *Appl. Opt.*, 19(22):3749–3755, 11 1980.

[41] T. Wittmann, B. Horvath, W. Helml, M. G. Schätzel, X. Gu, A. L. Cavalieri, G. G. Paulus, and R. Kienberger. Single-shot carrier–envelope phase measurement of few-cycle laser pulses. *Nat. Phys.*, 5(5):357–362, 5 2009.

[42] D. Habibović, K. R. Hamilton, O. Neufeld, and L. Rego. Emerging tailored light sources for studying chirality and symmetry. *Nat Rev Phys*, 6(11):663–675, 11 2024.

[43] Y. H. Wang, H. Steinberg, P. Jarillo-Herrero, and N. Gedik. Observation of floquet-bloch states on the surface of a topological insulator. *Science*, 342(6157):453–457, 10 2013.

[44] M. A. Sentef, M. Claassen, A. F. Kemper, B. Moritz, T. Oka, J. K. Freericks, and T. P. Devereaux. Theory of floquet band formation and local pseudospin textures in pump-probe photoemission of graphene. *Nat. Commun.*, 6(1):7047, 5 2015.

[45] F. Mahmood, C-K. Chan, Z. Alpichshev, D. Gardner, Y. Lee, P. A. Lee, and N. Gedik. Selective scattering between floquet–bloch and volkov states in a topological insulator. *Nat. Phys.*, 12(4):306–310, 4 2016.

[46] S. Sederberg, F. Kong, and P. B. Corkum. Tesla-scale terahertz magnetic impulses. *Phys. Rev. X*, 10(1):011063, 3 2020.

[47] A. de las Heras, F. P. Bonafé, C. Hernández-García, A. Rubio, and O. Neufeld. Tunable tesla-scale magnetic attosecond pulses through ring-current gating. *J. Phys. Chem. Lett.*, 14(49):11160–11167, 12 2023.

[48] P. B. Corkum, N. H. Burnett, and M. Y. Ivanov. Subfemtosecond pulses. *Opt. Lett.*, 19(22):1870–1872, 11 1994.

[49] M. Ivanov, P. B. Corkum, T. Zuo, and A. Bandrauk. Routes to control of intense-field atomic polarizability. *Phys. Rev. Lett.*, 74(15):2933–2936, 4 1995.

[50] V. T. Platonenko and V. V. Strelkov. Single attosecond soft-x-ray pulse generated with a limited laser beam. *J. Opt. Soc. Am. B*, 16(3):435–440, 3 1999.

[51] O. Tcherbakoff, E. Mével, D. Descamps, J. Plumridge, and E. Constant. Time-gated high-order harmonic generation. *Phys. Rev. A*, 68(4):043804, 10 2003.

[52] Z. Chang. Controlling attosecond pulse generation with a double optical gating. *Phys. Rev. A*, 76(5):051403, 11 2007.

[53] P. Tzallas, E. Skantzakis, C. Kalpouzos, E. P. Benis, G. D. Tsakiris, and D. Charalambidis. Generation of intense continuum extreme-ultraviolet radiation by many-cycle laser fields. *Nat. Phys.*, 3(12):846–850, 12 2007.

[54] S. A. Akhmanov, A. I. Kovrigin, A. S. Piskarskas, V. V. Fadeev, and R. V Khokhlov. Observation of parametric amplification in the optical range. *JETP Lett.*, 2(191):212–215, 7 1965.

[55] D. Strickland and G. Mourou. Compression of amplified chirped optical pulses. *Opt. Commun.*, 56(3):219–221, 12 1985.

[56] Y-C. Cheng, S. Mikaelsson, S. Nandi, L. Rämisch, C. Guo, S. Carlström, A. Harth, J. Vogelsang, M. Miranda, C. L. Arnold, A. L'Huillier, and M. Gisselbrecht. Controlling photoionization using attosecond time-slit interferences. *Proc. Natl. Acad. Sci. U.S.A.*, 117(20):10727–10732, 4 2020.

[57] F. Lindner, M. G. Schätzel, H. Walther, A. Baltuška, E. Goulielmakis, F. Krausz, D. B. Milošević, D. Bauer, W. Becker, and G. G. Paulus. Attosecond double-slit experiment. *Phys. Rev. Lett.*, 95(4):040401, 7 2005.

[58] B. Piglosiewicz, S. Schmidt, D. J. Park, J. Vogelsang, P. Groß, C. Manzoni, P. Farinello, G. Cerullo, and C. Lienau. Carrier-envelope phase effects on the strong-field photoemission of electrons from metallic nanostructures. *Nat. Photon.*, 8(1):37–42, 1 2014.

[59] K. C. Kulander, K. J. Schafer, and J. L. Krause. *Super-Intense Laser—Atom Physics*, volume 316 of *NATO Science Series B*. Springer New York, NY, 1993.

[60] M. Lewenstein, P. Balcou, M. Y. Ivanov, A. L'Huillier, and P. B. Corkum. Theory of high-harmonic generation by low-frequency laser fields. *Phys. Rev. A*, 49(3):2117–2132, 3 1994.

[61] P. B. Corkum. Plasma perspective on strong field multiphoton ionization. *Phys. Rev. Lett.*, 71(13):1994–1997, 9 1993.

[62] J. L. Krause, K. J. Schafer, and K. C. Kulander. High-order harmonic generation from atoms and ions in the high intensity regime. *Phys. Rev. Lett.*, 68(24):3535–3538, 6 1992.

[63] E. Constant, D. Garzella, P. Breger, E. Mével, C. Dorrer, C. Le Blanc, F. Salin, and P. Agostini. Optimizing high harmonic generation in absorbing gases: Model and experiment. *Phys. Rev. Lett.*, 82(8):1668–1671, 2 1999.

[64] R. Weissenbilder, S. Carlström, L. Rego, C. Guo, C. M. Heyl, P. Smorenburg, E. Constant, C. L. Arnold, and A. L'Huillier. How to optimize high-order harmonic generation in gases. *Nat. Rev. Phys.*, 4(11):713–722, 11 2022.

[65] K. Varjú, Y. Mairesse, B. Carré, M. B. Gaarde, P. Johnsson, S. Kazamias, R. López-Martens, J. Mauritsson, K. J. Schafer, P. Balcou, A. L'huillier, and P. Salières. Frequency chirp of harmonic and attosecond pulses. *J. Mod. Opt.*, 52(2-3):379–394, 9 2005.

[66] C. Guo, A. Harth, S. Carlström, Y-C. Cheng, S. Mikaelsson, E. Mårsell, C. Heyl, M. Miranda, M. Gisselbrecht, M. B. Gaarde, K. J. Schafer, A. Mikkelsen, J. Mauritsson, C. L. Arnold, and A. L'Huillier. Phase control of attosecond pulses in a train. *J. Phys. B: Atom. Mol. Opt. Phys.*, 51:034006, 1 2018.

[67] E. Appi, R. Weissenbilder, B. Nagyillés, Z. Diveki, J. Peschel, B. Farkas, M. Plach, F. Vismarra, V. Poulain, N. Weber, C. L. Arnold, K. Varjú, S. Kahaly, P. Eng-Johnsson, and A. L'Huillier. Two phase-matching regimes in high-order harmonic generation. *Opt. Express*, 31(20):31687–31697, 9 2023.

[68] A. M. Perelomov, V. S. Popov, and M. V. Terentév. Ionization of atoms in an alternating electric field. *Sov. Phys. JETP*, 23(5):1393–1409, 11 1966.

[69] G. L. Yudin and M. Y. Ivanov. Nonadiabatic tunnel ionization: Looking inside a laser cycle. *Phys. Rev. A*, 64(1):013409, 6 2001.

[70] J. A. R. Samson and W. C. Stolte. Precision measurements of the total photoionization cross-sections of he, ne, ar, kr, and xe. *J. Electron Spectrosc. Relat. Phenom.*, 123(2):265–276, 5 2002.

[71] C. Hernández-García, J. A. Pérez-Hernández, J. Ramos, E. Conejero Jarque, L. Roso, and L. Plaja. High-order harmonic propagation in gases within the discrete dipole approximation. *Phys. Rev. A*, 82(3):033432, 9 2010.

[72] S. Mikaelsson, J. Vogelsang, C. Guo, I. Sytcevich, A. L. Viotti, F. Langer, Y-C. Cheng, S. Nandi, W. Jin, A. Olofsson, R. Weissenbilder, J. Mauritsson, A. L'Huillier, M. Gisselbrecht, and C. L. Arnold. A high-repetition rate attosecond light source for time-resolved coincidence spectroscopy. *J. Nanophotonics*, 10(1):117–128, 9 2021.

[73] P. Salières, A. L'Huillier, and M. Lewenstein. Coherence control of high-order harmonics. *Phys. Rev. Lett.*, 74(19):3776–3779, 5 1995.

[74] P. Antoine, B. Carré, A. L'Huillier, and M. Lewenstein. Polarization of high-order harmonics. *Phys. Rev. A*, 55(2):1314–1324, 2 1997.

[75] V. Strelkov, A. Zaïr, O. Tcherbakoff, R. López-Martens, E. Cormier, E. Mével, and E. Constant. Single attosecond pulse production with an ellipticity-modulated driving IR pulse. *J. Phys. B: At. Mol. Opt. Phys.*, 38(L161):277–283, 5 2005.

[76] B. Shan, S. Ghimire, and Z. Chang. Generation of the attosecond extreme ultraviolet supercontinuum by a polarization gating. *J. Mod. Opt.*, 52(2-3):277–283, 9 2005.

[77] I. J. Sola, E. Mével, L. Elouga, E. Constant, V. Strelkov, L. Poletto, P. Villoresi, E. Benedetti, J-P. Caumes, S. Stagira, C. Vozzi, G. Sansone, and M. Nisoli. Controlling attosecond electron dynamics by phase-stabilized polarization gating. *Nat. Phys.*, 2(5):319–322, 5 2006.

[78] I. P. Christov, M. M. Murnane, and H. C. Kapteyn. High-harmonic generation of attosecond pulses in the "single-cycle" regime. *Phys. Rev. Lett.*, 78(7):1251–1254, 2 1997.

[79] R. Kienberger, E. Goulielmakis, M. Uiberacker, A. Baltuska, V. Yakovlev, F. Bammer, A. Scrinzi, H. Westerwalbesloh, U. Kleineberg, U. Heinzmann, M. Drescher, and F. Krausz. Atomic transient recorder. *Nature*, 427(6977):817–821, 2 2004.

[80] A. L. Cavalieri, E. Goulielmakis, B. Horvath, W. Helml, M. Schultze, M. Fieß, V. Pervak, L. Veisz, V. S. Yakovlev, M. Uiberacker, A. Apolonski, F. Krausz, and R. Kienberger. Intense 1.5-cycle near-infrared laser waveforms and their use for the generation of ultra-broadband soft-x-ray harmonic continua. *New J. Phys.*, 9(7):242, 7 2007.

[81] V. Schmidt. Photoionization of atoms using synchrotron radiation. *Rep. Prog. Phys.*, 55(9):1483, 9 1992.

[82] M. Li, H. Wang, R. Tahouri, R. Weissenbilder, J. Li, W. Wang, J. Cai, X. Hong, X. Shi, L-W. Pi, D. Busto, M. Gisselbrecht, K. Ueda, P. V. Demekhin, A. L'Huillier, J. M. Dahlström, E. Lindroth, D. Ding, and S. Luo. Photoionization time delays probe electron correlations. *Phys. Rev. Lett.*, 135(18):183202, 10 2025.

[83] Á. Jiménez-Galán, F. Martín, and L. Argenti. Two-photon finite-pulse model for resonant transitions in attosecond experiments. *Phys. Rev. A*, 93(2):023429, 2 2016.

[84] M. Isinger, D. Busto, S. Mikaelsson, S. Zhong, C. Guo, P. Salières, C. L. Arnold, A. L'Huillier, and M. Gisselbrecht. Accuracy and precision of the rabbit technique. *Phil. Trans. R. Soc. A*, 377(2145):2017–0475, 4 2019.

[85] J. M. Dahlström, D. Guénot, K. Klünder, M. Gisselbrecht, J. Mauritsson, A. L'Huillier, A. Maquet, and R. Taïeb. Theory of attosecond delays in laser-assisted photoionization. *Chem. Phys.*, 414:53–64, 3 2013.

[86] E. Arnous, S. Klarsfeld, and S. Wane. Angular distribution in the two-quantum atomic photoeffect. *Phys. Rev. A*, 7(5):1559–1568, 5 1973.

[87] A. L'Huillier, M. Lewenstein, P. Salières, P. Balcou, M. Y. Ivanov, J. Larsson, and C. G. Wahlström. High-order harmonic-generation cutoff. *Phys. Rev. A*, 48(5):R3433–R3436, 11 1993.

[88] A. T. J. B. Eppink and D. H. Parker. Velocity map imaging of ions and electrons using electrostatic lenses: Application in photoelectron and photofragment ion imaging of molecular oxygen. *Rev. Sci. Instrum.*, 68(9):3477–3484, 9 1997.

[89] J. Ullrich, R. Moshammer, A. Dorn, R. Dörner, L. P. H Schmidt, and H. Schmidt-Böcking. Recoil-ion and electron momentum spectroscopy: reaction-microscopes. *Rep. Prog. Phys.*, 66(9):1463, 8 2003.

[90] Y. Mairesse and F. Quéré. Frequency-resolved optical gating for complete reconstruction of attosecond bursts. *Phys. Rev. A*, 71(1):011401, 1 2005.

[91] M. Lucchini, M. H. Brügmann, A. Ludwig, L. Gallmann, U. Keller, and T. Feurer. Ptychographic reconstruction of attosecond pulses. *Opt. Express*, 23(23):29502–29513, 11 2015.

[92] M. Lucchini and M. Nisoli. Refined ptychographic reconstruction of attosecond pulses. *Appl. Sci.*, 8(12):2563, 12 2018.

[93] G. L. Dolso, G. Inzani, N. Di Palo, B. Moio, F. Medeghini, R. Borrego-Varillas, M. Nisoli, and M. Lucchini. Versatile and robust reconstruction of extreme-ultraviolet pulses down to the attosecond regime. *APL Photonics*, 8(7):076101, 7 2023.

[94] P. D. Keathley, S. Bhardwaj, J. Moses, G. Laurent, and F. X. Kärtner. Ptychographic reconstruction of attosecond pulses. *New J. Phys.*, 18(18):073009, 7 2016.

[95] I. Orfanos, I. Makos, I. Liontos, E. Skantzakis, B. Förg, D. Charalambidis, and P. Tzallas. Attosecond pulse metrology. *APL Photonics*, 4(8):080901, 8 2019.

[96] N. Rohringer, A. Gordon, and R. Santra. Configuration-interaction-based time-dependent orbital approach for ab initio treatment of electronic dynamics in a strong optical laser field. *Phys. Rev. A*, 74(4):043420, 10 2006.

[97] S. Carlström, J. Mauritsson, K. J Schafer, A. L'Huillier, and M. Gisselbrecht. Quantum coherence in photo-ionisation with tailored xuv pulses. *J. Phys. B: Atom. Mol. Opt. Phys.*, 51(1):015201, 11 2017.

[98] S. Carlström, M. Spanner, and S. Patchkovskii. General time-dependent configuration-interaction singles. I. molecular case. *Phys. Rev. A*, 106(4):043104, 10 2022.

[99] S. Carlström, M. Bertolino, J. M. Dahlström, and S. Patchkovskii. General time-dependent configuration-interaction singles. II. atomic case. *Phys. Rev. A*, 106(4):042806, 10 2022.

[100] J. Mauritsson, T. Remetter, M. Swoboda, K. Klünder, A. L'Huillier, K. J. Schafer, O. Ghafur, F. Kelkensberg, W. Siu, P. Johnsson, M. J. J. Vrakking, I. Znakovskaya, T. Uphues, S. Zherebtsov, M. F. Kling, F. Lépine, E. Benedetti, F. Ferrari, G. Sansone, and M. Nisoli. Attosecond electron spectroscopy using a novel interferometric pump-probe technique. *Phys. Rev. Lett.*, 105(5):053001, 7 2010.

[101] M. Lucchini, A. Ludwig, T. Zimmermann, L. Kasmi, J. Herrmann, A. Scrinzi, A. S. Landsman, L. Gallmann, and U. Keller. Anisotropic emission in quantum-beat spectroscopy of helium excited states. *Phys. Rev. A*, 91(6):063406, 6 2015.

[102] J. Fuchs, N. Douguet, S. Donsa, F. Martin, J. Burgdörfer, L. Argenti, L. Cattaneo, and U. Keller. Time delays from one-photon transitions in the continuum. *Optica*, 7(2):154–161, 2 2020.

[103] J. Joseph, F. Holzmeier, D. Bresteau, C. Spezzani, T. Ruchon, J. F Hergott, O. Tcherbakoff, P. D'Oliveira, J. C Houver, and D. Dowek. Angle-resolved studies of XUV–IR two-photon ionization in the RABBITT scheme. *J. Phys. B: Atom. Mol. Opt. Phys.*, 53(18):184–007, 7 2020.

[104] U. Fano. Propensity rules: An analytical approach. *Phys. Rev. A*, 32(1):617–618, 7 1985.

[105] D. Busto, J. Vinbladh, S. Zhong, M. Isinger, S. Nandi, S. Maclot, P. Johnsson, M. Gisselbrecht, A. L'Huillier, E. Lindroth, and J. M. Dahlström. Fano's propensity rule in angle-resolved attosecond pump-probe photoionization. *Phys. Rev. Lett.*, 123(13):133201, 9 2019.

[106] J. Benda, Z. Mašín, S. Palakkal, F. Lépine, S. Nandi, and V. Loriot. Angular momentum dependence in multiphoton ionization and attosecond time delays. *Phys. Rev. A*, 111(1):013110, 1 2025.

[107] J. Vinbladh, J. M. Dahlström, and E. Lindroth. Many-body calculations of two-photon, two-color matrix elements for attosecond delays. *Phys. Rev. A*, 100(4):043424, 10 2019.

[108] G. E. Moore. Cramming more components onto integrated circuits, reprinted from electronics, volume 38, number 8, april 19, 1965, pp.114 ff. *IEEE Solid-State Circuits Society Newsletter*, 11(3):33–35, 2006.

[109] C. Battaglia, A. Cuevas, and S. De Wolf. High-efficiency crystalline silicon solar cells: status and perspectives. *Energy Environ. Sci.*, 9(5):1552–1576, 2 2016.

[110] B. L. Henke, E. M. Gullikson, and J. C. Davis. X-ray interactions: Photoabsorption, scattering, transmission, and reflection at E = 50–30,000 ev, Z = 1-92. *At. Data Nucl. Data Tables*, 54(2):181–342, 7 1993.

[111] T. J. Whittles, L. A. Burton, J. M. Skelton, A. Walsh, T. D. Veal, and V. R. Dhanak. Band alignments, valence bands, and core levels in the tin sulfides SnS, SnS_2, and Sn_2S_3: Experiment and theory. *Chem. Mater.*, 28(11):3718–3726, 5 2016.

[112] R. Quintero-Bermudez, L. Drescher, V. Eggers, K. G. Xiong, and S. R. Leone. Attosecond transient grating spectroscopy with near-infrared grating pulses and an extreme ultraviolet diffracted probe. *ACS Photonics*, 12(4):2097–2105, 3 2025.

[113] M. P. Seah and W. A. Dench. Quantitative electron spectroscopy of surfaces: A standard data base for electron inelastic mean free paths in solids. *Surf. Interface Anal.*, 1(1):2–11, 2 1979.

[114] I. Vurgaftman, J. R. Meyer, and L. R. Ram-Mohan. Band parameters for III–V compound semiconductors and their alloys. *J. Appl. Phys.*, 89(11):5815–5875, 6 2001.

[115] P. Bauer Pereira, I. Sergueev, S. Gorsse, J. Dadda, E. Müller, and R. P. Hermann. Lattice dynamics and structure of GeTe, SnTe and PbTe. *Phys. Status Solidi B*, 250(7):1300–1307, 12 2013.

[116] B. L. Gelmont, T. R. Globus, and A. V. Matveenko. Optical absorption and band structure of PbTe. *Solid State Commun.*, 38(10):931–934, 6 1981.

[117] R. N. Tauber, A. A. Machonis, and I. B. Cadoff. Thermal and optical energy gaps in PbTe. *J. Appl. Phys.*, 37(13):4855–4860, 12 1966.

[118] R. Tsu, W. E. Howard, and L. Esaki. Optical and electrical properties and band structure of GeTe and SnTe. *Phys. Rev.*, 172(3):779–788, 8 1968.

[119] S. Palaz, H. Koc, A. M. Mamedov, and E. Ozbay. Topological insulators: Electronic band structure and spectroscopy. *IOP Conf. Ser.: Mater. Sci. Eng.*, 175(1):012–004, 2 2017.

[120] J. M. Skelton, S. C. Parker, A. Togo, I. Tanaka, and A. Walsh. Thermal physics of the lead chalcogenides PbS, PbSe, and PbTe from first principles. *Phys. Rev. B*, 89(20):205203, 5 2014.

[121] J. M. Skelton, L. A. Burton, F. Oba, and A. Walsh. Metastable cubic tin sulfide: A novel phonon-stable chiral semiconductor. *APL Mater.*, 5(3):036–101, 3 2017.

[122] E. Barrigón, M. Heurlin, Z. Bi, B. Monemar, and L. Samuelson. Synthesis and applications of iii–v nanowires. *Chem. Rev.*, 119(15):9170–9220, 8 2019.

[123] L. Hrachowina, N. Anttu, and M. T. Borgström. Wafer-scale synthesis and optical characterization of inp nanowire arrays for solar cells. *Nano Lett.*, 21(17):7347–7353, 8 2021.

[124] G. Badawy and E. P. A. M. Bakkers. Electronic transport and quantum phenomena in nanowires. *Chem. Rev.*, 124(5):2419–2440, 2 2024.

[125] P. Sinsermsuksakul, J. Heo, W. Noh, A. S. Hock, and R. G. Gordon. Atomic layer deposition of tin monosulfide thin films. *Adv. Energy Mater.*, 1(6):1116–1125, 9 2011.

[126] R. E. Banai, L. A. Burton, S. G. Choi, F. Hofherr, T. Sorgenfrei, A. Walsh, B. To, A. Cröll, and J. R. S. Brownson. Ellipsometric characterization and density-functional theory analysis of anisotropic optical properties of single-crystal α-SnS. *J. Appl. Phys.*, 116(1):013511, 7 2014.

[127] R. Jaramillo, M-J. Sher, B. K. Ofori-Okai, V. Steinmann, C. Yang, K. Hartman, K. A. Nelson, A. M. Lindenberg, R G. Gordon, and T. Buonassisi. Transient terahertz photoconductivity measurements of minority-carrier lifetime in tin sulfide thin films: Advanced metrology for an early stage photovoltaic material. *J. Appl. Phys.*, 119(3):035–101, 1 2016.

[128] R. E. Abutbul, A. R. Garcia-Angelmo, Z. Burshtein, M. T. S. Nair, P. K. Nair, and Y. Golan. Crystal structure of a large cubic tin monosulfide polymorph: an unraveled puzzle. *CrystEngComm*, 18(27):5188–5194, 5 2016.

[129] G. K. Wertheim and D. N. E. Buchanan. Crystal field splitting of core levels in β-Sn. *Solid State Commun.*, 69(6):689–692, 2 1989.

[130] M. Taniguchi, R. L. Johnson, J. Ghijsen, and M. Cardona. Core excitons and conduction-band structures in orthorhombic GeS, GeSe, SnS, and SnSe single crystals. *Phys. Rev. B*, 42(6):3634–3643, 8 1990.

[131] P. De Padova, M. Fanfoni, R. Larciprete, M. Mangiantini, S. Priori, and P. Perfetti. A synchrotron radiation photoemission study of the oxidation of tin. *Surf. Sci.*, 313(3):379–391, 7 1994.

[132] R. A. Abram, G. J. Rees, and B. L. H. Wilson. Heavily doped semiconductors and devices. *Adv. Phys.*, 27(6):799–892, 6 1978.

[133] I. Hamberg, C. G. Granqvist, K. F. Berggren, B. E. Sernelius, and L. Engström. Band-gap widening in heavily sn-doped In_2O_3. *Phys. Rev. B*, 30(6):3240–3249, 9 1984.

[134] B. G. Alberding, A. J. Biacchi, A. R. Hight Walker, and E. J. Heilweil. Charge carrier dynamics and mobility determined by time-resolved terahertz spectroscopy on films of nano-to-micrometer-sized colloidal Tin(II) monosulfide. *J. Phys. Chem. C*, 120(28):15395–15406, 6 2016.

[135] Y. Li, R. Clady, A. F. Marshall, J. Park, S. V. Thombare, G. Chan, T. W. Schmidt, M. L. Brongersma, and P. C. McIntyre. Ultrafast carrier dynamics of a photo-excited germanium nanowire–air metamaterial. *ACS Photonics*, 2(8):1091–1098, 7 2015.

[136] M. Guc, J. Andrade-Arvizu, I. Y. Ahmet, F. Oliva, M. Placidi, X. Alcobé, E. Saucedo, A. Pérez-Rodríguez, A. L. Johnson, and V. Izquierdo-Roca. Structural and vibrational properties of α- and π-SnS polymorphs for photovoltaic applications. *Acta Mater.*, 183:1–10, 1 2020.

[137] L. V. Keldysh. Ionization in the Field of a Strong Electromagnetic Wave. *Sov. Phys. JETP*, 20:1945–1957, 5 1965.

[138] P. Dombi, Z. Pápa, J. Vogelsang, S. V. Yalunin, M. Sivis, G. Herink, S. Schäfer, P. Groß, C. Ropers, and C. Lienau. Strong-field nano-optics. *Rev. Mod. Phys.*, 92(2):025003, 6 2020.

[139] R. Bormann, M. Gulde, A. Weismann, S. V. Yalunin, and C. Ropers. Tip-enhanced strong-field photoemission. *Phys. Rev. Lett.*, 105(14):147601, 9 2010.

[140] M. Schenk, M. Krüger, and P. Hommelhoff. Strong-field above-threshold photoemission from sharp metal tips. *Phys. Rev. Lett.*, 105(25):257601, 12 2010.

[141] B. Lovász, P. Sándor, Gellért-Zsolt Kiss, B. Bánhegyi, P. Rácz, Z. Pápa, J. Budai, C. Prietl, J. R. Krenn, and P. Dombi. Nonadiabatic nano-optical tunneling of photoelectrons in plasmonic near-fields. *Nano Lett.*, 22(6):2303–2308, 3 2022.

[142] B. Bánhegyi, G. Z. Kiss, Z. Pápa, P. Sándor, L. Tóth, L. Péter, P. Rácz, and P. Dombi. Nanoplasmonic photoelectron rescattering in the multiphoton-induced emission regime. *Phys. Rev. Lett.*, 133(3):033801, 7 2024.

[143] J. Heimerl, S. Meier, A. Herzig, F. López Hoffmann, L. Seiffert, D. M. B. Lesko, S. Hillmann, S. Wittigschlager, T. Weitz, T. Fennel, and P. Hommelhoff. Attosecond physics in optical near fields. *Nat. Phys.*, 21(12):1893–1898, 12 2025.

[144] K. Yee. Numerical solution of initial boundary value problems involving Maxwell's equations in isotropic media. *IEEE Trans. Antennas Propag.*, 14(3):302–307, 5 1966.

[145] T. E. Fischer. Photoelectric emission and work function of InP. *Phys. Rev.*, 142(2):519–523, 2 1966.

[146] M. Han, J-B. Ji, A. Blech, R. E. Goetz, C. Allison, L. Greenman, C. P. Koch, and H. J. Wörner. Attosecond control and measurement of chiral photoionization dynamics. *Nature*, 645(8079):95–100, 9 2025.

Acknowledgements

Before anything else, I want to thank the MHz laboratory, which taught me everything. I thought I already knew how to work hard, but then I became an experimentalist.

When I started my PhD, I wanted to operate particle detectors like Mathieu, bridge theory and experiment like Anne and love optics like Cord. Mathieu, I thank you for the support these last years. I am particularly grateful to my co-supervisors for their meaningful feedback on my written thesis. Anne, thank you for the financial support and the amount of time you spent helping me write manuscripts. Cord, I appreciate that you took the time to come to the theory meetings about my phase-matching model and the related article feedback. I would like to acknowledge your work in coordinating Kulturnatten, and I enjoyed volunteering very much each year.
I have to address specific thanks to Anders, who motivated me during hard times and supported me in analyzing data or writing manuscripts for the PEEM.

I am of course thankful to all the colleagues I shared these last years with. My journey started with my office mate from day one to roughly day end. Praveen, I always thought you were a profoundly kind person, and I wish you the best. Emilia, thanks for using my code and for the fun time in Innsbruck! Samuel, thanks for your unlimited energy and somehow keeping that prehistoric quantum beats project alive.

As time went by, the PEEM came by. Mahesh, thank you for forming countless images in the PEEM, and being the only one who knew how to do it decently! You are also the one who kept me company the most in the lab, especially during late nights! I absolutely want to thank Thomas. I will always remember our time in Berkeley, where I had such a good time being roommates, but I also thank you for still not knowing how to restart a single lab software (<3). Caroline, you brought me help by always taking the time to answer the questions I had about the rods, the wedges or other laser things! You are also a supportive person, which I felt lucky to have in the MHz. Chandni, thank you for teaching me sample transfer. Nelia, thank you for looking at some of the samples in the SEM. At last, Jan Vogelsang, thank you for being so welcoming regarding practical PEEM questions.

I also had the chance to receive help from many colleagues all over the world. I want to address each of them my deepest gratitude: Corentin Picot, Eric Constant, Rodrigo Martín-Hernández, Matteo Lucchini, Kevin Xion, Hugo Laurell, Jonah R. Aldeman, Stephen R. Leone, Stefanos Carlström, Claudio Verdozzi, Zhen Zhao, Emil Östberg.

The MHz is a big lab and I thank my fellow users. Ivan, thank you for watching me from your side of the lab when I started in the visible, completely alone and clueless. Daniel, we learned a lot from each other when you joined me to dive into the **wonderful** world of the OPCPA. Miguel, thank you for sharing my passion for coding. Anka, you had migrated to the D-lab before I arrived, but you did start in similar conditions I did (…). Anne-Lise, thank you for the organization skills. I did stop putting my hand on dead flies in the lab by the way… I will not forget about more recent arrivals: I thank Jin Niu for the many (many) cookies or candies and the plethora of students that came by throughout the years. Finally, I became a good experimentalist thanks to experienced people that reminded me it is ok to remove my goggles: Chen, without you no CEP would have ever been stabilized and Anders, hopefully you always had any weird equipment I needed.

The attogroup is a big group so I want to thank my fellow members.
Vénus, merci pour le soutien et ta capacité à vivre dans le moment présent, Aishwarya and Gergana for your kindness, Marius for all the workshop tricks and Elisa for always being cheerful! Melvin, tout simplement un garçon super (mes meilleurs vœux dans ta quête secondaire) et Gaspard, le meilleur représentant des doctorants ! Saga, thank you for being so good-natured and Yuman, thanks for always enjoying my office sofa. Robin, thank you for all the discussions about phase matching and for listening to my complaints during writing. Mattias, I enjoyed the trip to Stockholm with you! Edoardo, thank you for sharing my passion for intense moments in sports. Ah! And "Ici c'est Paris" ahahah. Gustav, it was always a pleasure to discuss with another original Wes Anderson admirer. Viktoriia, thank you for finally putting an end to the boy's band. David, thank you for the good times in Ascona and for giving me very welcomed ideas about my research! Finally, I am so grateful to have shared an office with Sizuo for some time, which was always there to answer data analysis questions and showing kindness I very much needed at the start of my PhD. I had other office mates that I thank: Zijie, that stopped shaving over the desk when asked to, and Linnas, who made me nostalgic for a second when he arrived all excited about everything.

At last, a huge help in research comes from the administrative staff. Åke, thank you for being so willing to help, always. The same goes for Anne-Peterson, Desiree, Emelie, Jane and Maria. Last but not least, I address countless thanks to the head of division Jörgen Larsson. You always listened to me carefully and we are very lucky to have you around. Finally, I address a very important thank you to Karen. You were a great help about literally everything, and I admire many things about you!

Yet, as time passes, colleagues and projects come and go. My heart, however, is always in Paris, where I was born in unconditional love. I also got another place where I am always welcomed in Sweden, thanks to Eva and Tommy.

Grand-père et grand-mère, vous êtes mon symbole de courage et de résilience dans l'adversité. Mazir, Anya, vous me protégez et me remettez en question avec la bienveillance et l'honnêteté dont seule une fratrie est capable. Nyou-nyou, je présente officiellement mes excuses pour avoir « malencontreusement » emporté ton pull en Suède (entre autres vêtements…). Mazou, merci pour tes recommandations littéraires (mais bon 300 pages lues et Hadrien raconte toujours sa vie...). Enfin,

je dédie ma thèse, en particulier mes heures d'enseignement, à ma mère. Et toute ma vie. Maman, « Voilà combien de jours, voilà combien de nuits, voilà combien de temps que je suis repartie ? ». Je vous aime juste trop.

John, jag svär att det inte finns någon bra fysik utan dig, även om du är min största källa till distraktion! Tack för att du alltid tar hand om mig, speciellt under de mycket svåra veckorna med experimentkampanjerna. Efter så mycket tålamod, låt oss leva ett fridfullt liv som en familj som älskar varandra, helt enkelt.

Mes dernières pensées sont pour mon père, à qui j'ai tant pensé pendant ma thèse.

"It's probably the last adventure I've got in me.
I was hopin' to go out in a flash of blazes,
but I'll probably just end up goin' home."

Steve Zissou, in *The life aquatic with Steve Zissou*.

Author contributions

Paper I: Impact of oblique reflections on the generation of isolated attosecond pulses by polarization gating

In this paper, a polarization gate is implemented in combination with an optical set-up that pre-compensates detrimental pulse propagation effects. The tailored few-cycle pulses are used to confine the XUV emission from HHG, thereby generating CEP-dependent continuous spectra compatible with the generation of SAPs.

I prepared and optimized the beamline before the campaign. I contributed to operate the beamline to acquire the data during the campaign. I participated in the discussion of the results and provided feedback on the manuscript.

Paper II: Subcycle phase matching effects in short attosecond pulse trains

In this paper, short APTs are generated using CEP-controlled few-cycle pulses. We characterize them with laser-assisted photoionization and find an unexpected energy-dependent number of attosecond pulses for some CEP values. Simulations indicate that macroscopic effects of the generation process, in particular temporal phase-matching, confines the harmonic emission of the high-orders, thereby impacting, non-trivially, the number of pulses in the train.

I took a leading role in analyzing the data and conceiving the one-dimensional model to explain them. I conceptualized and performed measurements to support the model. I took a leading role in discussing the results, analyzing the theoretical data (provided by Rodrigo Martín-Hernández), and writing the manuscript.

Paper III: Parity-mixing in photoionization

This paper investigates laser-assisted photoionization of helium atoms using a comb of broad harmonics in the presence of a few-cycle NIR laser field. Four different interference pathways are

found, which involve quantum paths of different parities. Their phase properties allow them to be disentangled and linked to different spectral regions of the main- and sidebands.

I was involved in acquiring the data during the campaign. I took a leading role in the data curation and analysis, as well as derived the theoretical framework and models for interpreting the data. I analyzed the TDSE theoretical data, calculated by Stefanos Carlström. I wrote the manuscript.

Paper IV: From interface-limited to Auger-dominated carrier dynamics in π-SnS

This paper presents a time-resolved study of carrier cooling and recombination dynamics in a metastable cubic phase of SnS, performed with attosecond transient absorption spectroscopy. The measurements are carried out under different photo-excitation conditions, leading to the identification of two carrier density-dependent regimes, in particular the onset of Auger mechanisms from a threshold density.

This was a very collaborative experiment, which resulted in a manuscript where I share first authorship with Hugo Laurell, Kevin Xiong and Thomas Kjellberg Jensen. I participated in data acquisition, jointly analyzed the data, and contributed to discussion of the results. I also contributed in writing the manuscript, in particular the "Results and Discussion" section.

Paper V: Ultrafast photoemission from InP nanowires mediated by local optical field enhancement

This paper establishes InP nanowires as a platform for producing localized, ultrashort electron bursts in the strong-field regime, owing to pronounced field enhancement capabilities. It reports field-enhancement-mediated strong-field emission from a semiconductor nanostructure, providing bandwidths supporting sub-femtosecond durations.

I conceived the experiment and obtained funding for it. I took the lead role in designing and building parts of the set-up, performing the measurements, analyzing the data and discussing the results. I wrote the manuscript.

Paper VI: Quantum beats: Finite pulse effects

This paper investigates interference effects involving highly excited states of helium using a comb of broad harmonics and few-cycle laser pulses. The influence of the spectral amplitude and phase of the laser field is emphasized. Monte Carlo simulations are developed to characterize the excited states, while accounting for the properties of the probe field.

I was involved in the acquisition of the data sets. I have contributed to the development of the data curation and analysis tools. I provided feedback on the manuscript.

Printed by Media-Tryck, Lund 2026 NORDIC SWAN ECOLABEL 3041 0903

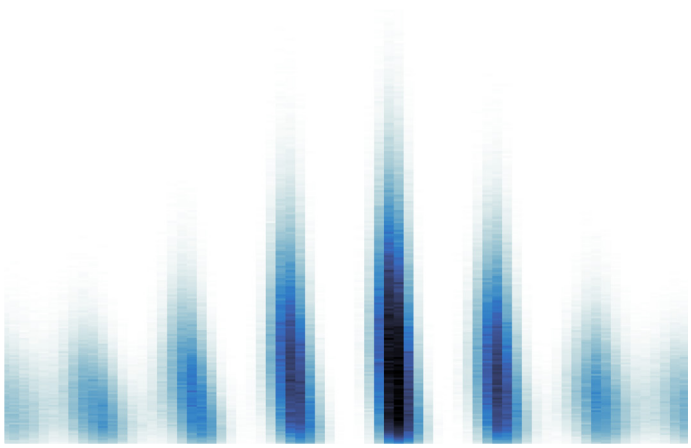

LUND UNIVERSITY

Faculty of Engineering, LTH
Department of Physics
Division of Atomic Physics
ISBN: 978-91-8104-984-8
ISSN: 0281-2762
Lund Reports on Atomic Physics, LRAP (2026)